

## ABSTRACT

STODDARD, NATHAN GREGORY. On the Interactions of Point Defects, Dopants and Light Element Impurities in Silicon as Stimulated by 200 kV Electron Irradiation. (Under the direction of George Rozgonyi and Gerd Duscher.)

The purpose of this research has been the investigation of atomic manipulation in silicon. It has been demonstrated that bulk vacancies and interstitials are created and spatially separated one Frenkel pair at a time during 200 kV electron irradiation of nitrogen-doped silicon. The mechanism by which the nitrogen pair allows Frenkel pair separation is shown to be a combination of the lowering of the energy barrier to a knock-on event combined with a more stable end-state. Anomalous nitrogen diffusion has been observed as a result of low energy ion milling, and the diffusion of nitrogen is studied theoretically, revealing a new, low energy model for N<sub>2</sub> pair diffusion. For the first time, 200 kV irradiation has been demonstrated not only to create Frenkel pairs during broad-beam irradiation, but also to allow the formation of extended defects like voids, oxygen precipitates and interstitial complexes. Using electron energy loss spectroscopy combined with first principles simulations, dark and bright areas induced in Z contrast images by 200 kV irradiation are demonstrated to be due to vacancy and self-interstitial complexes, respectively, with N>2. Finally, the manipulation of dopants in silicon is induced by using the difference in energy transferable from a 200 kV electron to light versus heavy elements (*e.g.* B vs. Sb). Atomic Force Microscopy is used to demonstrate that n-type regions with a size corresponding to the beam diameter are created in p-type material by short periods of 200 kV e-beam exposure. In this way, a method can be developed to create p-n-p type devices of arbitrary size in codoped silicon using a room temperature process.

**On the Interactions of Point Defects, Dopants and Light Element  
Impurities in Silicon as Stimulated by 200 kV Electron Irradiation**

by  
**NATHAN GREGORY STODDARD**

A dissertation submitted to the Graduate Faculty of  
North Carolina State University  
in partial fulfillment of the  
requirements for the Degree of  
Doctor of Philosophy

**MATERIALS SCIENCE AND ENGINEERING**

Raleigh

2004

**APPROVED BY:**

---

\_\_\_\_\_  
Co-chair of Advisory Committee      Co-chair of Advisory Committee



## Dedication

To my wife, Jennifer, whose love and partnership are my greatest assets.

## Biography

Nathan Gregory Stoddard was born in October, 1977 in the upper peninsula of Michigan. Schooled in Massachusetts, Ohio and finally at Exeter Township Senior High School in Reading, Pennsylvania, Nathan graduated at the top of his class in 1995 and proceeded to graduate summa cum laude from Villanova University in 1999 with a BS in Physics and a BA in Honors. After working for one year at Lockheed Martin, and in the meantime marrying his 'high school sweetheart', Jen, he worked for a year with Made4Me.com, an internet startup company (now Intellifit) writing software to produce custom fit clothing patterns. Nathan and Jen moved to North Carolina in the Fall of 2001 in order to start simultaneous graduate programs. Their first son, Benjamin, was born in November of 2002, and Jen graduated in May of 2003. Nathan is currently seeking a permanent position as a research scientist in industry.

## Acknowledgements

Many people have been helpful to the completion of this body of work, and several have been instrumental. First I would like to acknowledge my colleagues in research: Wolfgang Windl, Abdennaceur Karoui, Fred Stevie, Alex Kvit, Jag Kasichainula, Dawn Bonnell, Rui Shao, and Maxim Nikiforov. I would like to thank my parents, Greg and Teri, for their constant love and support, and I thank my wife, Jen for being my happiness and my lifelong companion. Thank you to my undergraduate research advisor, Joe Schick, for introducing me to the importance of basic scientific research. This work has been supported by the Silicon Wafer Engineering and Defect Science I/U CRC program (grant EEC-9726176) through the National Science Foundation and through the National Renewable Energy Laboratories under contract AAT-2-31605-05. Finally, I would like to acknowledge the members of my thesis committee for their consideration and helpful advice, and especially George Rozgonyi and Gerd Duscher who have been invaluable mentors to me in every way.

Soli Deo Gloria.

## Table of Contents

List of Tables.....	vii
List of Figures.....	viii
1 Grand Introduction.....	1
1.1 Current State of the Field.....	1
1.2 Literature Review.....	3
1.3 Electron-silicon interactions.....	7
2 Effects of 200 kV electron irradiation on nitrogen doped silicon.....	10
2.1 Materials and Methods.....	10
2.2 Results.....	11
2.3 Discussion.....	12
2.4 Conclusion.....	14
3 Nitrogen Pair Diffusion in Silicon.....	15
3.1 Introduction.....	15
3.2 Materials and Methods.....	15
3.3 Results.....	16
3.4 Discussion.....	18
3.5 Conclusion.....	18
4 Anomalous Nitrogen Diffusion during Ion Milling: a SIMS Study.....	20
4.1 Introduction.....	20
4.2 Materials and Methods.....	21
4.3 Results.....	23
4.4 Discussion.....	25

4.5	Conclusion.....	27
5	The Nucleation and Growth of Extended Defects in Silicon from their atomic constituents.....	29
5.1	Materials and Methods.....	29
5.2	Results.....	30
5.3	Discussion.....	35
5.4	Conclusion.....	42
6	Study of Point Defect Complexes by Electron Energy Loss Spectroscopy and First Principles Simulations.....	44
6.1	Introduction.....	44
6.2	Materials and Methods.....	44
6.3	Results and Discussion.....	46
6.4	Conclusion.....	55
7	The Athermal Manipulation of Dopants to Produce Device Structures on the Nanoscale.....	56
7.1	Introduction.....	56
7.2	Materials and Methods.....	57
7.3	Results.....	59
7.4	Discussion.....	60
7.5	Conclusion.....	61
8	Grand Conclusion.....	63
	References	

## List of Tables

1.	Bond lengths for diffusion sequences of nitrogen.....	75
2.	Summary of nitrogen concentrations after different TEM sample preparation processes.....	79
3.	Maximum energy transfer from a 200 kV electron to atoms of selected elements.....	92

## List of Figures

1.	Two configurations of nitrogen situated in silicon.....	67
2.	Energy transfer during an elastic e-Si collision as a function of angle.....	68
3.	Probability of scattering as a function of imparted energy.....	68
4.	Conventional TEM images of electron irradiated nitrogen-doped and nitrogen-free Czochralski silicon.....	69
5.	Close-up of Fig. 4 with evidence of faceted voids.....	70
6.	Z contrast STEM image of irradiated nitrogen-doped CZ-Si.....	70
7.	High resolution TEM image of an irradiation induced precipitate.....	71
8.	First diffusion path for the nitrogen pair in silicon.....	72
9.	Second diffusion path for the nitrogen pair in silicon.....	73
10.	Energetics for the diffusion paths of N <sub>2</sub> .....	74
11.	Theoretical and experimental data for the diffusion coefficient of N <sub>2</sub> in Si...	75
12.	Schematic of surface treatments used in TEM sample preparation.....	76
13.	Optical microscope image of a TEM sample prepared as in Fig. 12.....	76
14.	SIMS depth profiles of nitrogen in areas of different TEM sample preparation steps.....	77
15.	SIMS depth profiles of samples with different ion milling treatments.....	78
16.	SIMS depth profile of a sample with a surface nitride removed by ion milling	79
17.	N-CZ Si sample after extended broad-beam irradiation with electron energy loss spectra from different particles.....	80
18.	Electron irradiation of nitrogen-doped Float Zone silicon.....	81
19.	Convergent beam electron irradiation at different beam diameters.....	82

20.	Diffusion path for a silicon atom ejected near a nitrogen pair into a nearby interstitial position.....	83
21.	Energetics for the series illustrated in Fig. 20.....	84
22.	Model for electron-beam induced precipitation in N-CZ Si.....	84
23.	Cyclical model for the creation of point defects, voids and oxygen precipitates, aided by the nitrogen pair.....	85
24.	EELS spectra of interstitial-rich and vacancy-rich regions of irradiated N-FZ Si.....	86
25.	High energy resolution EELS spectra of N-FZ Si.....	87
26.	Point defects and point defect complexes in silicon.....	88
27.	Simulated EELS signals from silicon containing point defects.....	89
28.	Simulated EELS signals from silicon containing vacancy complexes.....	90
29.	Simulated EELS signals from silicon containing interstitial complexes.....	91
30.	Doping profiles of compensated silicon, co-implanted with boron and antimony.....	93
31.	Cross-sectional Z contrast images of the near surface of recrystallized implant damage.....	94
32.	Atomic force microscope images of topography and surface potential including one irradiated spot.....	95
33.	AFM images of topography and surface potential including a number of irradiated spots.....	96
34.	Device configuration for the measurement of electrical characteristics of nanodiodes.....	97

# 1 General Introduction

## 1.1 Current State of Research

Decades of work have created an understanding of the fundamental physics as well as the very successful implementation of engineering techniques to create both efficient solar cells and highly integrated electronic devices. In the field of crystal growth, the key to obtaining highest quality material is control of the point defects and light element impurities incorporated at the solid-melt interface. Once wafers are cut from the ingot, subsequent annealing regimens further tailor the concentration and distribution of larger extended defects that nucleate from smaller grown-in defects. Prime among the extended defects important in single crystal silicon are oxygen precipitates and related stacking faults. Although much is known of the details of the growth process, the nucleation process is still poorly understood. It is believed that nuclei grow one atom at a time, enabled by bulk diffusion at high temperatures.

Point defects play a central role in defect formation on large and small levels during crystal growth and they are central to solid-state diffusion. Vacancies and self-interstitials are especially active at high temperatures, and their behavior in many ways influences the final properties of devices.<sup>1</sup> Extensive experimental and theoretical work has been applied to determining the structural configurations of point defects as well as their formation and activation energies.<sup>2,3,4,5</sup> The thorough application of *ab initio* atomic simulations have produced a wealth of insights into the interactions of impurities and point defects and experimental techniques like Fourier Transform of Infrared (FTIR) can provide useful comparison points. Nevertheless, there is no way to image or in any way spatially resolve

individual point defects or complexes of several atoms, so matching experimental to theoretical data has remained elusive.

## 1.2 Literature Review: nitrogen in silicon and the irradiation of silicon

Among the light element impurities, the use of nitrogen doping in high purity silicon has been a topic of much research in the last few years.<sup>6</sup> Both Czochralski (CZ) grown and Float Zone (FZ) processed single crystal silicon benefit in their defect profiles from the introduction of low concentrations ( $< 10^{15} \text{ cm}^{-3}$ ) of nitrogen. Specifically, nitrogen doped CZ silicon (N-CZ Si) has increased denuded zone integrity<sup>7</sup> combined with a higher density of smaller oxygen precipitates in the bulk that provide improved gettering ability compared to nitrogen free CZ Si.<sup>8</sup> The oxygen precipitate nuclei exist in the as-grown N-CZ Si at a high density, while subsequent precipitate growth rate and size are limited by oxygen diffusion, requiring high temperatures<sup>8,9</sup>. Theoretical work<sup>10</sup> suggests that the split-interstitial  $\text{N}_2$  complex is quite stable and tends to form vacancy complexes either as  $\text{VN}_2$  or, more prevalently,  $\text{V}_2\text{N}_2$ . These complexes tie up vacancies at high temperature and reduce the formation of voids by delaying the onset temperature of void formation in the cooling process<sup>8</sup>. The importance of nitrogen doping in silicon stems from the significant role that nitrogen plays, both interacting with point defects during crystal growth and influencing oxygen precipitation during subsequent annealing.<sup>8</sup> The nitrogen pair has become well-known as a very stable defect configuration, with an energy reported to be lower than two interstitial nitrogen atoms by 4.3eV.<sup>11,12</sup> It has been observed to diffuse up to four orders of magnitude faster than substitutional nitrogen, with an experimentally measured diffusion coefficient of  $D_{\text{N}_2} = 2700e^{-2.8eV/kT}$ , although this value is based on only four annealing

temperatures.<sup>13,14</sup> It has also been shown that the N<sub>2</sub> pair readily complexes with vacancies, both in an unstable N<sub>2</sub>V configuration, and in the very stable N<sub>2</sub>V<sub>2</sub> configuration which can either form from the reaction N<sub>2</sub>V + V → N<sub>2</sub>V<sub>2</sub> or N<sub>2</sub> + V<sub>2</sub> → N<sub>2</sub>V<sub>2</sub>. The N<sub>2</sub>V<sub>2</sub> complex has further been shown to attract oxygen into a stable configuration, indicating the possibility of further oxygen precipitate nucleation based on the N<sub>2</sub> pair.<sup>15,16</sup> Schultz and Nelson have discovered a diffusion path for singly occurring interstitial nitrogen involving a pure interstitialcy mechanism.<sup>17</sup> A low migration energy diffusion path is demonstrated, going from a threefold-coordinated split interstitial site to a twofold coordinated bridge site and back again, but Schultz and Nelson ignore the N<sub>2</sub> pair configuration, which many believe to be the most prevalent nitrogen defect. The diffusion of the nitrogen pair has been considered by Sawada *et al.*, both with simultaneous movement and with sequential movement of the nitrogen atoms, with reported values for the activation barrier of 3.3 and 2.9 eV, respectively.<sup>18</sup> The lower energy barrier agrees well with the experimental value, and moves the nitrogen from the antiparallel ground state to the Humble configuration, both shown in Figure 1, with a second barrier of 1.0 eV to move back into a different antiparallel configuration in a break and make bonding type of motion. Sawada *et al.* make a point of either using known structures or configurations with obvious symmetry. In this work, the requirements of symmetry in the diffusion path are dropped and a new, lower energy diffusion path for the nitrogen pair is found that may require a revision of the experimental data. Furthermore, a report will be given of anomalous diffusion of nitrogen during low energy ion milling, where secondary ion mass spectroscopy has demonstrated near room temperature diffusion of nitrogen.

Since the advent of million-volt electron microscopes, electron interactions with silicon have been studied using high voltage electron microscopy (HVEM).<sup>19</sup> The main interaction is termed non-ionizing energy loss (NIEL) in the world of radiation studies, a synonym for damage caused by elastic collisions, but applying not only to electron bombardment, but also to irradiation by all types of particles. The interest in radiation processes was fueled initially by the development of nuclear reactors and by the placement of spacecraft and satellites in space where cosmic radiation is ever-present. High end silicon solar cells, used to power devices in space, drove both the improvement of solar cell efficiencies and the understanding of radiation-induced defects.<sup>20,21</sup> The study of defect evolution in silicon is now its own field of study, and broad-beam high voltage electron irradiation is one of the key tools. Based on the modified Kinchin-Pease expression (see equation II, below), each electron in a 1 MeV beam can create a damage cascade of up to four Frenkel pairs, although many more atoms are temporarily affected. The vacancies and silicon interstitials then react with each other and evolve into larger defect complexes, among which voids, dislocation loops and [311] rod defects are by far the most studied.<sup>22, 23, 24</sup> The formation of the defects cannot be discounted, but for the study of high temperature thermal defect evolution, the environment of radiation-induced damage cascades is decidedly non-equilibrium. While most HVEM irradiation employs broad-beam irradiation and has the resulting confusion of constant recombination and generation, a more recent study has employed a 1 MeV STEM to do convergent beam irradiation.<sup>25</sup> Arai *et al.* induce separation of the Frenkel pair components by controlling the temperature of irradiation at just above room temperature to favor the diffusion of one defect over the other. They thereby simplify the point defect complexing picture by limiting the extent of point defect recombination. The

founding result of the work presented here demonstrates the creation and separation of Frenkel pairs in nitrogen-doped silicon, but at only 200 kV electron accelerating voltage. Subsequent interaction and complexing of vacancies, self-interstitials and oxygen is also observed by a number of methods.

Much work has also been applied to the simulation of radiation damage and elastic processes. One of the basic parameters of radiation damage is the displacement energy for a material. This can be determined theoretically by finding the saddle point during kick-out of a lattice atom. For silicon, this value depends on the direction in which the atom is knocked, but has been calculated to range from 10-20 eV.<sup>26</sup> To accomplish a larger scale modeling of irradiation processes, molecular dynamics simulations are necessary, and have been used to simulate extended defect nucleation and growth. The most recent research has employed multiscale modeling and continuum models to more closely match experimental data on material strength and the dynamics of defect growth.<sup>27,28,29</sup>

### 1.3 Electron-Silicon Interactions in a 200 kV TEM

The electrons of the most common TEM beam carry 200 keV of energy, giving them relativistic speeds with  $v/c = 0.695$ . Interactions with atoms in a crystalline solid can be either elastic or inelastic. Inelastic scattering gives rise to a diffuse background of electrons that have lost relatively little energy from interactions with valence electrons, core electrons, phonons, *etc.* Elastic (or energy-conserving) scattering of electrons from the screened nucleus gives rise to diffraction patterns, so-called HOLZ lines and, at higher scattering angles, a small background of Rutherford back-scattered electrons. It is the electrons scattered to large angles that are of greatest interest here, since they can impart up to the

entirety of their momentum to the target atom. Momentum conservation limits the amount of energy that can be transferred, and in the case of a silicon atom, the energy transferred,  $T$ , by an electron scattered to an angle  $\theta$  is

$$\text{I.)} \quad T = \frac{2E_e}{m_{Si}c^2} (E_e + 2m_e c^2) \sin^2 \frac{\theta}{2}$$

where  $E_e$  is the electron energy (*e.g.* 200 keV),  $c$  is the speed of light and  $m_e$  is the electron rest mass.<sup>30</sup> Using this expression, the maximum possible transferred energy, corresponding to  $\theta = 180$ , is  $T_{max} = 18.7$  eV in a 200 kV TEM. The full plot of transferred energy vs. scattering angle is given in Fig. 2 for electrons of 140, 160 and 200 keV. The number of Frenkel pairs,  $N_{FP}$ , created from a knock-on collision is described by the modified Kinchin-Pease expression

$$\text{II.)} \quad N_{FP} = \begin{cases} 0 & T < E_d \\ 1 & E_d \leq T \leq 2.5E_d \\ 0.4E_D / E_d & 2.5E_d < T \end{cases}$$

where  $T$  is the imparted energy and  $E_d$  is the displacement energy for the material. For silicon, experiments suggest that  $E_d$  ranges from 12-20eV while theoretical studies have indicated that it might be as low as 10 eV, and depends on the crystallographic orientation.<sup>30,26</sup> For the lowest theoretical values, there have been suggestions that Monte Carlo simulations for longer periods of time result in recombination of the Frenkel pair, so that the spontaneous recombination volume (SRV) is larger at 300K than *ab initio* calculations might predict. If the effective displacement energy is less than 18.6 eV for a given zone-axis alignment, then one would expect Frenkel pairs to be created during 200kV electron irradiation. Under normal operating conditions, with a beam diameter greater than

10 nm, damage accumulation is not observed. Even though it is commonly quoted that the minimum TEM beam energy to create Frenkel pairs in Si is 140-160 keV, which corresponds to a maximum energy transfer of 12.4-14.4eV to silicon, damage is typically only seen under conditions where the beam is converged to a diameter of ~5nm, at which point a hole can develop in the thin foil. Another notable exception to the absence of radiation damage is the use of sample cooling. In an experiment by Yamasaki *et al.* where the sample temperature was maintained at 15K, some permanent damage formation became evident after exposure to a dose of  $3 \times 10^{23}/\text{cm}^2$ .<sup>31</sup> This affirms the earlier conjecture about temperature effects on the SRV, and suggests that Frenkel pairs are created during the course of 200kV irradiation under all irradiation conditions; at normal temperatures (300-400K), the Frenkel pairs recombine soon after the collision, but at low temperatures the damage is frozen in. A second important conclusion in Yamasaki's study, agreeing with that of Seidman *et al.*,<sup>32</sup> is that amorphization of silicon is extremely difficult below 1 MeV of accelerating energy, even at low temperature. Yamasaki and Takeda conclude from this that the introduction of one-at-a-time Frenkel pairs is insufficient for amorphization, but that damage cascades are the nuclei for amorphization. This will be revisited based on the results presented below.

To determine the probability of a knock-on collision, one starts with the scattering cross section. The differential Mott cross section for elastic scattering provides a relativistic correction to the Rutherford expression as follows<sup>33</sup>

$$\text{III.)} \quad \left( \frac{d\sigma}{d\Omega} \right)_{\text{Rutherford}} = \left( \frac{Ze^2}{8\pi\epsilon_0 E} \right)^2 \left( \frac{E + E_0}{E + 2E_0} \right)^2 \frac{1}{\sin^4 \frac{\theta}{2}}$$

$$\left( \frac{d\sigma}{d\Omega} \right)_{\text{Mott}} = \left( \frac{d\sigma}{d\Omega} \right)_{\text{Rutherford}} \left\{ 1 - \beta^2 \sin^2 \frac{\theta}{2} + \pi\alpha\beta \sin \frac{\theta}{2} \left( 1 - \sin \frac{\theta}{2} \right) \right\}$$

where  $Z$  is atomic number,  $E$  is the electron energy,  $E_0$  is the electron rest energy,  $e$  is the electron charge,  $\epsilon_0$  is the vacuum permittivity,  $\theta$  is the scattering angle,  $\alpha = Z/137$  and  $\beta = v/c$ . The cross-section for imparting *at least* a given value of energy  $T(\theta)$  (i.e. scattering to greater than a given scattering angle  $\theta_{min}$ ) can be derived from the differential cross-section by integration.

$$\text{IV.)} \quad \sigma_{Mott}(T) = \int_{\theta_{min}}^{\pi} \left( \frac{d\sigma}{d\Omega} \right)_{Mott} 2\pi \sin(\theta) d\theta$$

To translate the cross section into a probability, one can first convert the cross section into an angle-dependent mean free path.<sup>34</sup>

$$\text{V.)} \quad \lambda_{elastic}(\theta) = \frac{1}{\sigma_{Mott} n_a}$$

where  $n_a$  is the number of atoms per unit volume. The probability is then defined by Poisson statistics in terms of the ratio of the sample thickness,  $t$ , to the mean free path.

$$\text{VI.)} \quad P_{elastic}(t, \theta) = \frac{t}{\lambda_{el}} e^{-t/\lambda_{el}}$$

The probability for a collision that transfers energy greater or equal to a given value is plotted in Fig. 3, so that the probability of a knock-on event can be determined.

This analysis will be used extensively below in an attempt to explain the origin of many of the 200 kV irradiation effects that are observed. A thorough understanding of the nature and frequency of electron-silicon interactions is key to the interpretation of the results to come. This thesis will begin with a number of novel observations dealing with the electron irradiation of nitrogen-doped silicon in Section 2. In Section 3, a theoretical study of the diffusion of the nitrogen pair in silicon will be presented where a new, lowest energy mechanism has been discovered that is in good agreement with experimental data. An

experimentally discovered anomaly in nitrogen diffusion is reported in Section 4, where it is demonstrated that nitrogen can diffuse over several micrometers in silicon and in the process build up higher concentrations during low energy, low angle ion milling. This concentration enhancement is important to an explanation of the electron irradiation effects observed in N-doped Si, which is provided along with additional experimental data in Section 5. This section of the thesis also deals with oxygen precipitation, as well as void formation in low-oxygen nitrogen-doped silicon. In Section 6, the clustering of vacancies and interstitials during electron irradiation is studied using electron energy loss spectroscopy (EELS) and supporting theoretical simulations. Section 7 extends the electron-assisted manipulation of silicon to electronic dopants with fruitful results. Specifically, a method is demonstrated for athermally creating p/n junctions of arbitrary size in co-doped silicon.

## 2 Effects of 200 kV electron irradiation on nitrogen doped silicon

Published as “*In Situ* Point Defect Generation and Agglomeration during Electron Beam Irradiation of Nitrogen-doped Czochralski Silicon”

N. Stoddard, A. Karoui, G. Duscher, A. Kvit and G. Rozgonyi, *Electrochemical and Solid State Letters* **6**(11) G134-136 (2003).

### 2.1 Materials and Methods

Three [100] oriented CZ wafers, one from Nippon Steel with  $[N] = 1 \times 10^{15} \text{ cm}^{-3}$  (measured by secondary ion mass spectroscopy) and two nitrogen-free reference samples, were prepared for plan view transmission electron microscope (TEM) imaging using standard methods. A Wacker Siltronic N-free reference sample had an unknown grown-in vacancy/interstitial prevalence while the other, from MEMC, was grown at the ‘perfect’ Voronkov  $v/G$  ratio such that neither intrinsic point defect was predominant<sup>35</sup>. In a Topcon 002B TEM, all samples were [100] aligned and irradiated under a converged 200 kV electron beam from a high electron flux  $\text{LaB}_6$  filament. The converged beam diameter was  $\sim 400 \text{ nm}$  and irradiation was performed on different areas of the same foil for between 5 and 45 minutes. Analysis by conventional TEM methods was performed *in situ* in the Topcon microscope and later in a JEOL 2010F field emission Scanning TEM (STEM) capable of high resolution (HRTEM), Electron Energy Loss Spectroscopy (EELS) and Z-Contrast imaging. The Z-Contrast imaging is particularly important in separating atomic number contrast from stress contrast, which is unavoidable in conventional modes of TEM<sup>36</sup>.

## 2.2 Results

Changes in the nitrogen-doped sample were evident after five minutes of irradiation, with more dramatic effects appearing after twenty minutes, see Fig. 4A, while the Wacker N-free reference sample is essentially unchanged under the same conditions, see Fig. 4B. Note that the grainy texture in the center of Fig. 4A is absent in Fig. 4B, while the stress contrast lines are much stronger in Fig. 4B. At higher magnification, more details of the grainy texture in the N-CZ irradiated volume are revealed, see Fig. 5. Dark triangular areas, indicated by arrows, suggest the formation of faceted voids. A STEM Z-Contrast image, free from interference due to stress contrast, provides key information about the average atomic density in Fig. 6. The micrograph shows a dark (i.e. low  $Z$ ) central region corresponding to the size of the converged beam, surrounded by a bright ring. Because of the transparency of Z-contrast image analysis, we may interpret the dark central region to be vacancy-rich, while the bright surrounding ring is interstitial rich. Some spots of brighter contrast can be seen within the dark region. They may be clusters of lattice atoms in the vacancy rich region, or possibly small areas of a second phase with a higher mass density than the rest of the vacancy rich region. Examining the clusters more closely, high-resolution images have provided some evidence of agglomerated point defects and secondary phases, see Fig. 7, whose presence is supported by the extra spots in the Fourier transforms. It is possible that the precipitate-like region may be due to grown-in nitrogen-oxygen precipitates. These grown-in precipitates should not have high enough volume density for their presence in the irradiated region to be likely, but the chance cannot be ruled out. Since we have seen several clustered aggregations inside the irradiated volume in Z-Contrast and high-resolution images,

and none outside, then either the beam interactions are nucleating the clusters or playing a crucial role in stimulating their growth.

The two N-free reference samples exhibited some subtle differences in response to the beam. Specifically, we have observed some stress introduced in the Wacker N-free material, as in Fig 4B, that is absent in the “perfect” MEMC N-free material. This difference in the response of the reference samples to the e-beam can be explained because, unlike the MEMC reference that has negligible  $V_{Si}$  and  $Si_i$  concentrations, the Wacker sample was grown under conditions such that a significant excess of either vacancies or interstitials is present. This prevailing point defect will diffuse rapidly due to the driving force of the electron irradiation, even when the lattice is not disturbed. The resulting point defect concentration gradients in the Wacker sample produce the stress contours that are absent in the MEMC sample.

### 2.3 Discussion

These results corroborate the occurrence of Frenkel pair formation during the interaction of 200 kV electrons with thin foils of silicon. In the N-free samples, the material shows no signs of the grainy texture present in the N-CZ, see Fig. 4. Since the collision dynamics are the same, Frenkel pairs must be created in all thin foil Si samples. Normally, recombination is highly likely, since there is little kinetic energy left over after the knock-on process. Therefore, without the intervention of nitrogen, there would be no long-range diffusion or vacancy agglomeration. In the presence of nitrogen, and due to its affinity with vacancies, the Frenkel pair constituents separate. Once separated, the interstitial atoms experience enhanced diffusion because of the constant electron bombardment, migrating

either to the surface, or to an area just outside of the 400nm beam diameter. This causes a ring of locally higher density, imaged by Z-Contrast as the bright ring seen in Fig. 4, while the interstitial and vacancy concentration gradients set up the considerable stress seen in Fig. 4A. As for the separation process, it is known that nitrogen forms complexes with vacancies in the forms of VN, VN<sub>2</sub> and V<sub>2</sub>N<sub>2</sub>.<sup>10</sup> These complexes are nuclei for oxygen precipitation<sup>37</sup>, and would be likely to capture vacancies if present immediately after a silicon knock-on process, thereby preventing recombination with the interstitial and allowing the self-interstitial to diffuse away. Subsequently, the N-V nuclei could either capture more vacancies and evolve towards a void, or gather oxygen atoms initiating a SiO<sub>2</sub> nucleation process. The TEM results presented above support this idea, providing evidence for the presence of both voids (Figs. 5, 6) and nuclei of a second phase (Fig. 7). If the nitrogen can later separate from the aggregation, then a single N atom (or N<sub>2</sub> pair) could initiate multiple agglomerates over time. Although enough oxygen is present to form significant aggregates, we do not yet have direct evidence for the presence of oxygen in the observed clusters.

Further experiments and simulation are necessary to elucidate the complex interactions of V<sub>Si</sub>, Si<sub>I</sub>, N and O, particularly since initial calculations indicate that, for a homogeneous distribution of nitrogen in the material, the dramatic difference in nitrogen-doped silicon is caused by fewer than ten atoms of nitrogen in the irradiated volume. This is conceptually problematic, and some alternatives must be considered. First, each nitrogen atom could be the seed of many extended defects over time. In fact, this is quite probable since nitrogen tends to segregate to the surface of growing precipitates and voids. However, even this argument is insufficient with fewer than ten atoms. Second, there may be a preparation-induced intensification of the nitrogen concentration in the thin TEM foil. We

believe that the N-doped and N-free wafers are otherwise identical in growth conditions and doping, and can only conclude that, as in the CZ growth and annealing processes, small concentrations of nitrogen can have significant effects on material properties.

## 2.4 Conclusion

The results of this experiment open the interesting possibility of creating a “laboratory” for performing kinetic studies of intrinsic point defects interacting with N and O atoms under the electron beam and at room temperature. Observing the formation of point defect agglomerates under the beam should enhance our understanding of the nucleation of octahedral voids and oxygen precipitates by sidestepping the experimental constraints of high temperature crystal growth and wafer processing.

### 3 Nitrogen Pair Diffusion in Silicon

Submitted to Physical Review Letters as “A New, Low Energy Model for Nitrogen Pair Diffusion in Silicon”, by N. Stoddard, G. Duscher, P. Pichler and W. Windl, July 2004

#### 3.1 Introduction

The current work on modeling nitrogen diffusion was reviewed above. Previous models for nitrogen diffusion have ignored the  $N_2$  paired configuration<sup>17</sup> or constrained the movement based on the requirement of maintaining symmetry<sup>12</sup>. In this work, the requirements of symmetry along the diffusion path are dropped, and two new diffusion paths are identified with calculations that make use of rigorous corrections to the subtleties of the local density approximation (LDA) and a careful determination of the saddle point. One of these two paths has a lower activation energy than any previously reported path.

#### 3.2 Materials and Methods

Simulations were performed using the Vienna *Ab Initio* Simulations Package (VASP), which employs a self-consistent approach based on density functional theory in the local density approximation. Ultra-soft pseudopotentials with a plane-wave basis set were used both for ionic relaxation and for calculating the total energy at different points along the diffusion path. A perfect supercell of 64 silicon and two nitrogen atoms, *i.e.* eight conventional unit cells, was first relaxed with the well-known  $N_2$  structure consisting of two nitrogen and two silicon atoms in a square configuration in the [110] direction. A similar configuration with the  $N_2$  pair situated in an equivalent near-by position was relaxed, and four to six intermediate positions between these two were interpolated as starting guesses for

nudged elastic band calculations, and each was locally relaxed to a total energy tolerance of 0.005 eV. Only the neutrally charged case is considered, since in other work the energy difference between negative and neutral charge states was negligible while the positive charge state had higher energies by a constant energy shift.<sup>18</sup> Throughout the calculations, the k-point mesh was generated using the Monkhorst-Pack scheme using a 2x2x2 matrix. Corrections were applied to the total energy and Fermi energy positions in an attempt to correct subtle errors arising from the assumptions inherent to the simulation, including the bandgap size correction or “scissors operator” (usually the most significant), corrections due to the finite size of the supercell,<sup>\*</sup> and an adjustment to energy levels within the bandgap, *e.g.* the Fermi energy.<sup>38</sup>

### 3.3 Results

The different stages along the first diffusion path are illustrated in Figure 8. The two nitrogen atoms part ways, one moving up while the other moves down, only to meet again on the other side of the cell’s central atoms. The atoms move disjointedly, with the upper atom moving through (2A-2C) before the lower atom does (2D-2F), while the highest energy configurations are those where the nitrogen atoms are the farthest separated. In this [001] projection, it appears that the configurations of Fig. 8D may be the pentagonal Humble configuration (see Fig. 1), but from a different view (Fig. 8D inset) this is clearly not the case. The nitrogen atoms maintain threefold coordination almost throughout the motion,

---

<sup>\*</sup> This correction makes the 2x2x2 k-point sampling equivalent to or better than uncorrected 4x4x4 meshes

with the bond length varying from 1.44 to 2.33 Å, but mostly within  $1.8 \pm 0.1 \text{Å}$ , see Table 1. The activation energy for this diffusion series is only 2.37 eV (see Fig. 10A), considerably less than any other published value, and  $\sim 0.4$  eV below the experimental value mentioned above. The diffusion coefficient prefactor, determined by calculating phonon frequencies for the saddle point and the ground state, is 0.00377.

The second diffusion path is illustrated in Fig.9. In this series, the upper nitrogen atom in Fig. 9A stays put while the other takes a round-about path towards the upper right before rejoining its partner. Here, the highest energy configuration of Fig. 9B, (see Fig. 10B for the relative total energy) happens when the two nitrogen atoms are closest together, in contrast to the previous series. The mobile nitrogen atom then moves out and around to a metastable low-energy configuration, see Fig. 9D, that once again resembles the Humble model without actually assuming that configuration. An energy barrier of 3.8 eV separates the original and metastable configurations, while a smaller barrier of 1.3 eV separates the metastable stage from the final configuration. At the saddle point, one nitrogen atom is four-fold coordinated while the other's fourth nearest neighbor is only  $2.71 \text{Å}$  away, see Table 1. The metastable state (stage 4) in the path, on the other hand, has nitrogen bond lengths that are quite similar to the lowest energy configuration. The interesting thing about this diffusion path is that only one atom is required to be excited, as opposed to other models (the previous model or those presented in [9]) that require both nitrogen atoms to pass through an energy barrier. If thermal energy is plentiful in a material then it would not be unusual to have two mobile atoms, whether they move disjointedly or in tandem. On the other hand, atomic excitation by collision, *e.g.* in ion or electron bombardment, might be more likely to

result in a single atom doing all of the moving. This difference in likelihood is borne out by a higher diffusion prefactor for the second diffusion path, with a value of 0.0248.

### 3.4 Discussion

The most significant way in which these diffusion paths differ from those previously reported is that they are unconstrained with respect to the preservation of symmetric arrangements, but instead follow non-obvious detours to maintain lower energy. It is not of serious concern that the low value for the first diffusion mechanism does not match with the experimental value, since error bars in this type of calculation can be as high as 0.4 eV. Given that previous authors' calculations have used the same inherent assumptions in their models, the fact that this new path has a lower value must make it the preferred route. Finally, nitrogen is known to introduce deep levels into the electronic band gap; this is the reason that it does not work as a dopant in silicon.<sup>39</sup> Due to the band gap problem in density functional theory calculations, this introduces the potential for sizable error bars, despite attempts to correct for it.<sup>38</sup>

### 3.5 Conclusion

Overall, we believe that, due to the energetics of the low activation energy diffusion path presented here, this mechanism should be a strong contributor to the diffusion of nitrogen, especially at elevated temperatures where the two atoms could move disjointedly in a short time period without falling back from the saddle point into their original configuration. The high activation energy diffusion pathway seems feasible and could be more likely than its 3.8 eV activation energy would suggest, since only one of the atoms is

required to move. A future study should explore these different paths competitively and at different temperatures to get a closer idea of the dynamics and temperature dependence of nitrogen pair diffusion.

## 4 Anomalous Nitrogen Diffusion during Ion Milling: a SIMS Study

Submitted to Journal of Applied Physics as “Segregation and Enhanced Diffusion of Nitrogen in Silicon Induced by Low Energy Ion Bombardment”, by N. Stoddard, G. Duscher, A. Karoui, F. Stevie and G. Rozgonyi, February 2004

### 4.1 Introduction

Surface processes are ubiquitous in the semiconductor industry. Ion milling is used for sample thinning, and etching, and in the creation of specialized structures.<sup>40,41</sup> It is also a key part of the process to create thin foils for use in transmission electron microscopy. Mechanical and chemical-mechanical polishing techniques are commonplace in any semiconductor processing facility. One chief assumption in the use of these techniques is that the resulting near-surface region is similar to the bulk material. For TEM specimens, the hope is for the thin foil samples (almost always less than 100 nm thick, typically less than 10 nm thick) to have the same properties as the original bulk wafers. It has been established that ion beam processes at moderate to high energy ( $> 5$  keV) and incident angles greater than  $15^\circ$  from the surface can cause significant damage in terms of point defect aggregates, amorphization and even phase changes in the sample.<sup>42</sup> In general, it is believed that using low energy, low angle conditions in ion milling minimizes the incidence of these defects. In this paper, however, it will be shown that significant segregation effects occur in the N-Si system during ion milling, even under optimum conditions, and that diffusion of N to a depth of several microns is possible, despite the low energies involved. First, the different surface processes will be described. The order of processes used here will correspond to the order used in TEM sample preparation. A representative TEM sample preparation process is

illustrated in Figure 12 involving mechanical polishing and dimpling, and subsequent ion milling.

## 4.2 Materials and Methods

Two sets of samples were studied. The first set (Set A) represents the different stages in TEM sample preparation: polishing, dimpling, and ion milling, carried out on nitrogen-doped, Czochralski grown silicon wafers manufactured by Wacker-Nippon Silicon. They have a bulk nitrogen concentration of  $1 \times 10^{15}$  atoms/cm<sup>3</sup> and an oxygen concentration of  $7 \times 10^{17}$  atoms/cm<sup>3</sup>, as measured by SIMS. Of these, full thickness pieces were cleaved to ~1 cm on a side and measured in four states: 1) no processing (original 760  $\mu$ m thickness), 2) rough and fine mechanical polishing to 200  $\mu$ m, 3) rough and fine dimple grinding to an end thickness of 100  $\mu$ m, and 4) ion milling in each of two ion mills: a Gatan 656 DuoMill and a Fischione 1100 ion mill. It should be noted that the ion-milling was not intended to create a hole, and the sample never came to a thin-foil state. For these bulk samples, ion bombardment was from one side only. Separately, a 3 mm piece from the same wafer was prepared as a TEM foil, see Fig. 13, using the various thinning processes described above. Ion milling was done on both sides simultaneously in the Gatan mill. A hole was created and a thin-foil region can be found around it. The SIMS measurement sites are numbered (1) – (8). Note that an area of rough dimple grinding can be found containing craters (6) and (7), where the sample broke during dimpling on a failed sample preparation sequence. A second set, B, of Cz-Si samples comes from Agere Systems and has no grown-in nitrogen, but instead has nitrogen introduced either by ion implantation of  $10^{15}$  cm<sup>-2</sup> of 100 keV <sup>14</sup>N<sup>+</sup> ions

or by thermal nitridation of the top  $10\text{\AA}$ . The observed values for projected range and straggle distance of the implant are 300 nm and 130 nm, respectively. According to theory,<sup>43</sup> each N atom creates an average of 817 Frenkel Pairs, or  $4.4 \times 10^{22}$  FP/cm<sup>3</sup>. This is enough to amorphize the 450 nm between the surface and  $R_p + \Delta R_p$ . These samples had no heat treatment and were ion-milled directly, on the top side only. Set B samples were ion milled in the Fischione ion mill, and the nitrogen-implanted samples were ion milled with and without liquid nitrogen cooling.

Polishing was performed using a Buehler Ecomet polisher with SiC pads whose grits range from 400 to P4000. The final polishing step was a chemical/mechanical polish involving a cloth pad and Syton NaOH colloidal fluid from MEMC. Dimple grinding was done on a Gatan 656 Dimple Grinder using a brass wheel with 3  $\mu\text{m}$  diamond paste and a cloth wheel with 0.05  $\mu\text{m}$  diamond paste. SIMS analysis was performed by the NCSU Analytical Instrumentation Facility using a CAMECA IMS-6F Secondary Ion Mass Spectrometer with a  $\text{Cs}^+$  primary beam and detection of negative secondary ions, primarily  $\text{SiN}^-$ . Depth profiles were performed with the settings designed to attain the best detection limit using a raster-reduction technique to improve nitrogen detection limit and differentiate small signals from redeposition of sputtered material.<sup>44</sup> A primary current of 400nA was used to sputter a region of  $200\mu\text{m} \times 200\mu\text{m}$  and secondary ions were detected from a  $60\mu\text{m}$  diameter region at the center of the raster. The raster was reduced to  $90\mu\text{m} \times 90\mu\text{m}$  and detection limit of approximately  $4 \times 10^{14}$  atoms/cm<sup>3</sup> was obtained for nitrogen.

### 4.3 Results

Table 2 provides the average nitrogen concentration for the first five to ten microns for the different samples of set A. The bulk nitrogen concentration in the N-doped samples is  $1 \times 10^{15} \text{ cm}^{-3}$ ; ion milled samples are measured to have  $10^{16} \text{ cm}^{-3}$ , and the depth profiles for measurements on the TEM foil, see Fig. 14(a), were consistent with those on bulk samples, see Figs. 15(a) and 15(b). Rough grinding, see Fig. 14(b), introduced the largest impurity concentrations, which are probably particulate residue from the polishing compound. Inspection of the sample using the scanning ion image during SIMS analysis revealed particles of  $\sim 5 \text{ }\mu\text{m}$  diameter whose carbon/nitrogen concentration was estimated to be on the order of  $10^{20} \text{ cm}^{-3}$ , in order to produce the average concentration of  $5 \times 10^{17} \text{ cm}^{-3}$ . Whatever the cause, the subsequent fine-polishing process, which occurs before ion milling, erases the elevated concentrations and erodes the sample without any nitrogen accumulation. In fact, the end concentration in the finely polished samples was actually slightly lower than the bulk value. It should be noted that, in Figs. 14(b) and 14(c) the raster reduction technique was used at  $\sim 9 \text{ }\mu\text{m}$  and  $1.7 \text{ }\mu\text{m}$  depths, respectively. The silicon secondary ion yield increases at those depths due to the collapse of the ion bombarded area to a smaller size. The nitrogen level in Fig. 14(c) demonstrated a similar increase in raw data, but is calibrated, normalized to the silicon increase, to show true concentration. Because it increases in step with the silicon (so that the calibrated signal remains constant), the nitrogen signal cannot be due to redeposited material and must originate from the sample. In Fig. 14(b), however, there is a significant drop upon raster reduction, indicating that most of the signal at that depth is due to material redeposited from the erosion of the shallower depths.

While the data on polishing is interesting, the key effect is the elevation of the concentration due to ion milling. Craters (1) and (2) of the Gatan milled TEM foil had concentrations of  $10^{16} \text{ cm}^{-3}$ . On all ion-milled samples from Set A, as you move away from the center of the ion-milled area, the concentration decreases smoothly towards baseline values. The sharp rise at the end of the crater (2) profile, see Fig. 14(a), is due to break-through, where a hole was actually created. Before break-through, however, there is a significant rise in the concentration as the backside is approached. It should also be noted that the concentration remains significantly elevated through several microns despite the shallow (tens of angstroms) interaction depth of ion milling. The introduction of nitrogen deep into the sample indicates an active mechanism for long-range diffusion. The thin foil nature of the TEM sample apparently was not a significant factor, since the bulk ion milled samples demonstrated similar behavior. Upon raster reduction, all of the samples in Set A demonstrate an increase in secondary ion yield, indicating actual nitrogen in the sample. The effect is not limited to a specific type of ion mill, since an older Gatan model with diffusion pump and a newer Fischione model with a turbo-molecular pump had almost identical results, see Figs. 15(a) and 15(b).

The data from the samples of Set B is shown in Figs. 15(c) and 15(d). Here, we see that any drive-in by ion-milling through the ion-implanted region is minimal. This result was independent of milling temperature and time in the ranges of  $-70$  to  $50^\circ\text{C}$  and one to three hours. It should be noted that the raster-reduction method, when used on the ion milled samples of Set B, did not show an increase in counts/second of SiN, indicating that the nitrogen signal was not originating from the sample, but from redeposition from residual gas in the vacuum system. Note that the concentration of nitrogen is much lower than for the

samples in set A and approached the detection limit in the  $10^{14}$  atoms/cm<sup>3</sup> concentration range. The results for the nitride layer, see Fig. 16, were slightly different. While the nitrogen level drops at 3  $\mu\text{m}$  where the raster size is reduced, which indicates some signal originating from redeposition, the signal is stronger than with the implanted sample. There may be a mix of signal from redeposition with a small but real signal.

#### 4.4 Discussion

The difference in behavior between the nitrogen-doped and nitrogen-implanted samples can be explained. The nitrogen in the implanted samples is associated with a region of ion implantation damage. Both amorphous silicon and dislocations will tend to trap the nitrogen with high solubility, compared to the low solubility of defect-free crystalline silicon. This trapping will prevent the nitrogen from being driven into the sample, allowing it to be sputtered normally with the rest of the material. The lack of significant drive-in for the nitrated sample can perhaps be attributed to the very shallow distribution, with only 10 $\text{\AA}$  of nitride. The effective volume of cascades from the Argon ion milling is around 20  $\text{\AA}$ , so the nitride may have been removed before the nitrogen could escape deeper in the sample. It is conceivable that thicker surface concentrations might perform more favorably.

The explanation for the ion milling drive-in effect observed in the silicon whose nitrogen was introduced during crystal growth requires one to consider the source of the extra nitrogen observed. A few possibilities present themselves: *i*) that it is introduced from the vacuum, *ii*) that there is a build-up of the nitrogen already in the sample, and *iii*) that it is driven in from surface concentrations. First consider introduction from the vacuum. During ion milling in either machine, the vacuum is better than  $5 \cdot 10^{-6}$  Torr, so at any given time

there would be a total of  $\sim 10^9$  atoms/cm<sup>3</sup> present in the ambient. If the nitrogen were being introduced by the ion milling, there is no reason why similar nitrogen-free silicon samples would not experience the same nitrogen buildup: both the implanted silicon and the nitrided silicon showed nothing of the sort once the top nitrogen-rich layers were removed.

Next, consider the mechanism of buildup from a ‘snow-plow’ effect of nitrogen in the bulk of the sample. The behavior is determined by a combination of mass conservation and segregation efficiency. Once again, the extremely optimistic case will be considered, where the segregation coefficient is unity. Figures 14(a), 15(a) and 15(b) show an average concentration of  $8 \times 10^{15}$  cm<sup>-3</sup> over a depth of 8  $\mu$ m. For the nitrogen to come from the sample at a bulk concentration of  $1 \times 10^{15}$  to  $2 \times 10^{15}$  cm<sup>-3</sup>, a depth of 32-64  $\mu$ m should have been ion milled. In reality, at most 10  $\mu$ m of material was ion milled, so this mechanism is not sufficient to explain the results either.

The final possibility is that some surface contamination existed that was driven in by the ion milling process. According to the above results, this contamination would have to be significantly deeper than the 10 Å nitride layer that was examined. This mechanism is difficult to quantify, but in the worst case, nitrogen-rich surface layers might be present with  $\sim 1 \times 10^{22}$  atoms/cm<sup>3</sup>, or  $\sim 5 \times 10^{14}$  atoms/cm<sup>2</sup>. In order to have enough material to drive in  $10^{16}$  cm<sup>-3</sup> of nitrogen through an 8  $\mu$ m thick volume with a segregation coefficient of 0.01, a nitrogen-rich layer thickness of 8 nm would be needed. This thickness is at least reasonable, both because it is not unrealistically thick and since it is considerably larger than the ion milling interaction volume, which allows time to escape into the bulk (unlike the nitride sample). Comparing Fig. 14(a) and Fig. 14(c), there is a surface peak before ion milling that is not there after ion milling. This mechanism seems in theory to be capable of introducing

the largest amounts of material, but our attempts to verify it with surface nitrogen profiles from implantation and thermal nitridation were unsuccessful. Support for the presence of higher levels of nitrogen in the near-surface layers can be found in the reports of Karoui et al., where SIMS N and O simultaneous depth profiling and imaging suggested that N and O pile up at the subsurface during wafer polishing.<sup>45</sup> They claim that, during polishing, the applied stresses from nano-scratches and dislocation micro-loops getter nitrogen which in turn drag oxygen.

Independent of the mechanism of introduction, there is a second question as to how the nitrogen moves through such a large depth. The thermal budget of nitrogen during ion milling (<100°C, 3h) is insignificant, so some type of enhanced diffusion is operating. One possibility is the Crowdion mechanism of diffusion, where a series of atoms in a close-packed direction slide together, pushing the last in the line into an interstitial position. Since the N<sub>2</sub> complex occupies a split-interstitial position, both direct Crowdion events and increased interstitialcy would enhance diffusion. The Crowdion mechanism is particularly active in ion-milling type processes, where collisions at the surface can create interstitials and diffusion events deep in the sample. In general, the diffusion phenomenon seems to be exotic and it is likely that other complementary mechanisms need to be examined.

#### 4.5 Conclusion

Surveying the different surface techniques that have been considered, rough thinning processes generally introduce highly impurity-rich embedded particles while subsequent fine grit processes remove these constituents and succeed in producing a near-surface in the first several microns that is similar to the bulk. Work by A. Karoui [to be submitted] has shown

that CMP processes can still create extraordinary nitrogen concentrations within the first micron. The ion milling process, however has been shown to induce significantly elevated levels of nitrogen (up to 10X the bulk value) in the first several microns. It has been shown above that this magnitude of change to a TEM sample can significantly affect TEM analysis. There should also be some impact on devices created in nitrogen-doped silicon that involve reactive ion etching, although that has yet to be studied. Two significant phenomena have been observed, however. First, a segregation mechanism is operating to accumulate the bulk nitrogen and to incorporate nitrogen driven in from the first few nanometers of the surface. Second, an unusual diffusion mechanism is causing the segregated nitrogen to diffuse through several microns of the sample despite a small thermal budget. The Crowdion mechanism has been suggested to explain the nitrogen diffusion, but more investigation is needed to clarify the causes of these two phenomena.

## 5 The Nucleation and Growth of Extended Defects in Silicon from their atomic constituents

Submitted to Physical Review B as “Inducing the Nucleation and Growth of Extended Defects at Room Temperature in Silicon by 200kV Electron Irradiation” by N. Stoddard, G. Duscher, W. Windl and G. Rozgonyi, June 2004.

### 5.1 Materials and Methods

[100] oriented, as-grown N-FZ and N-CZ plan-view samples were prepared by conventional TEM thinning methods, which include grinding, polishing, dimple grinding and ion milling. Siltronic Corp. grew the N-CZ starting material while the N-FZ sample came from the National Renewable Energy Labs. The N-CZ sample has bulk light element impurity profiles of  $[O] = 7 \times 10^{17} \text{ cm}^{-3}$  and  $[N] = 10^{15} \text{ cm}^{-3}$  while the N-FZ sample has  $[O] = 10^{15} \text{ cm}^{-3}$  and  $[N] = 10^{15} \text{ cm}^{-3}$ . Samples from these wafers were prepared for TEM analysis by mechanical polishing, dimple grinding and ion milling with 3-5 keV  $\text{Ar}^+$  ions at 5-6 mA. It has already been shown that this type of sample preparation can result in enhanced bulk nitrogen concentrations of up to  $10^{16} \text{ cm}^{-3}$ . Separately, a piece of the sample of the as-grown N-CZ Si was annealed using a hi-lo cycle of 8 hours at 750°C and 16 hours at 1050°C. It was prepared as a cross-sectional TEM sample and [110] oriented for irradiation. All electron irradiation was performed at 200 kV in JEOL 2010F and Topcon 002B electron microscopes, while high-resolution imaging, EELS, and scanning TEM (STEM) in Z-Contrast and bright field modes were performed on the JEOL instrument. It should be noted that contamination issues during the irradiation are minimized because the samples undergo plasma cleaning

every time they are placed in the microscope, and Z-contrast analysis is typically done at a different time than the irradiation.

Simulations were performed using the Vienna *Ab Initio* Simulations Package (VASP), which employs a self-consistent approach based on density functional theory in the local density approximation. Ultra-soft pseudopotentials with a plane-wave basis set were used both for ionic relaxation and for calculating the total energy at different points along the diffusion path. A perfect supercell of 64 silicon and two nitrogen atoms, *i.e.* eight unit cells, was first relaxed with the well-known N<sub>2</sub> structure consisting of two nitrogen and two silicon atoms in a square configuration in the [110] direction. A similar configuration with the nearest silicon atom to the N<sub>2</sub> pair situated in a near-by interstitial position was relaxed, and four to six intermediate positions between these two were interpolated as starting guesses for nudged elastic band calculations. Each of the intermediate steps was then locally relaxed along its hypertangent to a total energy tolerance of 0.005 eV. Only the neutrally charged case is considered, since in other work the energy difference between negative and neutral charge states was negligible while the positive charge state had higher energies by a constant energy shift.<sup>18</sup>

## 5.2 Results

Figure 17 depicts a N-CZ Si sample in both bright field and Z-Contrast modes of the STEM. The dark and light arcs visible in A) and B), respectively, delineate the boundary of the irradiated region. The irradiation was positioned near the edge of the TEM foil for best results in Z-Contrast and EELS modes of the TEM. In Z-Contrast images B), C) and D), the low signal dark areas correspond to a high concentration of vacancies, while the high signal

bright areas are denser (*i.e.* interstitial rich) or thicker, as was the case in Fig. 4. As was noted earlier, Z-Contrast image features are generally due to differing elemental distributions (based on atomic number  $Z$ ), varying sample thickness or density fluctuations.<sup>36</sup> Since this sample is pure CZ silicon (the nitrogen influence is negligible), we can attribute the contrast to local Si density variations due either to vacancies or silicon self-interstitials, local thickness differences or the presence of extra layers of oxide. It should be noted that silicon dioxide is very close in mass density to normal silicon, but since RBS goes as  $Z^2$ , an oxide layer will give less signal than an equal thickness of silicon. If, on the other hand, extra oxide thickness is on top of an equal thickness of silicon, the signal will be additive and give higher contrast to this region. Previously, secondary phases were observed but not identified. Here, as in Figs. 17C and 17D, EELS chemical analysis shows that high oxygen concentrations exist both inside the large irradiated region and in a speckled ring just outside of it. It is logical that the elastic collisions resulting from TEM electron bombardment will greatly enhance oxygen diffusion in the same way that silicon interstitial diffusion is enhanced. For oxygen diffusing in a vacancy-rich environment, the eventual result will be clustering and precipitation. Ripening of oxygen clusters inside the irradiated zone has been observed as longer irradiation times are used, a process that competes with diffusion out of the beam volume. While nitrogen concentrations were too small for measurement by EELS, the oxygen is readily detected and has some dramatic effects. Consider, for example, the two large bright spots in Figs. 17C and 17D. The sharply defined EELS spectra, see Fig. 17E, for the boxed area in Fig. 17C clearly indicates the presence of pure silicon dioxide, based on the sharp peak at 106 eV. Within the Si L-edge profile, the first sharp peak corresponds to stoichiometric silicon dioxide while the second peak relates to the strong presence of

interstitial oxygen. The Fig. 17C particle has fairly distinct boundaries, while the bright area in 17D has softer edges and is a mix of silicon with interstitial oxygen and silicon dioxide, as indicated by its EELS spectrum. No particle like either of these two was found elsewhere in the sample, *i.e.* outside of the irradiated zone, and they were not present before irradiation. As such, they must be attributed to e-beam-induced clustering and precipitation.

In nitrogen-doped, low oxygen float zone silicon, there exist differences in the response to irradiation, compared to the CZ material. Instead of the aggregation of oxygen, we observed void formation due to the agglomeration of vacancies during irradiation. Evidence of this phenomenon can be found in Figure 18. First, it should be noted that the three bright spots in Fig. 18B are due to carbon contamination while the converged Z contrast e-beam rested in spot-mode at those positions. Even though carbon has a lower Z than silicon, these spots appear bright because of the thickness of the carbon added on top of the sample thickness. The sample material in Fig. 18 is N-FZ Si, and the concentration of oxygen is a factor of 1000 less than in the N-CZ material. For this reason, oxygen precipitation is not expected, and no evidence of clusters can be seen in Fig. 18B. Instead, closer examination of the irradiated area in Z contrast mode reveals small dark features, see Fig. 18C. By the same logic as is used above, these can only be aggregates of vacancies. Their triangular appearance when viewed in high resolution suggests that the voids are somewhat faceted and vary in size from 2-5 nm, see Fig. 18D. Evidently, nitrogen-doped FZ silicon exhibits the same separation of interstitials and vacancies described above for N-CZ samples, but without the oxygen clustering. The irradiated area appears in Fig. 18B as a dark circle whose weaker contrast corresponds to a lower concentration of silicon atoms, *i.e.* a higher concentration of vacancies. In this case, the vacancies have had sufficient time to

aggregate into voids. A diffuse brighter halo of excess interstitials surrounds the dark circle, as was the case for N-CZ Si. In addition to the halo, faint bright lines can be seen directed radially away from the ring, and corresponding to the open (110) directions. The implication of this result is that the interstitial diffusion can continue outside of the irradiated region in certain directions. This is not necessarily surprising since the sample is maintained in the TEM at a temperature below 350K, while diffusion of silicon self-interstitials has been reported below 100K.<sup>5</sup> It is also a reinforcement of the bulk nature of the diffusion, since channeling along (110) directions is a significantly weaker phenomenon in surface diffusion.

The results of different intensities of irradiation are found in Figure 19. In 19A, a hole has been created by intense convergent beam irradiation of the N-CZ Si thin foil. This type of hole formation by electron irradiation has been widely observed in thin film silicon samples, and is generally attributed to surface diffusion.<sup>46</sup> The interesting result here is that a stacking fault has nucleated in close proximity to the hole, presumably formed from atoms diffusing in the bulk by interstitial paths away from the beam. With a beam of ~60 nm diameter, as in Fig. 19B, amorphization of the silicon crystal occurs but a hole is never formed. The amorphous nature of the irradiated region is verified by convergent beam electron diffraction patterns (inset), where the crystalline diffraction contrast is mostly lost in the irradiated area.

Finally, the electron knock-on process in nitrogen-doped silicon was studied using a nudged elastic band calculation. The configurations along the path of the knock-on event are shown in Figure 20, while the energetics can be found in Fig. 21. The initial configuration is the well-known and very stable N<sub>2</sub> configuration, see Fig. 20-1; one of its nearest neighbors is then displaced on a path towards the final configuration on a nearby tetrahedral interstitial

site, see Fig. 20-11. There are two saddle points along this path: at 4.2 eV above the ground state in Fig. 20-5 and at 6.2 eV above the ground state, found in Fig. 20-10. Two of the configurations (6 and 9 in Fig. 21) are omitted because they provide no interesting information. The excited atom, highlighted in yellow, moves away from the N<sub>2</sub> pair. Meanwhile, a nearby atom is drawn in to re-form a [110]-oriented N<sub>2</sub> square, see the white star in Figs. 20-3 to 20-5. Configuration 20-5 is a local saddle point, proceeding to a local minimum in 20-8. In the series from 20-5 to 20-11, the atom indicated by the black star is kicked out to accommodate the excited atom, and in Fig. 20-8, the system is very close to reverting to the original configuration with three atoms exchanged. If the excited atom (highlighted) does not have the energy to move through the saddle point of Fig. 20-10, there would be no observable change and no net damage. In the case that the excited atom moves to the final configuration, the atom indicated by the black star determines where the vacancy ends up; the lower energy configuration, shown in 20-11 is for a VN<sub>2</sub> complex to form. This is the first configuration that is stable against reversion to something equivalent to Fig. 20-1, with a 1 eV energy drop from 20-10 to 20-11. The total formation energy for the final configuration is 5.3 eV. To evolve the system one step beyond 20-11, a similar calculation was carried out to find the energy barrier between this interstitial position and the next interstitial position, one step farther from the N<sub>2</sub> pair. To get the excited atom farther away, a supercell of twice the size, 128 atoms, was used with 64 atoms of pure Si added. The energies of the initial and final interstitial states are within 0.2 eV, with an intermediate saddle point at 1 eV higher energy than 20-11. This value for the migration barrier energy is still higher than for bulk diffusion, indicating some residual pull on the interstitial atom.

### 5.3 Discussion

The surface is a consideration that must be taken into every interaction in a thin foil. In this case, it might be tempting to explain the effects noted in Figs. 4, 17 and 18 as surface related. The argument would be that only the atoms on the surface are being manipulated to move outside of the beam, and that the resulting thickness variation causes the ring-shaped contrast. In the case of the oxide formation in Fig. 17, one might surmise that the silicon dioxide particles have simply coalesced from the native surface oxide. For Fig. 18, the dark spots could be faceted [111] surface pits, once again the result of surface manipulation. There are several problems with these arguments, however. First of all, there is the question of reference samples. It was previously mentioned that nitrogen-free samples have essentially no response to irradiation with beams larger than 20 nm in diameter. In some N-free samples, slight stress contours were discernible after irradiation, but in most even this was lacking, and in no N-free sample were there features like those in the Z contrast micrographs. In the study by Yamasaki and Takeda[31], damage could only be created in Si under 200kV irradiation by cooling the sample down to 15K. The only difference between the N-free reference samples (similar to those used in [31]) and the N-doped samples was the bulk nitrogen concentration, so that the fundamental interaction during irradiation is indicated to occur at the bulk nitrogen sites. Secondary Ion Mass (SIMS) depth profiles have demonstrated that the nitrogen concentration after TEM sample preparation is uniformly distributed at a level of  $\sim 10^{16} \text{ cm}^{-3}$ . Concerning the arguments about thickness differences, attempts have been made to profile the topography of the irradiated surface using atomic force microscopy, but no surface topography was observed on either the top or the bottom of the TEM samples. As for the question of oxygen precipitation, it cannot be ruled out that the

surface oxide has some response to irradiation. In fact, irradiation under a tightly converged beam often causes obliteration of the surface oxide. In Fig. 17D, however, the energy-loss spectrum of Fig. 17E tells us that interstitial oxygen is piled up here, and this interstitial oxygen would have had to move by bulk diffusion. A similar situation is found in Fig. 19, where stacking faults have nucleated near a hole that was created during irradiation by a 2-3 nm converged electron beam. Holes like this are readily observed as a result of converged-beam irradiation in silicon thin foils, and it is often assumed to be an artifact related to surface diffusion. In this case, however, it is not possible for the stacking fault to have been nucleated by atoms diffusing along the surface because there is no driving force outside of the beam to force surface atoms into the bulk. Instead, atoms kicked out of their lattice sites have diffused in the bulk via interstitial pathways, and aligned themselves so as to lower the local energy. While some surface diffusion cannot be ruled out, it is likely that the two mechanisms compete during irradiation. In the case of Fig. 19B, however, there is no way for amorphization of the sample to occur through surface rearrangement. This result can only be explained by a bulk interaction at a high rate of damage accumulation. In N-free Si, amorphization was never achieved with a 200kV beam, even at 15K and with electron doses of  $10^{23} \text{ cm}^{-2}$ , but the nitrogen interaction proves here to be strong enough to facilitate breakdown of the crystal structure through repeated interaction with the silicon point defects.

It was noted earlier that the hole creation process in Fig. 19 does not involve nitrogen in the creation of vacancies that eventually grow to be a hole. It was determined that, based on Rutherford scattering, a 200kV electron can impart up to 18 eV of energy to a silicon atom, see above. First principles calculations indicate that the knock-on energy to create a stable V-I pair in silicon ranges from 11-20 eV, but that Frenkel pairs created at the lower

end of this energy range tend to quickly recombine in molecular dynamics simulations of the final configuration at room temperature. It is likely that this knock-out/recombination process occurs regularly during routine TEM analysis. Consider that, under typical conditions of the Topcon 002B TEM beam exposure (*i.e.* 10  $\mu\text{A}$ , 400 nm beam diameter),  $\sim 3.1 \cdot 10^5$  electrons will flow through an area of  $0.0625 \text{ nm}^2$  every second.\* Based on the graph presented in Fig. 3, the probability for each individual electron to impart more than 15 eV to one silicon atom is  $P \approx 0.0000025$ .† Calculating the probability for interaction in one second as one minus the probability that none of the electrons will interact,

$$P(1s) = 1 - (1 - P(1e^-))^{310,000} = 1 - 0.9999975^{310,000} \approx 0.54$$

the result is close to a coin toss. Using the same expression, the probability of an electron imparting the maximum possible energy (18.6 eV) to one of the atoms in a 100 nm thick column in 1s is 0.79! Our conjecture is that permanent separation requires a second electron collision to occur before the Frenkel pair recombines (in the absence of nitrogen). According to simulations, recombination of the V-I pair within 100 ps is quite likely. However, in either the Topcon 002B or the JEOL 2010F microscope with a beam diameter of 100-400 nm, the probability of *any* electron passing by a particular place in a period of 100 ps is  $3.1 \cdot 10^5 \text{ e}^-/\text{s} \cdot 10^{-12} \text{ s} \approx 0.00001$ , and much less that an electron that will impart significant energy to the displaced atom. Under these broad-beam irradiation conditions, recombination should dominate. Hole creation is usually observed at a beam diameter of  $<5 \text{ nm}$ , where the picture changes dramatically. In the JEOL 2010F, with  $1 \mu\text{A}$  of beam current flowing through an area  $\sim 2 \text{ nm}$  in diameter, there will be  $\sim 12$  electrons passing through each

---

\* This area is  $\frac{1}{4}$  the area of one side of the Si unit cell, about the interaction area of a beam electron

† This is the probability for interaction in 1nm thickness, 0.00001, divided by the 4 atoms in  $\frac{1}{4}$  of the unit cell area over two unit cells' thickness

0.0625 nm<sup>2</sup> every 100 ps, so that a second low energy collision to further separate the Frenkel pair before recombination becomes a real possibility. The repetition of this process over several tens of seconds results in the observed rapid out-diffusion of silicon atoms from the irradiated volume via bulk and surface diffusion.

The results of the nudged elastic band calculation add an interesting follow-on to the discussion of knock-on processes. It appears that the N<sub>2</sub> defect causes the barrier to Frenkel pair creation to be lowered from the reported range, 11-20 eV, to a value around 6 eV. For argument, let us take a moderate value for the displacement energy of  $E_d = 15$  eV. In Fig. 3, the nitrogen-enabled knock-on energy has a higher probability,  $P = 0.00015$ , than the 15 eV event with  $P = 0.00001$  by a factor of 15. In the course of 1s irradiation, the probability of a nitrogen-enabled V-I separation at any particular N<sub>2</sub> site is near unity, but the probability of an event in pure silicon is still 0.54 for every atom, and there  $\sim 10^6$  as many bulk silicon atoms as there are silicon atoms near an N<sub>2</sub> pair, so the pure silicon interaction should still be more prevalent. Therefore the calculated lowering of the energy barrier to Frenkel pair formation is not sufficient to account for the dramatic difference in response to irradiation between nitrogen-doped and nitrogen-free samples. Two alternative arguments can be made. First, one could argue that the effective value of  $E_d$ , accounting for a temperature dependence of the spontaneous recombination volume, is actually above 18.6 eV at room temperature. This properly explains the damage observed at 15K under electron irradiation, but is not entirely satisfying since the process of hole formation as explained above makes it clear that even the fastest recombination events can be disrupted given the right conditions. Instead, to properly account for the observational differences, one must look to the stability of the damage configuration.

The N<sub>2</sub>V-I configuration of Fig. 20-11 has been shown to have an energy barrier of 1eV against reversion to the ground state, which is well above the thermal budget (<0.1eV) available during irradiation. Since the pure V-I pair apparently recombines spontaneously during RT irradiation, it is reasonable to conclude that its energy barrier to recombination is on the order of the thermal energy, ~0.03eV. Therefore the nitrogen-related Frenkel pair is considerably more stable than the pure Frenkel pair, allowing time for a subsequent electron collision to further evolve the system. Concerning this second event, the energy barrier to move an interstitial from the configuration of Fig. 20-11 to the next-nearest interstitial site is also 1 eV. This is still higher than the thermal budget (and the value for interstitial migration), and so a second electron collision is needed. Even though the energy barrier to forward diffusion is almost identical to that for reversion, the probability for a beam electron to stimulate forward momentum (consistent with direction of momentum of the e-beam) is orders of magnitude greater than that to cause backwards momentum. Ultimately, the moderate stability of the new defect is the key ingredient that enables self-interstitial migration away from its vacancy and the resulting damage accumulation that is observed in Figs. 4, 17 and 18.

This theoretically determined energy barrier can now be used to estimate the probability and prevalence of the proposed N<sub>2</sub>-assisted kick-out mechanism under real irradiation conditions. Using the value quoted above, ~3.1\*10<sup>5</sup> electrons pass through a ¼ unit cell area every second during typical irradiation. From Fig. 3, each electron has a probability of 0.00015 to transfer more than 6.2 eV to a silicon atom in a 1 nm thickness, so that each atom has a P = 0.0000375 chance of interacting with each electron passing within a

0.1 nm radius. Within one second,  $3.1 \times 10^5$  electrons will pass within this cross-section, so the probability for interaction per second is

$$P(1s) = 1 - 0.9999625^{310,000} \approx 0.99999134$$

The relative concentration of nitrogen in the silicon is  $2 \times 10^{-7}$ , and each nitrogen atom in the  $N_2$  pair has two nearest neighbors, each of which is quite likely to receive enough energy to be displaced. Presumably, some recombination will occur as a result of subsequent electron collisions because the energy barrier to reversion is only 1eV, but the Frenkel pair is expected to be fairly stable against recombination when nitrogen is involved. The amount of damage is still likely to oscillate since the free interstitials may recombine with other vacancies as they diffuse. As interstitials occasionally and randomly leave the beam volume, however, vacancy defects will start to dominate under the beam while interstitial complexes can form just outside. In a cylindrical volume of 400 nm diameter and 100 nm thickness, there will be ~60  $N_2$  pairs in ion milled, as-grown material, so the extent of the observed damage is reasonable, even if each  $N_2$  pair is responsible for nucleating only one damage center.

Using this insight into the irradiation process, the geography of Fig. 17 can be explained from the point of view of diffusion and coarsening, as schematically illustrated in Fig. 22. First, the irradiation consists of fairly random electron stimulated diffusion events within a finite beam area, as shown in Fig. 22A. Therefore, a flux of silicon and oxygen atoms will leave the beam area near the periphery, while oxygen in the middle will tend to aggregate at nitrogen related complexes in the center and at favorable sites, such as the amorphous edge of the sample, as illustrated in Fig. 22B. The final picture, see Fig. 22C, has the central clusters consolidated and coarsened and a distinct ring of clusters around the edge

of the beam. This matches the observations of Figs. 17A and 17B, which focus on an area that was irradiated for 30 minutes. One might expect that further irradiation would eventually cause the oxygen rich particle to organize into stoichiometric silicon, which is apparently metastable under the beam.

Comparing the float zone and Czochralski samples, the dynamics of the competition of oxide precipitation with void formation should be controlled by the concentration of vacancies created relative to the oxygen concentration and by the nature of the irradiation. A schematic model of the nitrogen-enabled void/precipitate formation cycle is illustrated in Fig. 23. In the initial stages,  $N_2$  captures a nearby vacancy directly after the collision between an electron and a silicon lattice atom. The silicon atom is now on an interstitial position and cannot recombine with its lattice site. Subsequent electron collisions can provide enough impulse to cause the silicon to diffuse interstitially. The  $N_2V$  complex can now undergo the same process to become  $N_2V_2$ . From this point, it has been shown in simulations<sup>9</sup> that further vacancies can accumulate, or that  $N_2V_2$  can stably accumulate oxygen, forming N-O-V complexes that are believed to act as oxygen precipitate nuclei. Over time, each  $N_2$  pair could nucleate multiple extended defects by being electron stimulated to leave the now large defect that has been created, as in the last step of the cycle. The N-FZ Si sample has been shown to follow the vacancy accumulation route, see Fig. 18, while the N-CZ Si sample clearly has oxygen precipitation as the dominant phenomenon, although small voids may also form.

## 5.4 Conclusion

Looking at the results as a whole, there is significant evidence that bulk processes are active in addition to the usual surface processes. Firstly, all of these phenomena are unique to silicon with bulk nitrogen doping. Since the effects are absent in nitrogen-free silicon that is otherwise identical, the chief irradiation process must occur in the bulk at nitrogen sites. It is possible that the dark spots in Fig. 18C are due to vacancies that aggregate at the surface to form pits along  $\{111\}$  planes, it is not of central importance whether the voids form at the surface as pits or in the bulk. Some combination of the two is perhaps the most likely. It has already been indicated that the channeling seen in Fig. 18B and the formation of a stacking fault and amorphized silicon in Fig. 19 strongly demonstrate the interstitial diffusion of silicon atoms.

There are many possibilities for studying nanoscale material properties using the room temperature electron irradiation technique demonstrated here. The formation of voids, oxygen precipitates, and stacking faults have all been induced by exposure to the electron beam. This method can be the basis for the manipulation of crystalline/amorphous layers and the nucleation of slip dislocations, as will be shown elsewhere. This represents a laundry list of point, line and plane defects that can be studied from the earliest stages of formation, at room temperature and *in situ* in the TEM. Even the spatially resolved identification of otherwise elusive point defects, such as vacancies, can be attempted with such a method. There are two aspects that set this experiment apart from the wealth of irradiation studies at high voltage (300kV and greater). First, a unique aspect of using 200 keV TEMs is that the electrons are limited by momentum conservation to transferring at most 20 eV of energy to a silicon atom, providing just enough impulse to create knock-ons, and not so much that

cascades of damage occur. Second, using converged beams of 50-400 nm diameter allows the separation of vacancy aggregates, which form under the beam, from interstitial aggregates that are expelled from the beam area. Thus the two types of defects can be studied separately. Interstitial diffusion is also enhanced by irradiation, but not unreasonably so, allowing nucleation and growth processes that usually occur only at high temperatures to be studied at room temperature and in an observation tool of the highest resolution with chemical analysis capability.

## **6 Study of Point Defect Complexes by Electron Energy Loss Spectroscopy and First Principles Simulations**

To be submitted to Journal of Electron Microscopy as “A Chemical Signature for Point Defects and Their Complexes” by N. Stoddard, S. Lopatin, R. Erni, R. Hennig, W. Windl, G. Rozgonyi and G. Duscher, August 2004.

### **6.1 Introduction**

Electron energy loss spectroscopy is an excellent tool for determining qualitative and quantitative chemical data with high spatial resolution. Absorption edges arise in the energy loss spectra due to excitations of core electrons whose energy is characteristic of its parent element.<sup>34</sup> The exact position of the edge can provide information on shifts in the energy of core levels or the electronic bands, while the shape of the edge reflects local bonding properties and the area under an edge is proportional to the relative concentration of that element.<sup>47</sup> It has been shown that the energy-loss near-edge structure (ELNES) can be simulated by calculating the angular momentum resolved density of states in the Z+1 approximation, where the ELNES signal for the atom of interest is determined by using the next atom to the right in the periodic table, and a total signal is built up by determining the excited DOS for all atoms of interest and averaging them according to the overall composition.<sup>48</sup>

### **6.2 Materials and Methods**

The material used in this experiment is single-crystalline float-zone silicon doped during growth with  $10^{15} \text{cm}^{-3}$  of nitrogen by the National Renewable Energy Laboratories. Float Zone material was chosen for its low oxygen concentration to avoid the interference of

oxygen precipitation or interstitial oxygen in the energy-loss spectra. The [100]-oriented, plan-view TEM sample was prepared by standard methods, *i.e.* polishing, dimple grinding and ion-milling. The samples were irradiated at North Carolina State University's Atomic Resolution Electron Microscopy Center in either a 200 keV Topcon 002B TEM with an LaB<sub>6</sub> filament and in a 200keV JEOL 2010F TEM with a Schottky field emission filament. Typical irradiation times varied from 2 minutes to 10 minutes with a beam current of 1-10  $\mu$ A and a beam diameter of 50-200 nm. Z contrast images were acquired using an HAADF detector with the JEOL 2010F in STEM mode while scanning a converged 1.8nm electron beam. Electron energy loss spectra were acquired with an image-filtered Gatan spectrometer with a CCD detector with 1.3 eV energy resolution and operating at a dispersion of 0.2 eV/pixel. EELS was also performed on a monochromated 200 keV Tecnai TEM/STEM at the National Center for Electron Microscopy (part of Lawrence Berkeley National Laboratory) which attained 0.2 eV energy resolution when operating at a dispersion of 0.01 eV/pixel. At NCSU, irradiation and analysis occurred within hours of one another, and the sample was typically plasma-cleaned in between. On the Tecnai microscope, however, areas of irradiation were at least several days old and the bright 'interstitial-rich' halo had significantly diminished.

Vacancies and silicon interstitials were simulated using the *Vienna Ab-initio Simulation Package* (VASP), which employs a self-consistent approach based on density functional theory in the local density approximation. Ultra-soft pseudopotentials with a plane-wave basis set were used both for ionic relaxation and for calculating the total energy and the band structure. A perfect supercell of 64 atoms, *i.e.* eight unit cells, was first relaxed to a lattice parameter of 5.385 Å, which is smaller than the actual lattice parameter of 5.43Å

due to imprecision in the exchange-correlation term that is well-known for the local density approximation. The defects were then inserted and the atoms were allowed to relax to a lowest energy configuration. For the silicon interstitial atom, both the tetrahedral site and the [110] split interstitial configuration were used. The electrons were then allowed to fully relax in a frozen lattice with a refined k-points sampling grid and an increased number of electronic bands. Simulated EELS spectra for each atom near the defect were then acquired by calculating the angular momentum resolved density of states in the  $Z+1$  approximation to account for core-hole effects in the near-edge structure<sup>48</sup>. The calculated spectra had 0.09 eV resolution which was convolved to resemble a 0.2 eV wide Gaussian probe.

### 6.3 Results and Discussion

The chief effect of irradiation in the nitrogen-doped sample can be plainly seen in Fig. 18B, a Z contrast image of an area irradiated for 10 minutes by a beam 160 nm in diameter. In Z-Contrast images, the signal is derived from electrons scattered via Rutherford back scattering (RBS) to a high angle and measured by an annular detector. Since elements with higher Z have stronger RBS, they provide a stronger signal, as do denser and thicker areas of the same elemental composition.<sup>36</sup> In Fig. 18B, the material is high purity silicon, so elemental contrast is ruled out. A thickness gradient, due to the wedge shape of the TEM sample, can be seen going from the lower left to the upper right of the micrograph. The beam leaves a dark circle whose weaker contrast corresponds either to a lower concentration of silicon atoms, i.e. a higher concentration of vacancies, or to lesser thickness of the sample. As was indicated earlier, it is believed that the main interactions occur in the bulk, and this point will be argued for the ‘vacancy-rich’ area a little later. A diffuse brighter halo

surrounds the dark circle, which is attributed to of an increase in silicon atoms in the form of excess self-interstitials. From previous analysis, there is good reason to believe that the 200 kV electrons are creating Frenkel pairs by knock-on collisions with silicon atoms. To clarify the nature of the effect, EELS spectra were acquired from both the dark and bright areas to examine band-structure and bonding information. Two representative spectra can be found in Figure 24. Here, the near-edge structure of the Si-L<sub>2,3</sub> edge makes it clear that a significant alteration to the lattice properties has occurred. Compared to the reference spectra, taken in areas removed from the irradiation but of the same sample thickness, there are significant and consistent shifts in the edge position of  $1.3 \pm 0.2$  eV and  $0.9 \pm 0.15$  eV, respectively, for the dark (vacancy-rich) and bright (interstitial-rich) zones. Important shape differences exist as well, with the initial peak at 95 eV wiped out in the vacancy-rich spectra, and the rest of the edge remains depressed compared with the bulk until 120 eV. For the interstitial-rich case, the initial peak is enhanced, and the subsequent dip is slightly more shallow, although the spectrum is almost identical to the bulk past 110 eV. For both the self-interstitial and the vacancy spectra, the important differences in the near-edge structure are found within the first 10 eV of the leading edge.

The spectra from the JEOL microscope do not give much detail in the first few eV of the Si L<sub>2,3</sub> edge. The same N-FZ Si sample was analyzed in the monochromated Tecnai TEM, with the results shown in Fig. 25. The area from Fig. 24A is revisited in Fig. 25A, and, once the energy scale change is noted, the structure of the edges is largely the same. In the vacancy rich region, the L<sub>2</sub> and L<sub>3</sub> peaks are suppressed, and the onset of the edge slopes more gently, as before. The chief difference between Fig. 24A and Fig. 25A is the loss of the large energy shift observed on the JEOL TEM. If there is any shift from the bulk in Fig.

25A, it is slightly to the left of the bulk sample. This is borne out again in Fig. 25B, where a series of spectra are presented from a line scan starting at the center of the irradiation (bottom spectrum) and moving out to the bulk (top spectrum). For clarity, the spectra have been linearly displaced in the vertical direction. Outside of the center of irradiation, the  $L_2$  and  $L_3$  peaks appear quickly, and grow more pronounced as the bulk is approached. A blip can be seen where spectrum vi. unexpectedly shifts to the left. It might be easy to dismiss this as beam instability, but the initial peak is also slightly augmented compared to the linear progression of ii. – vi., and its shape is slightly different. This will be revisited later in comparison with the theoretical results.

Simulations were performed to determine the EELS spectra predicted to arise from single vacancies and single self-interstitials, as well as point defect complexes for the purpose of comparison with the experimental EELS spectra. Seven supercell structures were relaxed to their lowest energy configuration, of which six are shown in Figure 26: A) tetrahedral silicon interstitial on a  $[\frac{1}{2} \frac{1}{2} \frac{1}{2}]$  type position, B) silicon split interstitial configuration, C) silicon monovacancy, a divacancy (not shown), D) trivacancy, E) tri-interstitial in a penta-ring formation and F) tri-interstitial in a tetrahedron. The densities of states of excited atoms were calculated for comparison with the EELS data using the  $Z+1$  approximation to replace silicon atoms near the defect with phosphorus atoms. The raw data had energy intervals of 0.09 eV, but the data has been convolved to look like the results from a spectrometer with 0.1-0.3 eV energy resolution. The results for the first few nearest neighbors for singular point defects can be found in Figure 27. For the tetrahedral silicon interstitial, the most significant change in the density of states (DOS) compared to the perfect lattice is the large extra state that arises around 1.2 eV from the onset of the conduction band,

see Fig. 27A. It appears for the four first nearest neighbors and six second nearest neighbors, although it is absent for the interstitial itself. The DOS of the third nearest neighbors were identical to that of the perfect lattice, which more or less defines the boundary of the electron energy loss radius of disturbance of the defect. The calculated  $Z+1$  DOS for a split interstitial configuration was indistinguishable from the calculated bulk EELS signal and is not shown here. The DOS of excited atoms near a vacancy is found in Fig. 27B. Here, the onset of the conduction band for the first nearest neighbor matches the perfect lattice well, but the second nearest neighbor has two large states near the bottom of the conduction band, causing a type of shoulder to form when averaged together. The shape of the near edge structure coming from the first nearest neighbor to the vacancy is quite different from the bulk, as well as being severely depressed. The second nearest neighbor signal shares its shape with the 1<sup>st</sup> NN, but the depression is gone and, in magnitude, it resembles closely the bulk curve. The 2<sup>nd</sup> NN also has two sizeable states in the bandgap near the bottom of the conduction band, which do not disappear even when averaged. By the 3<sup>rd</sup> NN, the signal was identical to the bulk. A spectrum formed from the weighted averages of the nearest neighbor components is given in Fig. 27C, and it has significant differences from perfect silicon, but this is not yet comparable to a real ELNES signal. In order to properly approximate experimental conditions from a real TEM measurement, some signal from the defect-free volume that the beam traverses must be averaged in, as has been done in Fig. 27D. A fair estimate of a not-impossibly-thin, not-too-thick region would be 4 nm thickness, or the height of eight unit cells, so Fig 27D represents an average of a total of 64 atoms, most of which are unperturbed. Here, the differences in the spectra have diminished considerably, although there is still depression in the first peak, as well as a small tail due to the band gap

states. For the interstitial, the biggest feature is a considerable augmentation just below the first peak. It seems, then, that to be able to identify individual vacancies and interstitials, based on their EELS spectra and in a spectrometer with 0.1 eV resolution, the region would have to be quite thin (2 nm or less). Samples with this thickness have been reported, so this is an attainable goal. On the other hand, a signal from vacancies and interstitials could be resolved in a thicker sample if the density of defects were in the 5-10 at. % range, for example in a heavily self-implanted silicon sample. In comparing the experimental results with the theoretical predictions for single point defects, there are interesting similarities. For the vacancy case, the qualitative features of the experimental data are found in the computational result: there is a reduction in the intensity of the first peak. For the interstitial case, the enhancement in the vicinity of the first peak is consistent with the experimental data.

In this experiment, the electron irradiation as well as the acquisition of energy-loss spectra were performed at room temperature, and there is strong evidence[5] that vacancies and interstitials diffuse readily at this temperature, forming complexes with themselves and other species. The observed signal then must be derived from clusters of point defects, whose simulated results will be presented next. The calculated spectra for divacancies, trivacancies and two arrangements of tri-interstitials can be found in Figs. 28 and 29. Upon a general comparison with the experimental data, a few differences stand out. Firstly, the Si  $L_2$  and  $L_3$  peaks are split in the simulated spectra. Secondly, the Si  $L_2$  peak in the experimental spectra is much larger than the  $L_3$  peak; they are roughly the same height in the theoretical plots. The results for the divacancy are similar to that of the monovacancy. It is clear from Fig. 28D that, at 0.3 eV resolution, neither the monovacancy nor the divacancy defect will be

discernible based on the *shape* of its ELNES; the energy shift may yet be of interest, however. The trivacancy in Fig. 28 really starts to show a larger magnitude of difference from the bulk, and resembles fairly well the experimental spectra acquired from the dark region of the irradiated N-FZ Si. Three key similarities should be noted: 1) The depression of the first peaks is represented nicely, 2) The more gentle sloping of the edge onset is present, and 3) the leveling of the dip at 5 eV after the edge onset is replicated.

The di-interstitial was not considered, but two stable configurations of the tri-interstitial were considered, one in a tetrahedral configuration ( $I_3$ -A), and one in an arc shape ( $I_3$ -B), see Figs. 25E and 25F. The simulated spectra from  $I_3$ -A have as their main feature a very large peak arising from the interstitials at the edge onset, echoing the peak found for the single interstitial. The magnitude of the spectral difference of  $I_3$ -A combined with the larger radius of the defect combine to make the averaged signal in Fig. 29D retain a significantly altered shape, mostly defined by its enhanced initial shoulder and the decrease in the dip at 11 eV. There is also an energy shift reflected in the calculation resulting from the large initial peak. Its magnitude in the bulk-averaged case is 0.1 eV, but the value is clearly concentration dependent when comparing Figs. 29C and 29D. In the case of  $I_3$ -B, the differences are less pronounced, but the initial shoulder is smoothed out, and the dip in the bulk at 11 eV is filled in. The shape is still unique, and can be easily differentiated from  $I_3$ -A. It may be worth noting that, while the  $I_3$ -A structure results in a signature similar to the tetrahedral interstitial, the  $I_3$ -B structure more closely resembles the split interstitial, perhaps because of similarities in the local bonding of nearby atoms.

The energy shifts observed in the experimental energy-loss spectra were somewhat varied, and not entirely consistent with the theoretical predictions. A large energy shift,

consistently observed in the JEOL in many spectra, and of which an example is found in Fig. 23A, is absent from the same measurements in Fig. 25A. A similarly consistent energy shift in Fig. 2b goes in the opposite direction in Fig. 3b-iv. The key to this inconsistency lies in a proper understanding of edge energy shifts and the experimental conditions. Energy shifts in the onset of a spectral edge can be caused by one of two factors: either a change in the electronic band gap can move the conduction band up or down, or the energy level of core electrons can shift up or down due to local charge gradients. The *ab initio* simulations give a good reflection of the edge shape and show that, in general, the band gap size is constant. One notable exception is I3-A, where a large peak effectively shifts the conduction band onset by 0.1 eV. In terms of core level shifts, however, simulations using pseudopotentials to describe the inner electrons do not allow the alteration of core electron states, and the simulations presented here cannot be expected to properly reproduce all of the experimental energy shifts. Energy shifts of the core electrons are mostly caused by excess or deficient local charge. Defects and their complexes usually can have two to four different charge states, depending on the Fermi level. During irradiation of a thin foil, very few beam electrons are absorbed into the sample, but many secondary electrons are caused to leave the sample. This will cause a deficiency in electrons that eventually will be compensated by the electrical grounding of the sample. The irradiated region is still likely to have a slight positive charge during irradiation, and this fact would suggest that point defects and their complexes will also tend to have an effective positive charge. The nearby silicon atoms will have the energies of their core electrons slightly lowered by the positive charge of the nearby defect, and this will result in an overall increase of the energy difference between core levels and the conduction band, causing the Si L-edge onset to shift up, as is observed in the spectra

from the JEOL TEM, taken immediately after irradiation. The Tecnai TEM measurements were done much later, however, and the experimental results suggest that the defect charge states have changed in the intervening days. It is unlikely, however, that it was a shift only of electrons that makes the difference, since electrons move quickly and should reach equilibrium in less than a second. Instead, it is likely that the agglomerated point defects continue changing their configurations over the next few days, possibly even emitting or accepting charged point defects (*e.g.*  $V^+$  or  $\Gamma$ ). For the vacancy-rich region in Fig. 25A, there is a 0.3 eV shift in the edge onset, indicating that the equilibrium charge state of the defect has caused the core electrons to shift to higher energies. The same is true of what is believed to be a signal arising from an interstitial complex in Fig. 25B-iv, but this shift is consistent in direction with the simulation results in Figs. 29C and 29D, indicating that the overall shift may be due to a combination of band gap and core level shifts.

Independent of the particular details of these comparisons is the fact that the EELS signal observed in the irradiated sample is point defect related. Since our EELS scans turned up no signals from other elements, and the purity of the zone-refined silicon is well documented, there is little room for other explanations. Another very useful result of this data is the resolution of a question mentioned earlier: whether the contrast differences in the Z contrast images are due to thickness variations or bulk point defect concentrations. The differences in the EELS spectra guarantee that the difference in Z contrast is not just a thickness difference. If silicon atoms were traveling only to available lattice sites on the surface, then there would be no reason for differences in the EELS spectra, which reflect variations in the bonding of silicon. In contrast, distinct and significant differences are

observed both in the bonding characteristics of the vacancy-rich region and in the interstitial-rich region, so lattice defects are clearly playing a role.

Although the EELS detection of individual point defects was not possible within the scope of this experiment, the possibility still merits a moment's discussion. Firstly, although the full width at half maximum (FWHM) of the Tecnai beam was measured to be 0.2 eV, it is clear that the EELS results do not reflect this level of resolution. This was due to the slight instability of the zero-loss peak caused by temporarily unavoidable factors of the local environment. The effective performance of the instrument was probably ~0.4 eV resolution, while the simulation results reported here suggest that an energy resolution of 0.1-0.2 eV is necessary to discern the subtle differences introduced by vacancies and interstitials. A second issue is the question of defect mobility. This experiment was conducted without temperature control, but it has already been noted that point defects have been observed to diffuse at very low temperatures, depending on the sample doping. Irradiation by a 200kV beam has been demonstrated to induce Frenkel pair creation at low temperatures without the presence of nitrogen.<sup>31</sup> Therefore what is needed to attempt this measurement is a 200 kV monochromated TEM with a sample holder capable of cooling to liquid helium temperatures and an energy resolution less than 0.2 eV. A short irradiation time should be used to create Frenkel pairs in the thinnest region of the sample and to move the interstitials outside of the beam via elastic collisions while avoiding sample heating. A methodical search in EELS mode would then have to use short acquisition times to avoid the diffusion of the point defects. While this experiment is quite demanding, a positive result would certainly be worth the effort.

## 6.4 Conclusion

We have found experimental evidence that the complexes of silicon self-interstitials and the complexes of vacancies, as created by electron irradiation, provide a chemical signature in the shape of their respective near-edge energy loss spectra. Experimental spectra have been presented that appear to match the theoretically predicted shapes of the energy-loss near-edge profile for  $V_3$  and a tetrahedral arrangement of silicon interstitials. The experimental conditions for observing single point defects could not be attained, but the theoretically predicted spectra indicate the possibility of experimentally detecting single vacancies and interstitials. The qualitative features of vacancy and interstitial related ELNES have been shown to be consistent from single defects to complexes of three point defects.

## 7 The Athermal Manipulation of Dopants to Produce Device Structures on the Nanoscale

To be submitted to Science as “A Novel Method for the Creation of Bipolar Junction Transistors from 15nm to 1 $\mu$ m in size in Silicon at Room Temperature” by N. Stoddard, M. Nikiforov, D. Bonnell, G. Duscher and G. Rozgonyi, August 2004.

### 7.1 Introduction

One of the main trends required by the ITRS roadmap for integrated circuits is the shrinking of dimension size for most of the components of a CMOS device. Currently, this is envisioned as refinement of the lithography process, with plans to move into ultraviolet light sources in order to decrease the minimum size dictated by the optical resolution limit. Effort is also being put into e-beam lithography as an alternative serial process, but many challenges remain, including the related thermal budgeting.<sup>49,50</sup>

The scattering angle dependent expression for energy transfer in an elastic collision was given above. The maximum possible transferred energy,  $T_{max}$ , corresponds to  $\theta = 180^\circ$ , and is summarized in Table 3 for 200kV electrons.<sup>30</sup> The comparison point for these energies is the silicon displacement energy, i.e. the minimum energy to create a Frenkel pair. Reports for the actual value vary, but experimental values range from 11-20 eV<sup>30</sup> while theoretical estimates go as low as 10 eV, depending on crystallographic orientation.<sup>26</sup> Based on TEM observation of e-beam irradiation, there is evidence that the displacement energy is temperature dependent. Irradiation with 200 keV electrons at a temperature of 15 K produced visible damage, while extended irradiation at room temperature, but with otherwise similar conditions produced no changes in the sample.<sup>31</sup> This second observation would place the RT silicon displacement energy somewhere between 18 and 20 eV. This narrow

range will be taken as the working value for energy estimates in this paper. With this value in mind, one can revisit the values from Table 3. P-type boron atoms may receive up to 48.5 eV during an elastic collision with an electron, while n-type antimony can only receive 4.3 eV. Even with the possibly large errors in assuming that the displacement energies for substitutional boron and antimony are similar to that of silicon, it still seems quite likely that boron will be rather easily displaced during electron irradiation while antimony will not be knocked off of its lattice site. Once displacement of the boron occurs, boron is known to diffuse quite readily via interstitial and interstitialcy mechanisms, with an activation energy of 3.5-3.8 eV and a migration barrier of 0.4-0.7 eV.<sup>51,52</sup> Various techniques are known to enhance the diffusivity of boron, including transient enhanced diffusion and low energy ion bombardment<sup>53,54</sup>. In this case, boron will diffuse through the crystal without further damage because of subsequent electron collisions, each of which may impel a boron atom to make several atomic jumps. In this way, it is expected that 200 keV electron irradiation will cause boron deactivation and diffusion throughout much of the excitation volume. In this paper, this effect will be demonstrated with the useful consequence that p-n-p junctions can be formed in co-doped silicon.

## 7.2 Materials and Methods

Samples of p-type silicon were co-implanted, first with 35kV B<sup>+</sup> atoms at doses of  $(5-30) \times 10^{15}$  atoms/cm<sup>2</sup>, and subsequently with 300kV Sb<sup>++</sup> atoms at total implant doses of  $(3.5-20) \times 10^{15}$  atoms/cm<sup>2</sup>. A simulation of co-implanted boron and antimony, both at a dose of  $5 \times 10^{15}$  atoms/cm<sup>2</sup>, resulted in the doping profile shown in Fig. 30. This pair of dopants was chosen to have the greatest selectivity in their response to e-beam irradiation, as was

described above. The depth profile results in a p-n-p vertical structure with the first junction at 200 nm from the surface and the second around 1600 nm deep. Repair of the amorphized depth was achieved either by solid phase epitaxy (SPE) growth at 720°C or by laser annealing with a Nd:YAG laser operating at 266 nm, with an energy of 180 mJ and emitting an 8 ns pulse every 0.1 s. Cross-sectional TEM samples were prepared by the micro-cleavage method for analysis using a 200 kV JEOL 2010F field emission TEM both for conventional TEM imaging as well as bright field and Z contrast imaging modes of scanning TEM (STEM) with 1.8 nm minimum spot size. Recrystallization was assured by TEM imaging. The SPE regrowth failed below 720 °C, and, even when successful, tended to cause dopant clustering at high implant doses, as shown in Fig. 31B. Laser annealing successfully recrystallized the sample without clustering, but did result in some stacking fault nucleation, see the Z contrast micrograph in Fig. 31A. Thicker samples were also prepared in a plan-view geometry by back-side polishing to 100 μm thick. Irradiation was performed either in the JEOL instrument or in a Topcon 002B TEM with LaB<sub>6</sub> thermionic emission filament and 400 nm minimum spot size, and exposure times varied from 10 s to 20 min. EELS was attempted to characterize doping profiles in the cross-sectional sample, but the concentration was below the detection limit. Atomic force microscopy (AFM) was then performed using a Digital Instruments Nanoscope to examine the topography and surface potential of the sample. The surface potential signal represents a combination of surface charge and electronic potential, and it is expected to have a value somewhat compensated compared to that of the bulk due to surface charging. To perform C/V and I/V measurements, platinum contacts were deposited on the laser-annealed silicon using a focused ion beam (FIB). First the native oxide was removed by FIB milling of 1 nm and a ramp was made from the near-

edge oxide-removed area to the interior oxide area so that the platinum wire would be continuous. Irradiation was then performed in the TEM near the deposited metal contacts. Now, using the AFM, the circuit was completed by soldering an external wire to the FIB contacts, connecting it to the AFM and using the AFM probe to contact the n-type region. With the AFM in non-scanning, non-contact mode, the electrical characteristics of the diode could be measured. Care was taken to ensure that the samples were not cleaned in an oxygen plasma prior to irradiation in order to preserve the integrity of the metal contacts, but methanol was sometimes used to remove organic contaminants.

### 7.3 Results

Irradiation of doped samples in both plan-view and cross-sectional configurations had almost imperceptible effects as observed in the TEM. No strain contrast accompanied the irradiation in conventional TEM, and no Z contrast change was observed in STEM mode. When the samples were taken to the atomic force microscope, however, the result was clear. In Figs. 32 and 33, a surface potential difference of 100-300 mV was observed at the irradiated positions in the bulk sample compared to the background, while no corresponding topographic features are present. The sizes of the n-type spots in Figs. 32 and 33 correspond nicely to the 400 nm diameter of the TEM beam used to create them. In Fig. 32, movement of the sample during irradiation caused an elongation of the irradiated region, but the width matches perfectly. In Fig. 33, evidence of the beam being slowly dragged along the surface can be seen on the left side with the same characteristic beam width. In both of these cases, irradiation was performed using a larger beam for ease of observation in the AFM, but the physics remains the same using beams converged from 1  $\mu\text{m}$  to 5 nm.

## 7.4 Discussion

For the bright surface potential spots that lack corresponding topography, the surface potential in Figs. 32 and 33 is attributed to a surface-compensated bulk potential difference caused by band-bending local to a p-n junction. The true value of the bulk potential difference is unattainable using this type of measurement, but estimating the surface compensation at 0.2 V places the difference in the ~500 mV range expected for a p-type to n-type transition. Figure 34 illustrates the circuit that will be used to electrically characterize the device properties to verify the p/n diode behavior. One key question for the real-world feasibility of this technique is the exposure time needed to deactivate a sufficient proportion of the boron atoms. The peak boron concentration is roughly five times the antimony concentration at that depth, but if the laser annealing levels out the profiles, the average boron concentration is about twice the antimony concentration. In order to have a p/n junction, at least one half of the boron should be removed; three fourths removal would make a good p+/n+ junction. With a beam size of 400 nm and a beam current of ~10  $\mu$ A, there are a total of  $1.24 \times 10^6$  electrons passing through every unit cell area ( $0.29 \text{ nm}^2$ ) per second. Assuming that the boron displacement energy is similar to that of silicon, an energy transfer of 20 eV (conservatively) is required. Using the same reasoning as in Section 1.3, the probability for each 200 kV electron to transfer 20 eV to boron is  $\sim 2 \times 10^{-5}$ , assuming randomized incidence. After one second of beam exposure, the probability that each boron atom has been given at least the required 20 eV is  $\sim 0.998$ . Even if the effective displacement energy is 40 eV, the probability of deactivation is still 0.54 within the first second of beam exposure. Once the atom is displaced, recombination with other vacancies or diffusion by

kicking out silicon can cause boron reactivation and a lower efficiency, so it is reasonable to estimate that several seconds would be necessary for a 400 nm beam to create a quality n-type region. In a field emission microscope, the current is lower ( $\sim 1 \mu\text{A}$ ), but the spot size can go down to the point where the p/n junction quality is limited by the concentration of dopants, even at high concentrations. At the performance limit of the material and tightest convergence of the beam, successful deactivation of the boron would likely require only a fraction of a second.

## 7.5 Conclusion

There are several promising aspects to this technique. First, the inherent limitations of photolithography are sidestepped, circumventing the need to use ever-smaller light wavelengths. Secondly, some of the challenges involved in traditional e-beam lithography are also avoided. For example, this technique employs direct patterning of doped regions by interaction with the e-beam, instead of using the e-beam to pattern a resist material, in which case such issues as aspect ratios of the etched resist and ion implantation challenges arise. Ideally, this new process would be integrated with photolithography to save time and money; photolithography would stage the larger device features and then e-beam lithography would trace the finest n-type features. This technique relies on efficient de-activation of boron in a co-doped sample, and the selectivity is only based on mass difference between boron, the n-type material and the host material. While antimony was used here for the greatest mass contrast, other n-type dopants including arsenic and phosphorus should also work, as should other host materials like SiGe or GaAs. Furthermore, the extent of boron deactivation is time dependent, so the boron concentration promises to be controllable in between the ‘all or

nothing' techniques used here. In order to have the sharpest concentration profiles, however, the e-beam deactivation step should occur after all significant thermal steps have occurred. Other applications of e-beam assisted diffusion present themselves as well. For example, 200kV electron beam exposure might be used to 'clean' near-surface regions of a silicon device by removing all light element impurities (H, O, C, N, F), and not just boron. As is evident even from this relatively simple device fabrication, however, smaller doping regions will require smaller contacts and the development of a number of technologies not yet in existence. Here, metal contacts were deposited using a focused ion beam method, a technique that has not yet been integrated into IC fabrication, but e-beam lithography for metal patterning promises a better long-term result. In any case, it has been demonstrated that quantum size p- and n- type regions can be created in traditional silicon substrate technology.

## 8 General Conclusion

In the field of materials science, the study of solid state materials can be generally divided into categories based on crystal structure: from amorphous to nanocrystalline to polycrystalline to single crystal. For the fabrication of optical and electronic devices, the perfection of crystalline materials is of central importance. Thermodynamic limits prevent the existence of truly perfect crystals, so much of the aim of materials engineering is to better control atomic-level defects and the extended defects that evolve from them. The transmission electron microscope is in many ways unrivaled in its ability to study materials and their defects at the atomic scale. There exist challenges in the preparation of suitable samples, and even in the course of this work it has been demonstrated that a TEM thin foil cannot be automatically assumed to exactly represent the bulk material it came from. Other limitations persist in the high voltage ( $> 1$  MeV) study of damage in silicon. For example, it is difficult to study damage *in situ* because the damage cannot be stopped while the beam is on the sample. Ideally, the occurrence of damage during irradiation would be separated from the analysis of the sample within the same instrument. Another difficulty is that, while the intended purpose is to learn about the thermal evolution of defects, damage is always introduced in the form of knock-on cascades that are decidedly non-equilibrium. Furthermore, the high density of vacancies and interstitials in close proximity to one another gives rise to a complex situation where recombination is perhaps the most dominant event. In an ideal situation, Frenkel pairs would be introduced one-at-a-time and then spatially separated so that interstitial defects could evolve separately from vacancy defects. Nevertheless, high voltage transmission electron microscopy has remained the primary tool for studying the evolution of extended defects from their atomic constituents.

The aggregate of work presented here points to the diverse applications of a new technique for the study of silicon. Firstly, the demonstration of room temperature point defect creation in silicon by a one-at-a-time process has given new insight into the behavior of silicon. The displacement energy for silicon is widely quoted to be between 11-20 eV, but there is a lot of room within this range. For instance, a material with a displacement energy of 11 eV would be easily damaged by a 200 kV electron beam, but a material with  $E_d = 20$  eV would not react at all. Silicon has the interesting behavior that broad beam irradiation by 200 keV electrons causes no lattice damage while converged beam exposure on thin foil samples readily creates holes, an effect that occurs for accelerating voltages down to 140 kV. It has been demonstrated here that the difference in the response is not a question of surface diffusion vs. bulk diffusion, as was widely believed, but instead that there is a continuum of responses, all based on bulk diffusion and depending only on the time between electron collisions. Because the individual Frenkel pair in pure silicon recombines so quickly, there is very little time for a second electron collision to further separate the pair, and only the highest fluencies of electrons will bring the probability of a second collision into a reasonable regime. It has also been shown that nitrogen brings a perturbing influence into the electron-silicon interaction by changing the dynamics of the knock-on process so that the Frenkel pair is not only easier to create, so that the energy barrier is 6.2eV as opposed to 11 eV, but also more stable and less likely to recombine. Through the repetition of the Frenkel pair creation process, small amounts of nitrogen (0.5 ppm) have been demonstrated to allow the e-beam induced spatial separation of vacancies and interstitials, the formation of point defect complexes and the evolution of voids, the nucleation, growth and coarsening of oxygen precipitates and the partial amorphization of silicon. The fact that all of these

phenomena occur at room temperature, instead of the normally high temperatures required for bulk diffusion, is quite useful for *in situ* TEM imaging and opens the unique possibilities of chemical analysis from EELS analysis. Furthermore, even though no irradiation process reproduces the conditions of thermal equilibrium, the creation of point defects one at a time comes much closer to a quasi-equilibrium dynamic than does irradiation that causes damage cascades.

The diffusion of nitrogen has been studied both experimentally, where low energy ion bombardment has been shown to cause nitrogen diffusion several microns into the bulk, as well as theoretically, where two diffusion paths for the nitrogen pair were discovered. One diffusion path has a lower migration barrier than any previously reported, while the other, higher energy path requires the movement of only one of the two atoms, as might occur after an electron collision with one atom of the pair. The use of *ab initio* simulations has also been used in combination with EELS analysis to demonstrate a new way to study point defect complexes in silicon. Finally, the difference in energy transferable from fast electrons to light vs. heavy atoms has been used to great advantage to selectively deactivate boron atoms in compensated material for the creation of creating p/n junctions. The athermal nature of the process together with the fact that the silicon lattice is not damaged combine to make this a very viable end-of-processing step that is capable of creating features of the highest resolution. Other applications that take advantage of this mass selectivity have been outlined and await further exploration.

In total, 200 kV electron irradiation has been demonstrated to share many of the advantages of high voltage microscopy, but it can go further by introducing Frenkel pairs and energy into the crystal in a manner much closer to a thermal environment. Useful

applications for both fundamental materials science and applied materials engineering have been developed that take advantage of the spatial resolution of the TEM as well as its wide range of analytical capabilities, yet have remained undiscovered despite the widespread use of the TEM. In a few cases, the door has already been opened for many further discoveries.

FIGURES

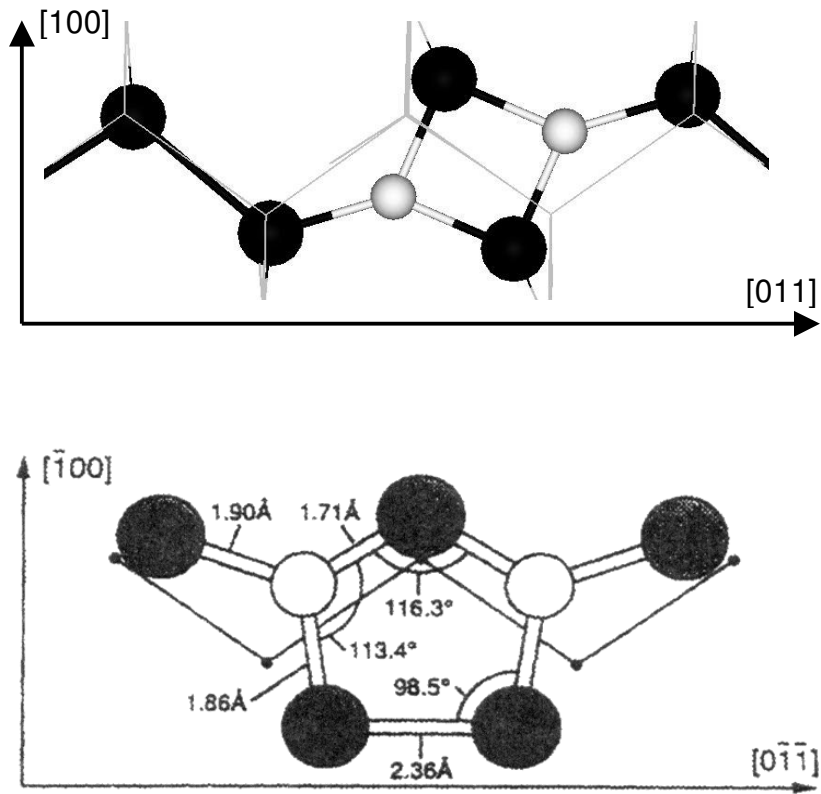


Figure 1 A) Antiparallel and B) Humble configurations for the N<sub>2</sub> pair. Nitrogen is in white, silicon in black. B) From R. Jones, S. Oberg et al.

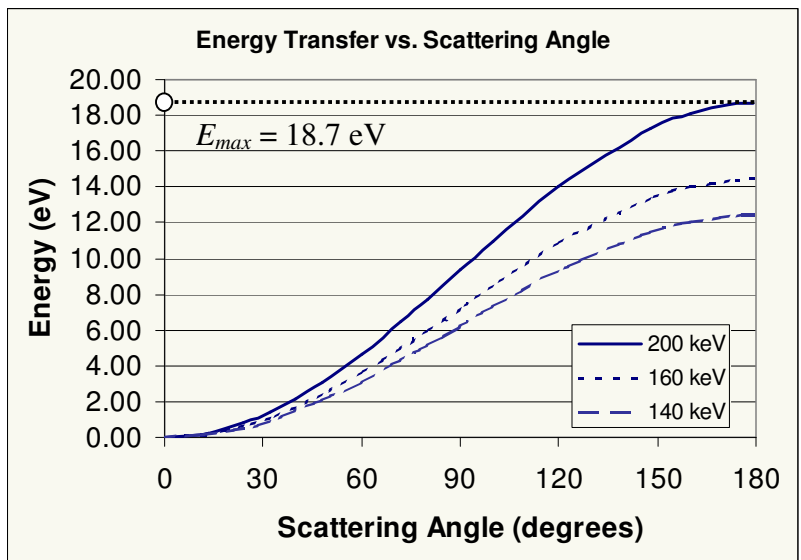


Figure 2: Energy imparted to silicon as a function of recoil angle for electrons of 140 kV, 160 kV and 200 kV.

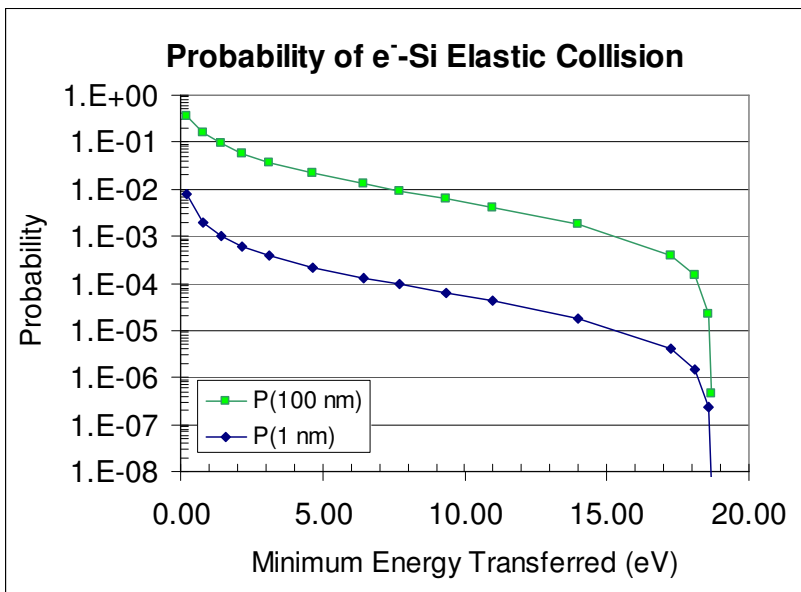


Figure 3: Probability for energy transfer by a 200 kV electron to a silicon atom as a function of transferred energy.

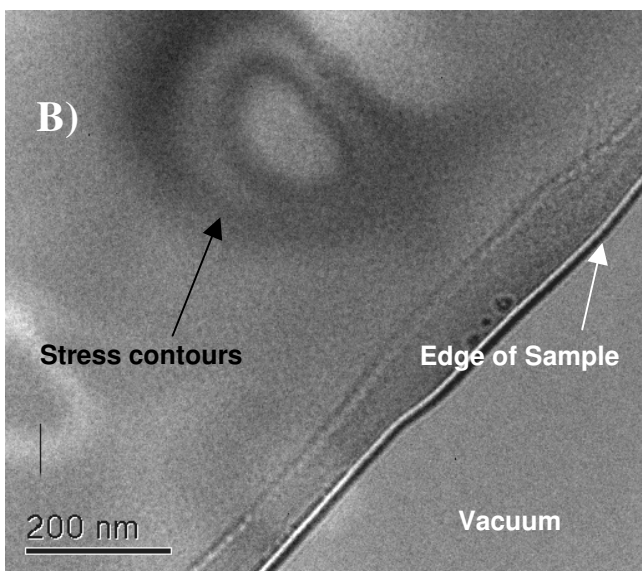
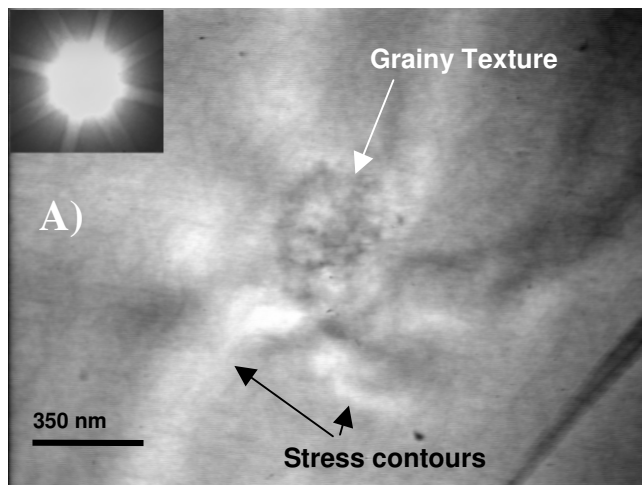


Figure 4: Conventional TEM showing the entire irradiated areas after 20 min. exposure to a 200 keV convergent beam: a grainy texture in the N-Cz sample A) is not present in the Wacker N-free Si sample B). The inset Kikuchi pattern verifies (100) zone axis alignment

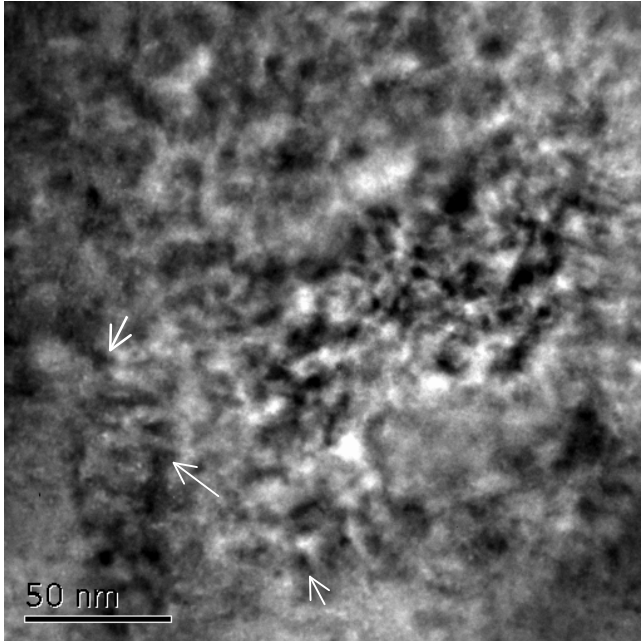


Figure 5: Close-up of Fig. 4A from the irradiated area of N-doped sample. Some faceted dark areas, indicated by arrows, suggest the presence octahedral voids.

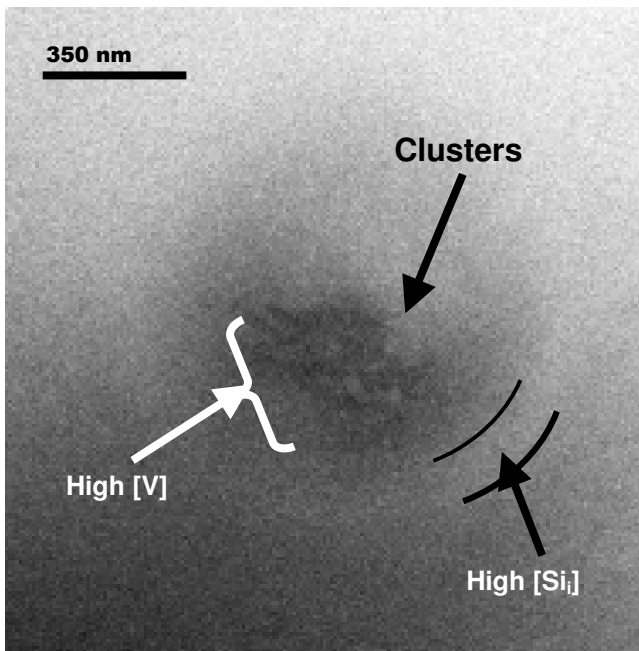


Figure 6: STEM Z-contrast image of N-CZ Si irradiated area, as in Fig. 4A. A central dark area is attributed to a large concentration of vacancies while the brighter ring surrounding it is attributed to excess self-interstitials. Some modulation of contrast exists in the dark region, suggesting clustering.

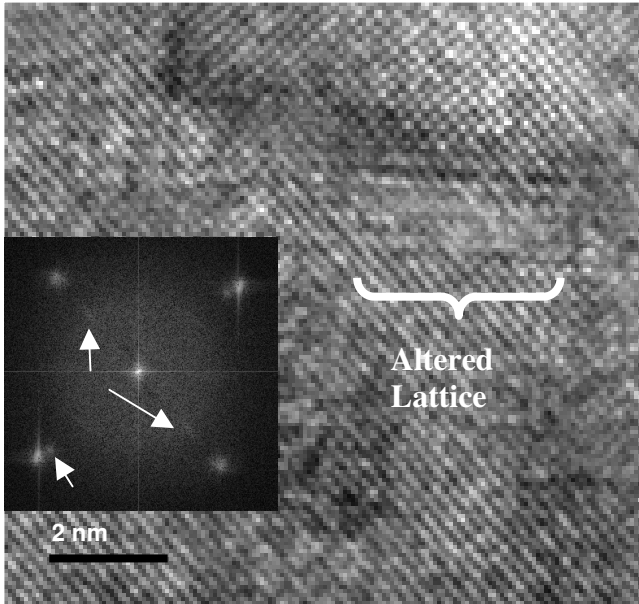


Figure 7: A HRTEM image of an irradiated area. The lattice has a different periodicity in the indicated area, and the four extra spots in the Fourier transform indicate the existence of a second phase.

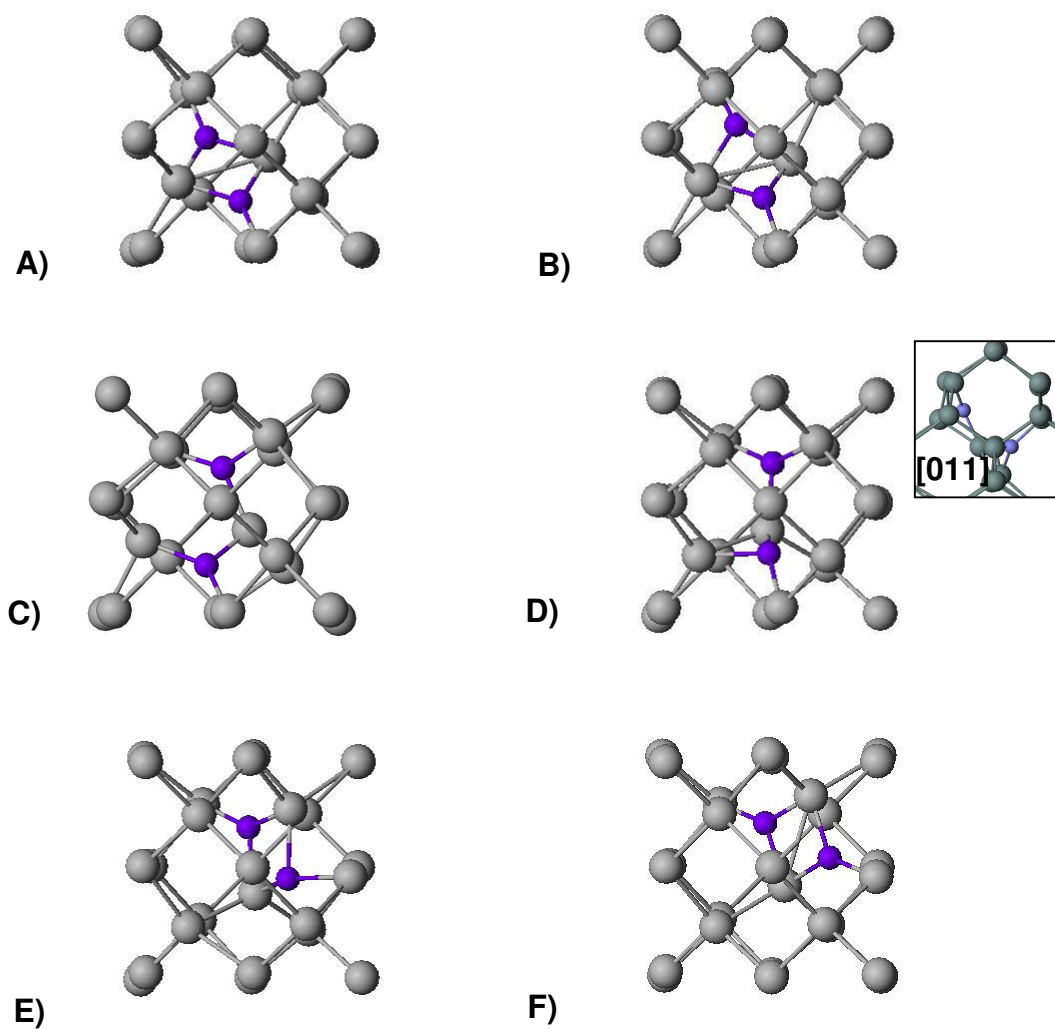


Figure 8: Low activation barrier diffusion series for a nitrogen pair (in purple) moving through the silicon lattice (gray). The first and last configurations are equivalent, and the energetics are provided in Fig. 10A.

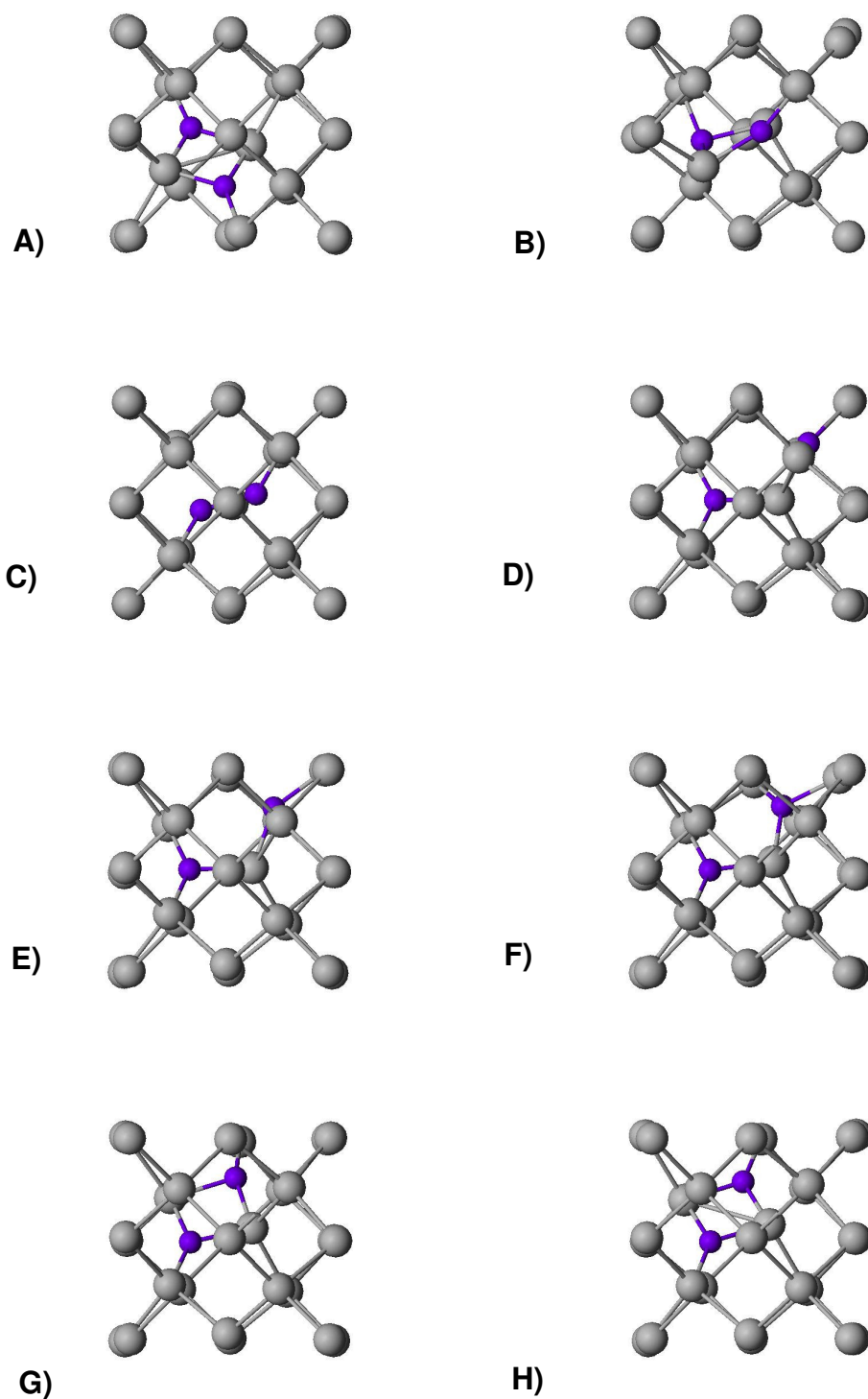


Figure 9: Higher activation barrier diffusion series for a nitrogen pair. The lower left nitrogen atom swings out and around while the upper right nitrogen atom mostly remains inactive. The corresponding energetics can be found in Fig. 10B.

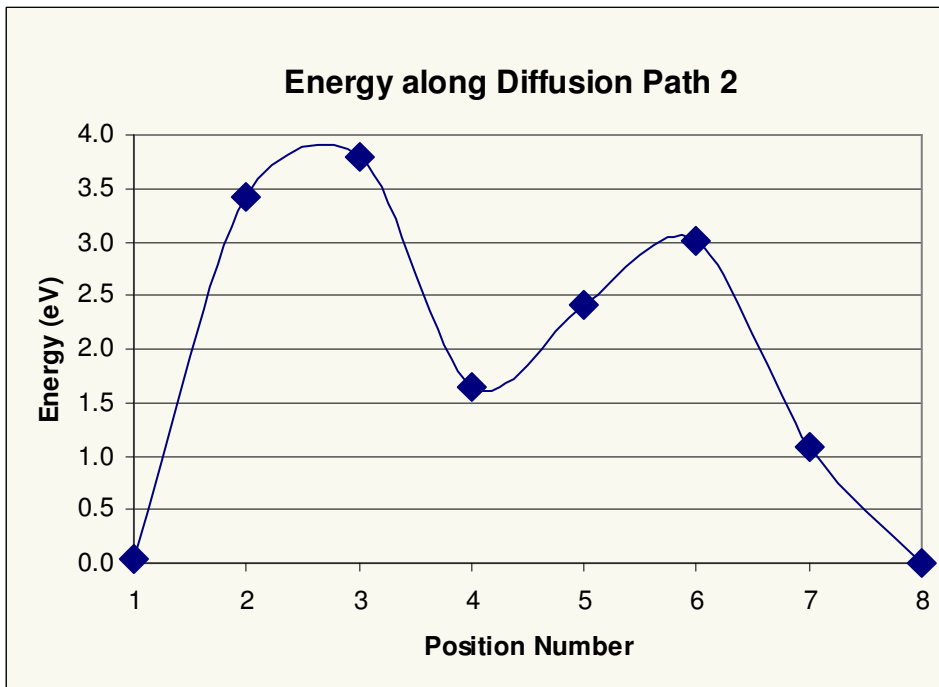
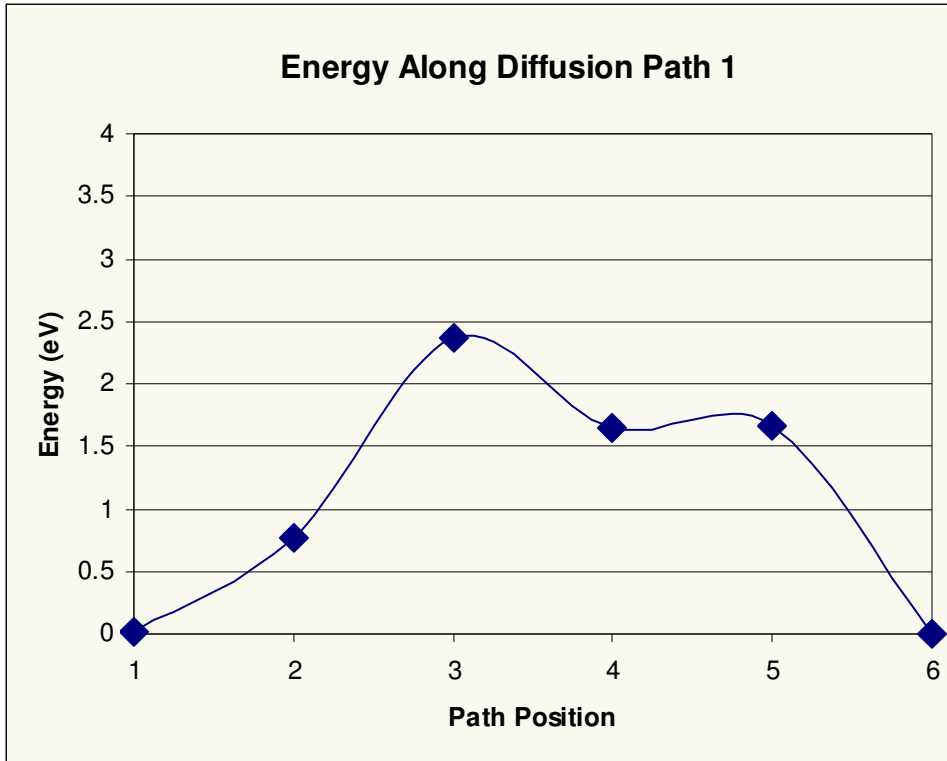


Figure 10: Energy profile for the two diffusion paths. The first has a 2.3eV energy barrier while the second has a 3.8eV barrier to a metastable state that has another 1.3eV activation energy to get back to the ground state.

Table 1: Bond lengths (in Å) for the nitrogen atoms through the stages of diffusion. If no fourth nearest neighbor distance is provided, then the next atom is more than 3.1Å away.

Path	Bond Length of N(1)				Bond Length of N(2)			
	1	2	3	4	1	2	3	4
Path 1								
1	1.73	1.74	1.78		1.73	1.75	1.76	
2	1.73	1.74	1.76		1.67	1.73	1.98	
3	1.72	1.73	1.74		1.44	1.72	2.30	2.59
4	1.76	1.77	1.82		1.72	1.78	1.80	
5	1.78	1.87	1.91	2.70	1.72	1.73	1.77	
6	1.66	1.72	2.16	2.56	1.67	1.73	2.31	2.37
Path 2								
1	1.72	1.79	1.81		1.72	1.73	1.76	
2	1.72	1.74	1.82		1.76	1.79	1.86	
3	1.56	1.72	1.74	2.71	1.56	1.84	1.95	1.96
4	1.71	1.76	1.78		1.73	1.77	1.80	
5	1.73	1.74	1.91		1.71	1.79	1.79	
6	1.74	1.79	1.84	2.67	1.73	1.76	1.79	
7	1.72	1.76	1.85		1.72	1.73	1.76	
8	1.66	1.72	2.16	2.56	1.67	1.73	2.31	2.37

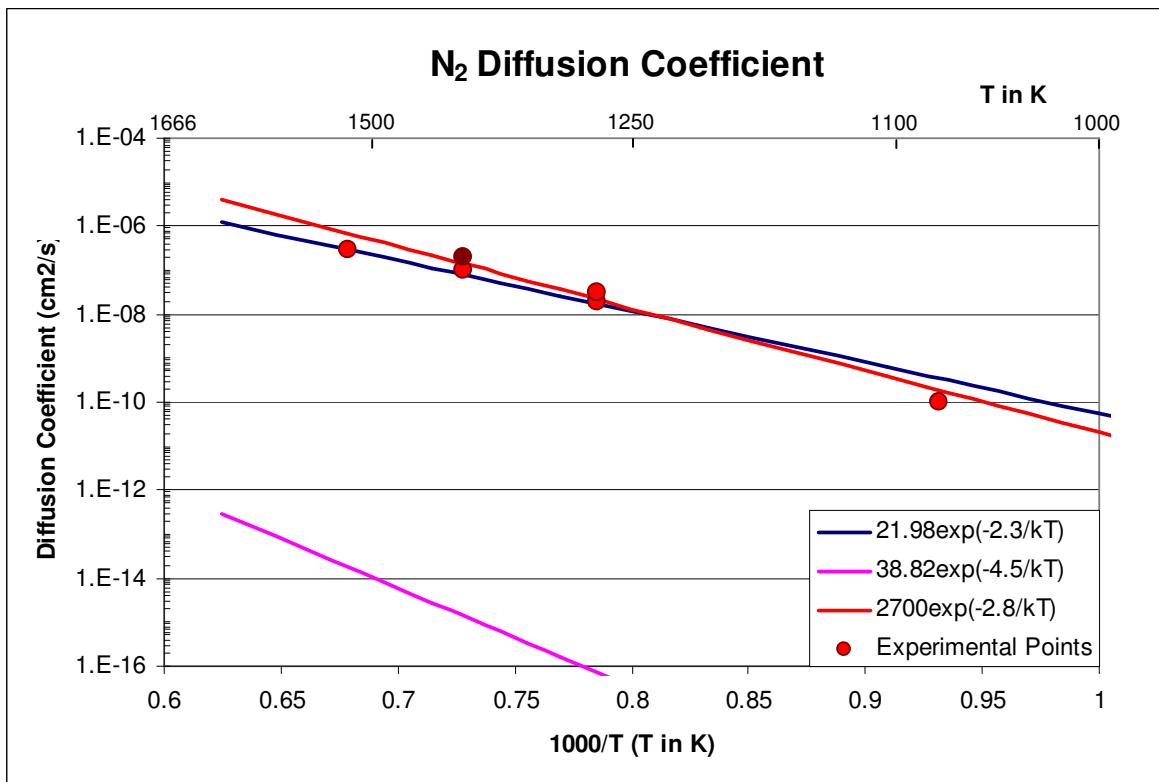


Figure 11: Arrhenius plot of the calculated diffusion coefficient for the N<sub>2</sub> pair in silicon compared to experimental data from [13].

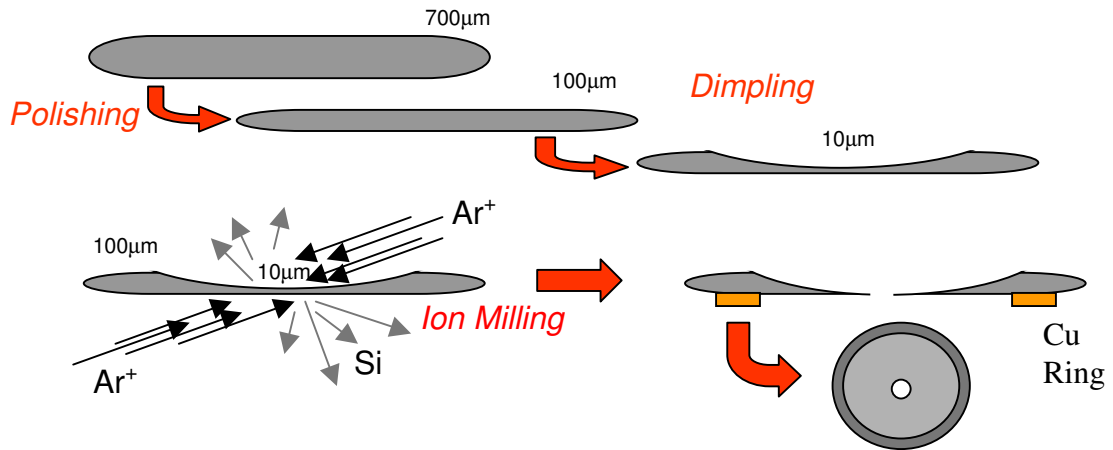


Figure 12: Series of surface treatments used to create TEM samples: polishing, dimpling and ion milling. Each of the processes is used elsewhere in semiconductor manufacturing.

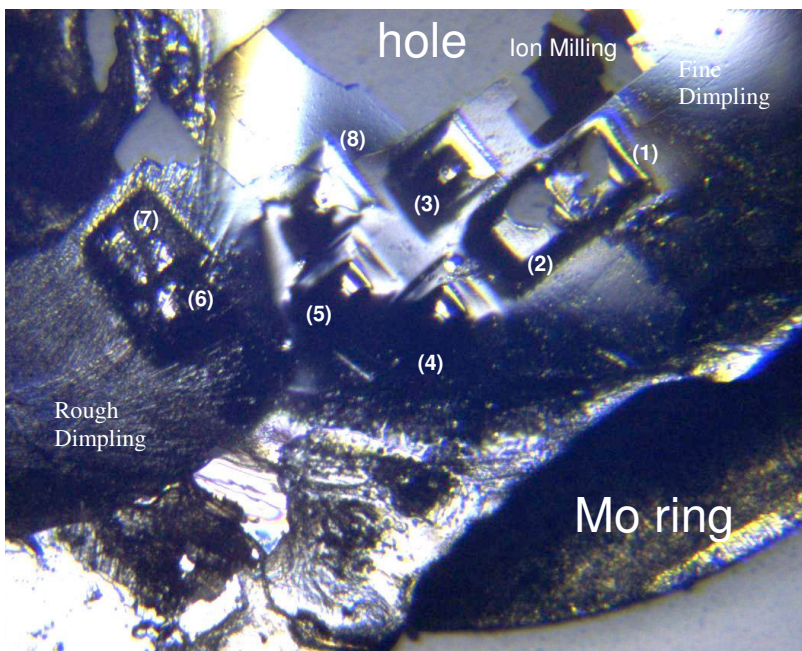


Figure 13: Layout of SIMS craters on Set A TEM foil. Process steps are labeled, as are craters (1) - (8).

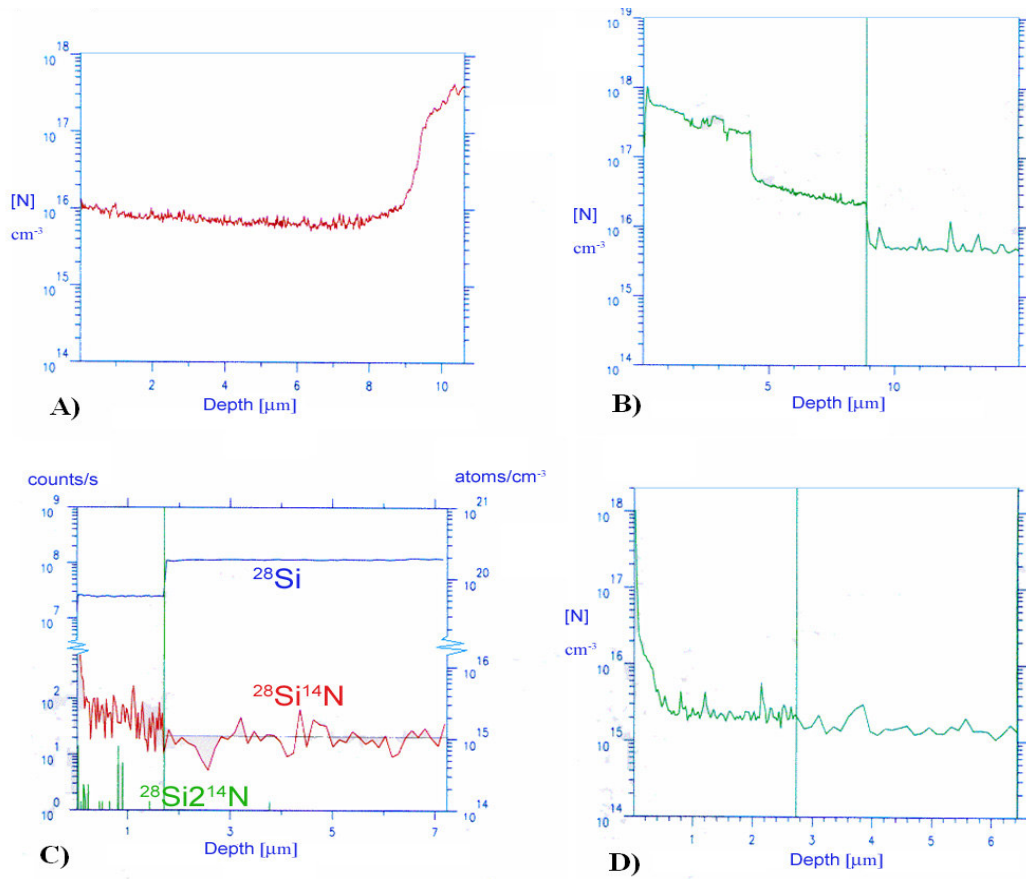


Figure 14: SIMS nitrogen depth profiles resulting from different processes on a TEM foil: A) Profile after ion milling; the large increase in sample is due to sample breakthrough. B) Rough dimple grinding. C) Profile for fine dimpling. D) An area far from the center of ion milling (near bulk). The vertical green lines indicate the depth at which the raster size was reduced.

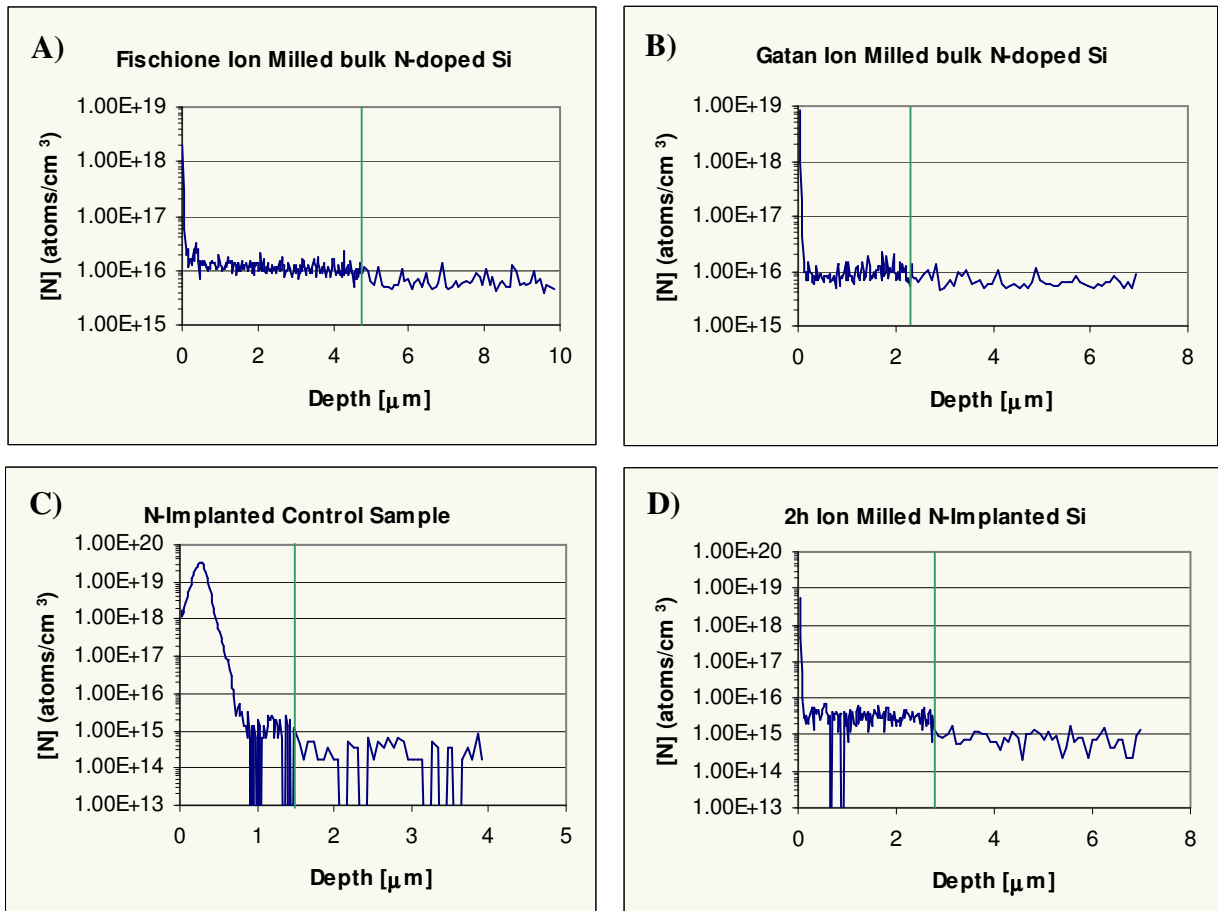


Figure 15: N depth profiles for bulk samples. A) and B) are nitrogen doped (Set A) and ion milled on different machines. C) and D) are implanted with nitrogen (Set B), one a control sample and the other after two hours of 50 °C ion milling.

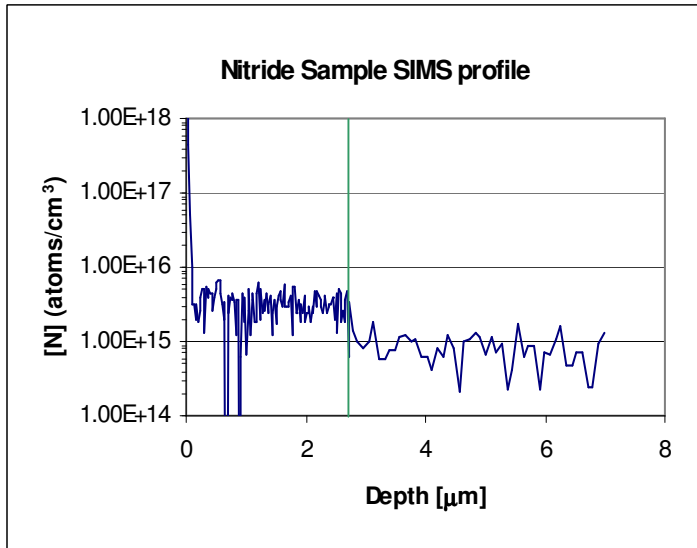


Figure 16: Nitrogen depth profile for nitride layer sample from Set B. The decrease in signal upon raster reduction (around 3 μm deep) indicates that part of the signal comes from redeposited material.

Table 2: SIMS results for samples from Set A

Preparation Step	[N] (cm <sup>-3</sup> )	Comment
Initial	1 E 15	From N ambient
Thinning: Syton/Ludox CMP	5 E 14	Well polished surface
Fine Grit Dimple Grinding	1 E 15	Back to original levels
Ion Milling	1 E 16	[N] decreases to 2E15 as distance to hole increases

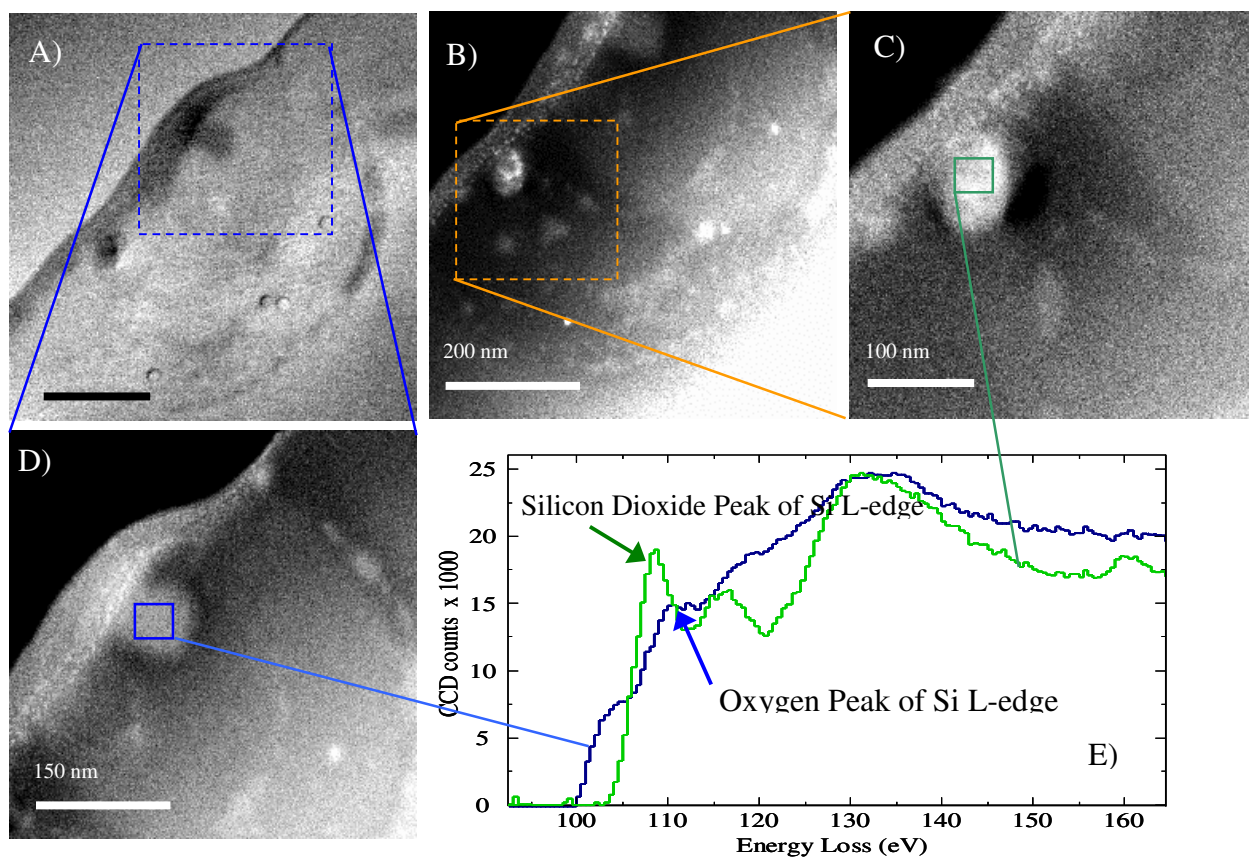


Figure 17: 200kV Scanning TEM images of an e-irradiated region of a N-Cz Si sample. A) is a bright field image while B), C), and D) are Z-Contrast images revealing bright clusters inside and peripheral rings surrounding the irradiated area. E) is an electron energy loss spectrum from two of the particles nucleated during irradiation. The particle in C) is identified as stoichiometric silicon dioxide by the peak at 106 eV in the Si L<sub>2,3</sub> edge. The particle in D) is mostly composed of silicon with interstitial oxygen.

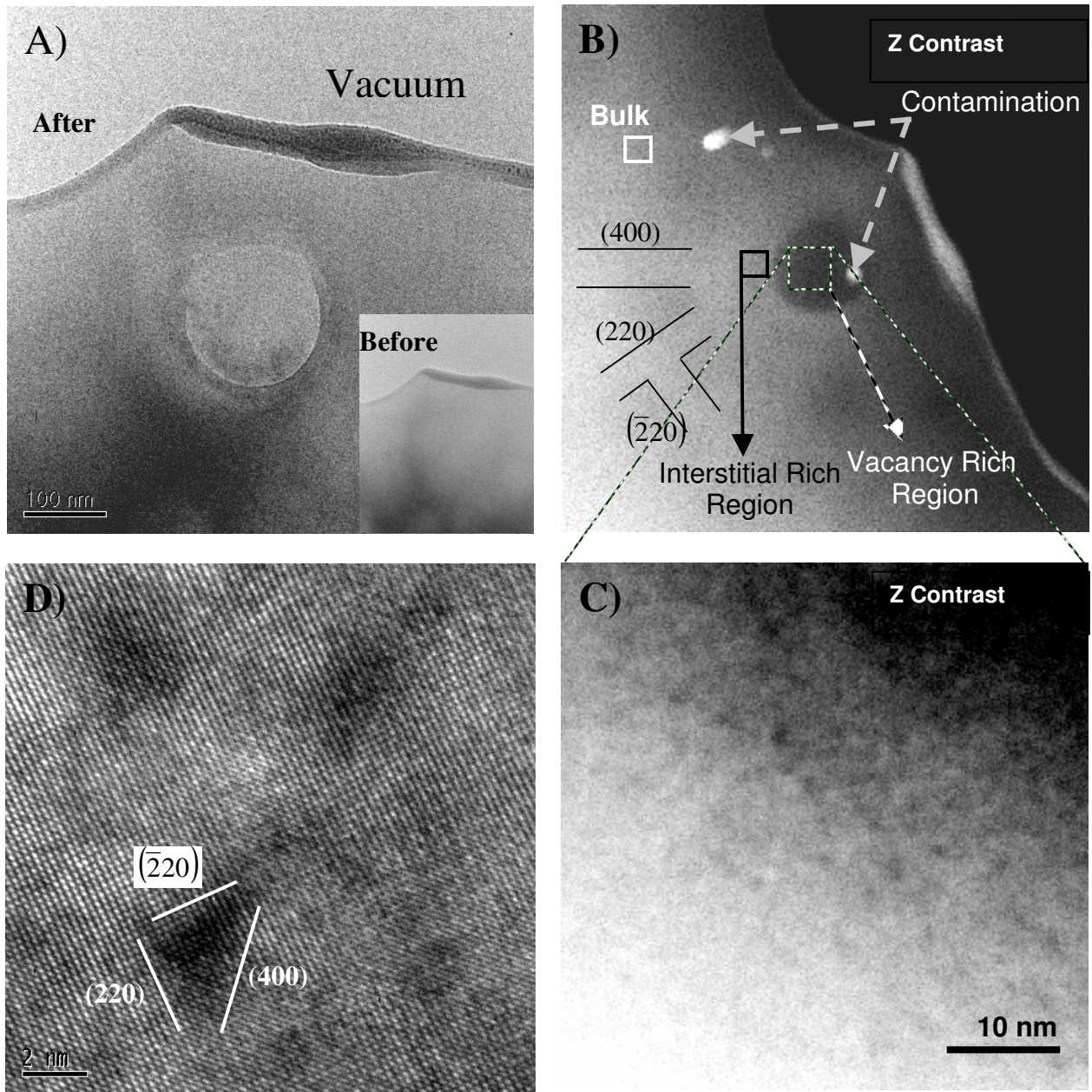


Figure 18: TEM images of a N-FZ Si sample after irradiation. A) is a conventional TEM image of N-FZ Si irradiated for 10 min. in a JEOL 2010F TEM. B) is the same region imaged in Z Contrast STEM mode: no bright speckles exist in the dark vacancy-rich region, but faint bright lines emanate from the center along crystallographic directions. C) is a higher magnification image of the vacancy-rich dark circle, revealing small voids, imaged as faceted dark pits. D) is a high-resolution conventional image of the area in C).

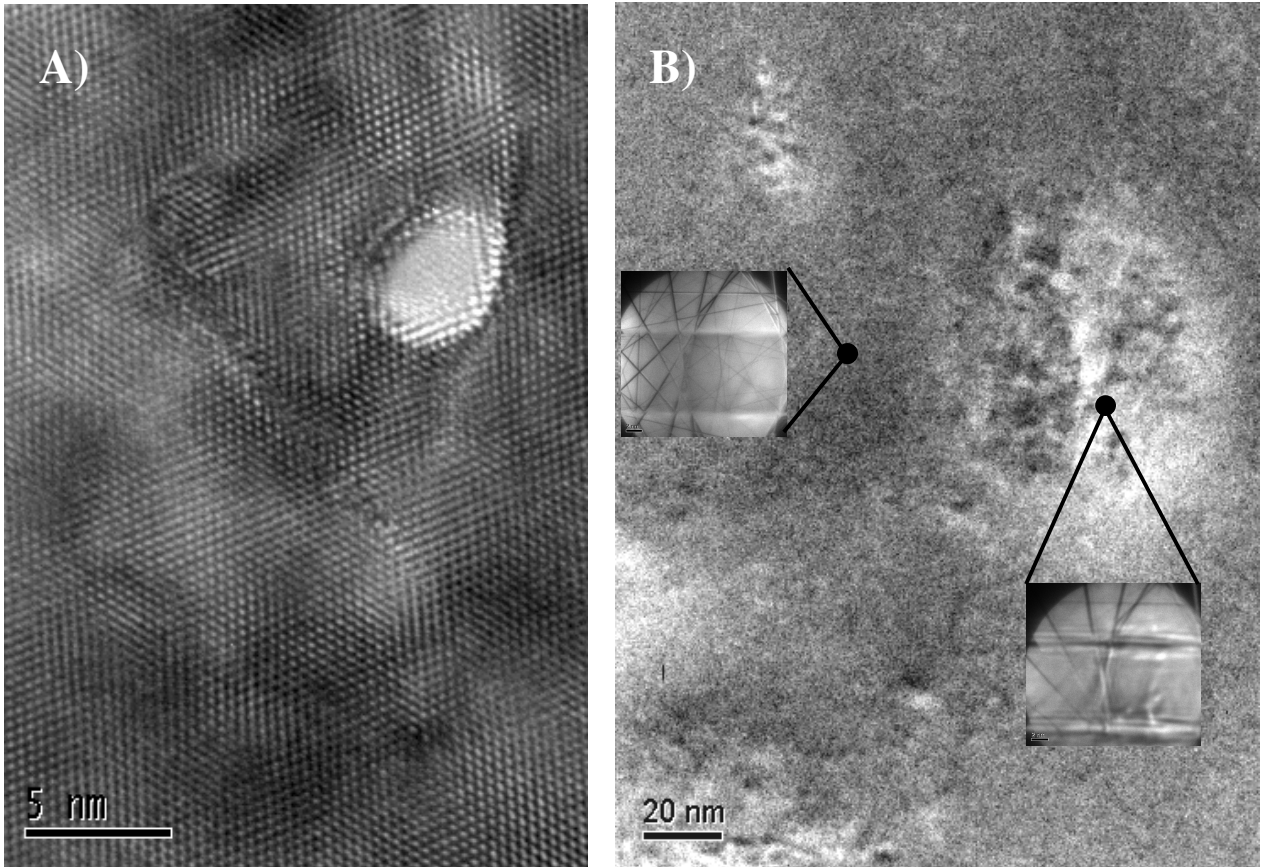


Figure 19: Tightly Converged Beam Irradiation: A) The interstitials ejected from the 3 nm irradiation area during hole formation diffuse into the bulk and coalesce to form a stacking fault, whose ends are indicated by the arrows. B) With a larger 60 nm beam, amorphization of the silicon substrate occurs.

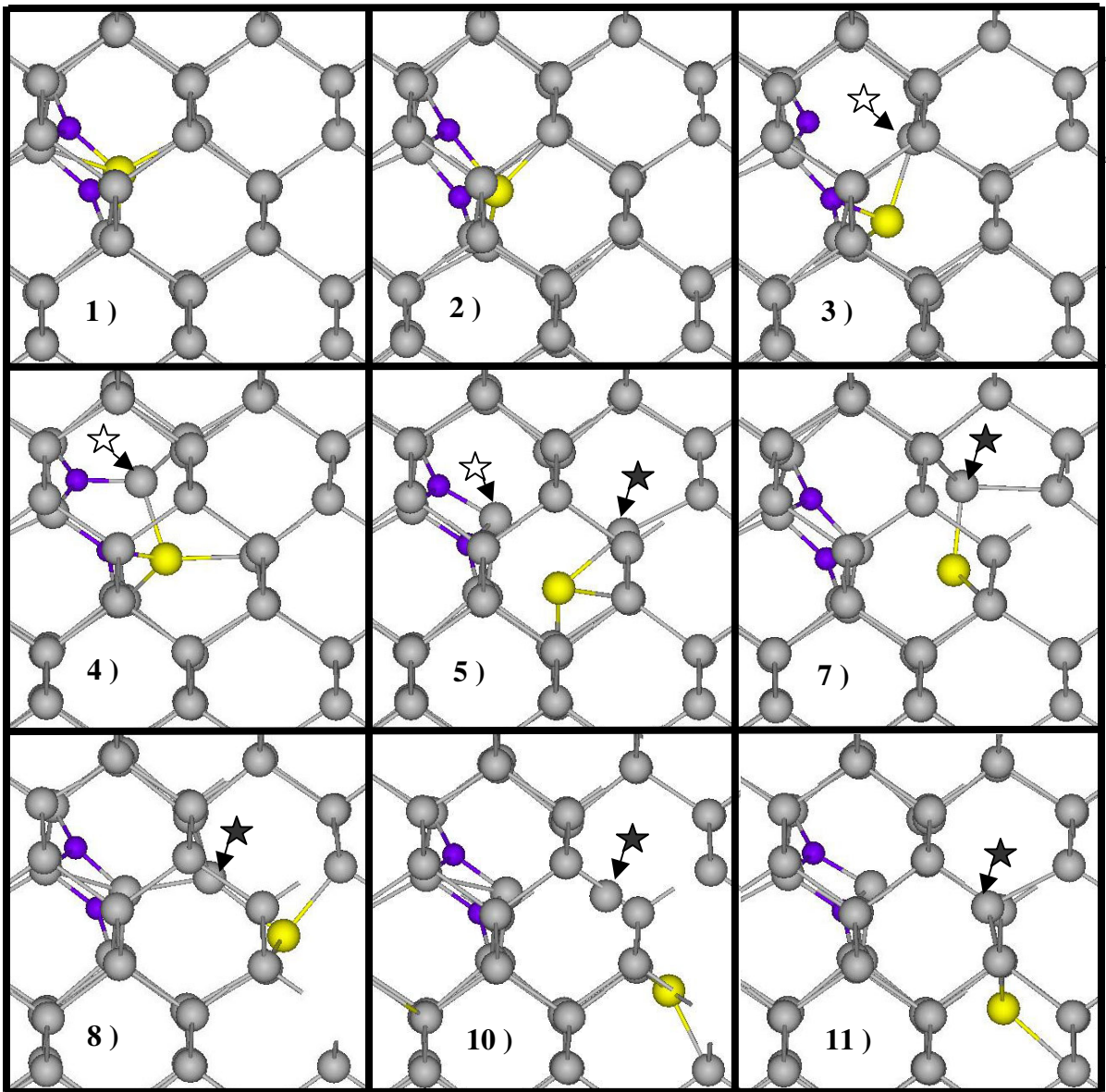


Figure 20: [110] projection of the diffusion path determined by *ab initio* nudged elastic band calculations for an excited silicon atom (in yellow) knocked away from an N<sub>2</sub> pair (in purple) and into a nearby interstitial position. The stable N<sub>2</sub> square configuration of 7-1 reforms with a new atom by 7-5, resulting in an N<sub>2</sub>V complex near a self-interstitial, 7-11.

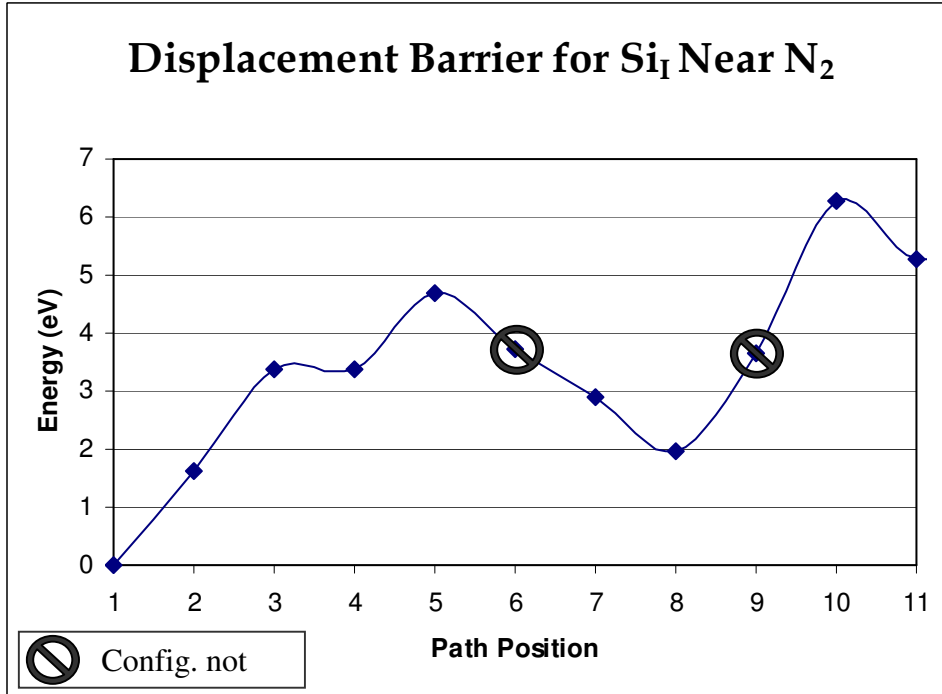


Figure 21: Energy profile of the diffusion path shown in Fig. 19. An initial 4.7 eV migration barrier leads to a local minimum at 2.0 eV above the ground state that will revert to the ground state if the excited atom does not have the 6.2 eV necessary to escape to the next nearest interstitial position. Black and white stars follow two atoms of interest.

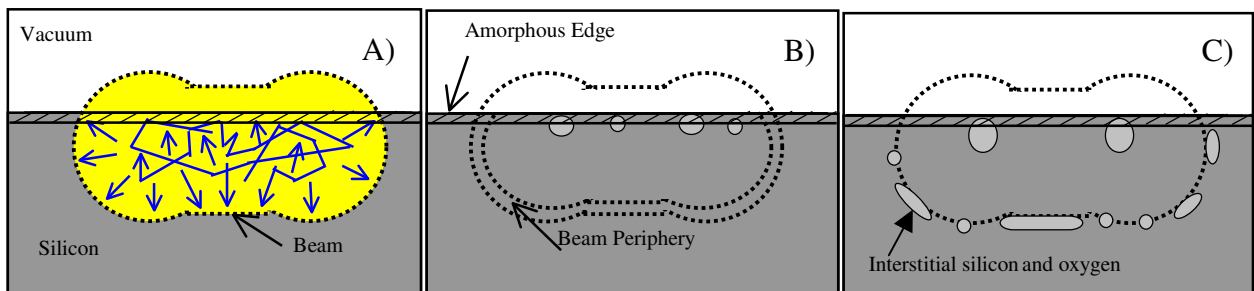


Figure 22: Illustration of a model for A) diffusion, B) nucleation and C) coarsening effects observed in Figure 16 during electron irradiation.

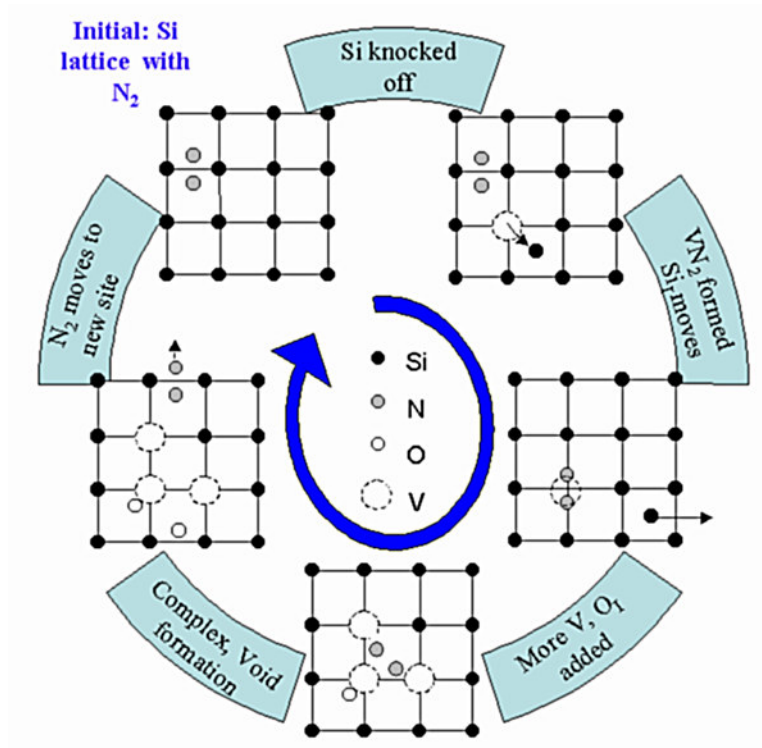


Figure 23: Model for the evolution of voids and oxygen aggregates as a result of nitrogen-assisted Frenkel pair creation during electron irradiation. The  $N_2$  pair first facilitates V-I separation, then repeats the process to form  $V_2N_2$ ,  $V_2N_2O$ ,  $V_3N_2$  and so on until the complex becomes large enough that the nitrogen diffuses away to nucleate another Frenkel pair.

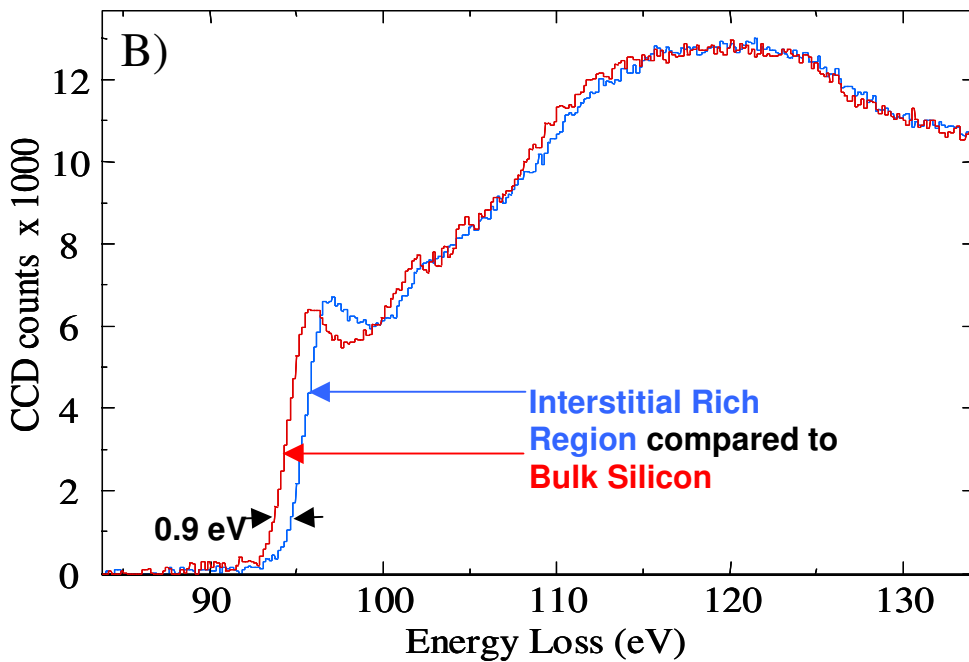
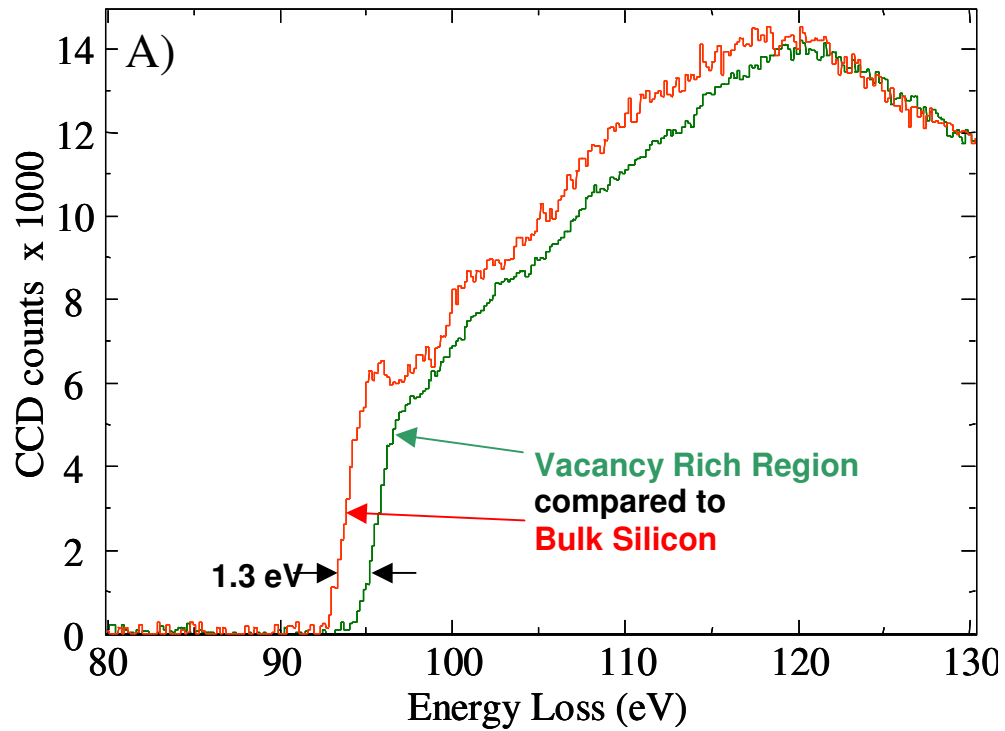


Figure 24: Electron energy-loss spectra from the JEOL TEM from the places around the irradiated area of Fig. 17B and acquired immediately after the irradiation. The spectra from both the bright (interstitial rich) and dark (vacancy rich) regions are shifted to the left relative to the bulk spectrum. Shape differences also exist indicating different changes in the local bonding environment of the silicon for the areas of interest.

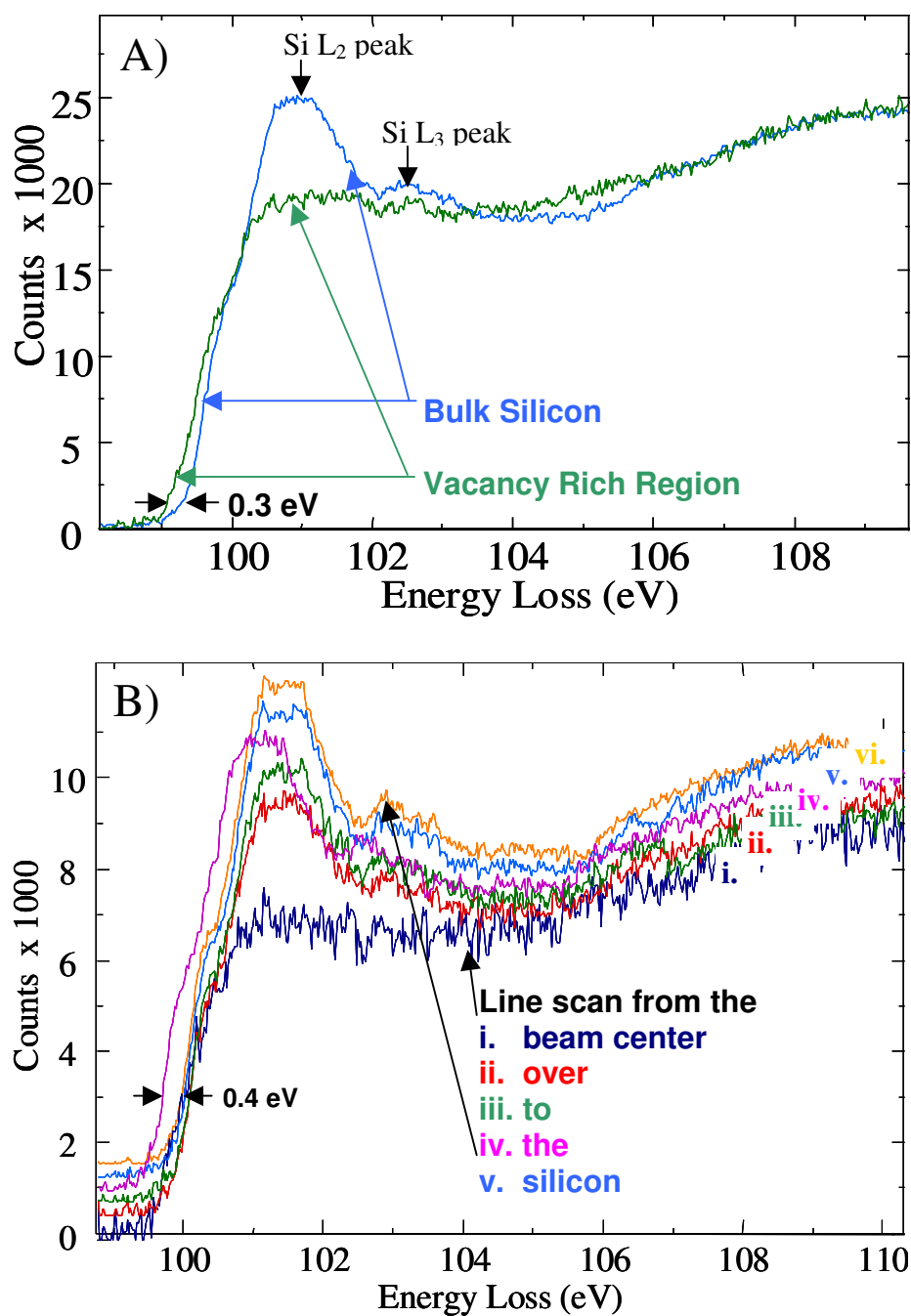


Figure 25: Energy-loss spectra from a monochromated Tecnai TEM with  $\sim 0.4$  eV effective energy resolution. A) The shape of the curve from the vacancy region matches that of Fig. 24A although the energy shift of the edge onset relative to the bulk has changed. B) A linescan moving from the center of irradiation out to the bulk. The first peak grows steadily as the bulk is approached.

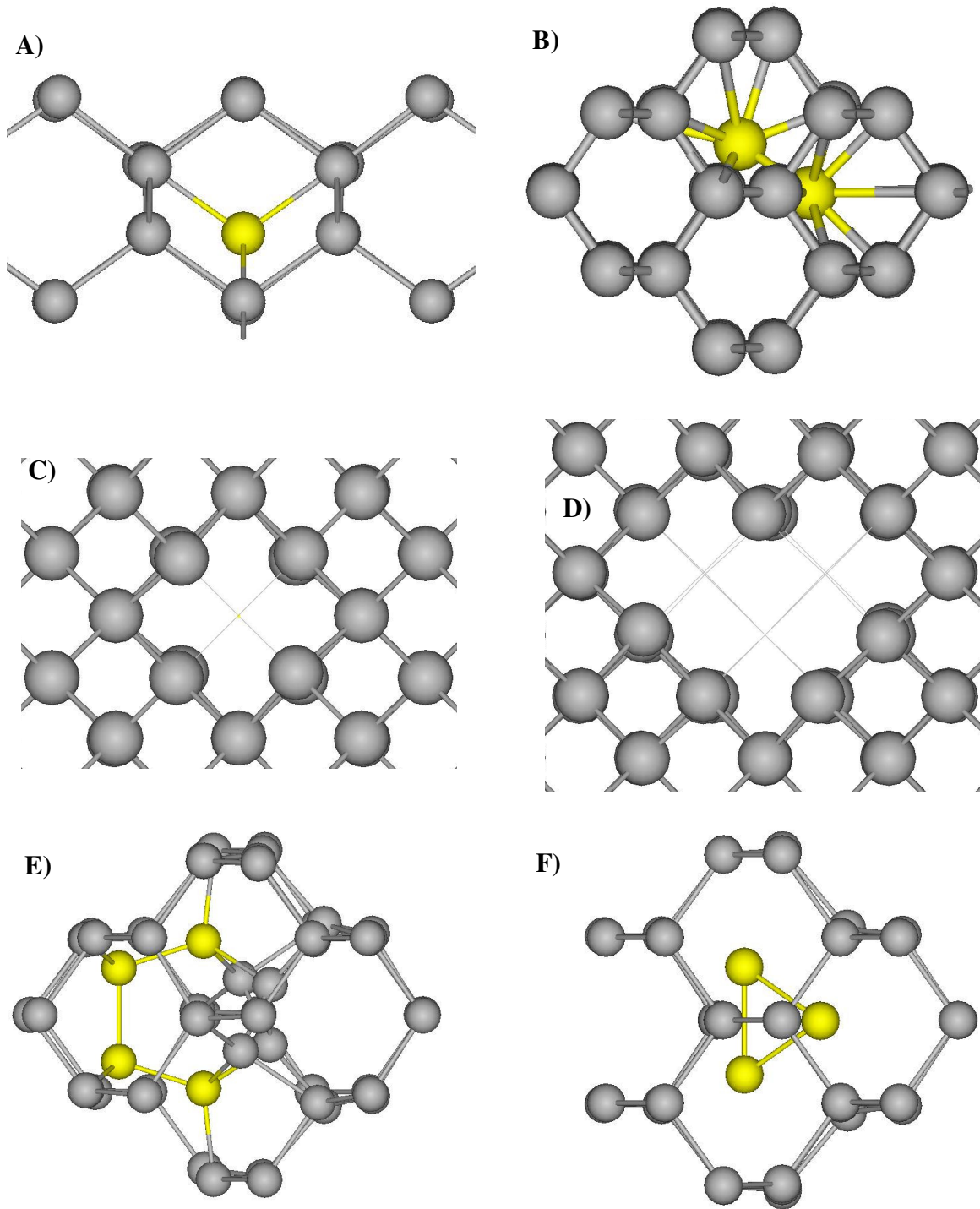


Figure 26: Relaxed configurations of various point defects and complexes. Interstitial silicon atoms are shown in yellow. A) Tetrahedral interstitial. B) Split interstitial. C) Vacancy. D) Trivacancy. E) 'Penta-ring' tri-interstitial configuration  $I_3$ -B. F) Tetrahedral tri-interstitial configuration  $I_3$ -A. A), B), E) and F) look down the  $[110]$  zone axis, C) and D) look down the  $[100]$  axis.

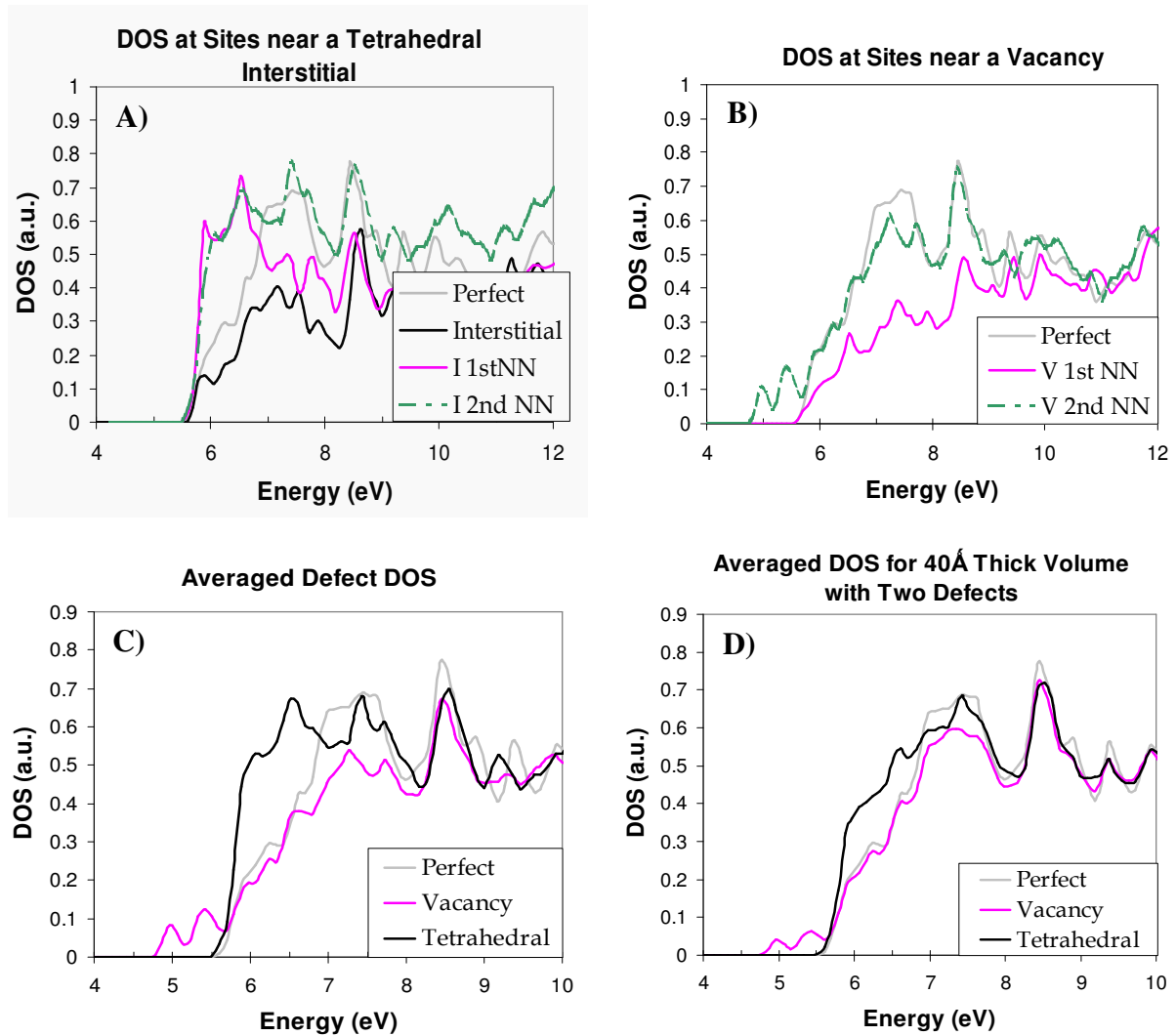


Figure 27: Simulated EELS signals from the conduction band density of states (DOS) calculated for excited atoms near point defects. The contributions from the interstitial, and from the first and second nearest neighbors to the defect in A) and B) are averaged together in C) and averaged with the equivalent of 4 nm of perfect silicon signal in D). The curves in D) indicate what might actually be measured by a spectrometer with the result of very little difference in behavior for individual point defects compared to the bulk.

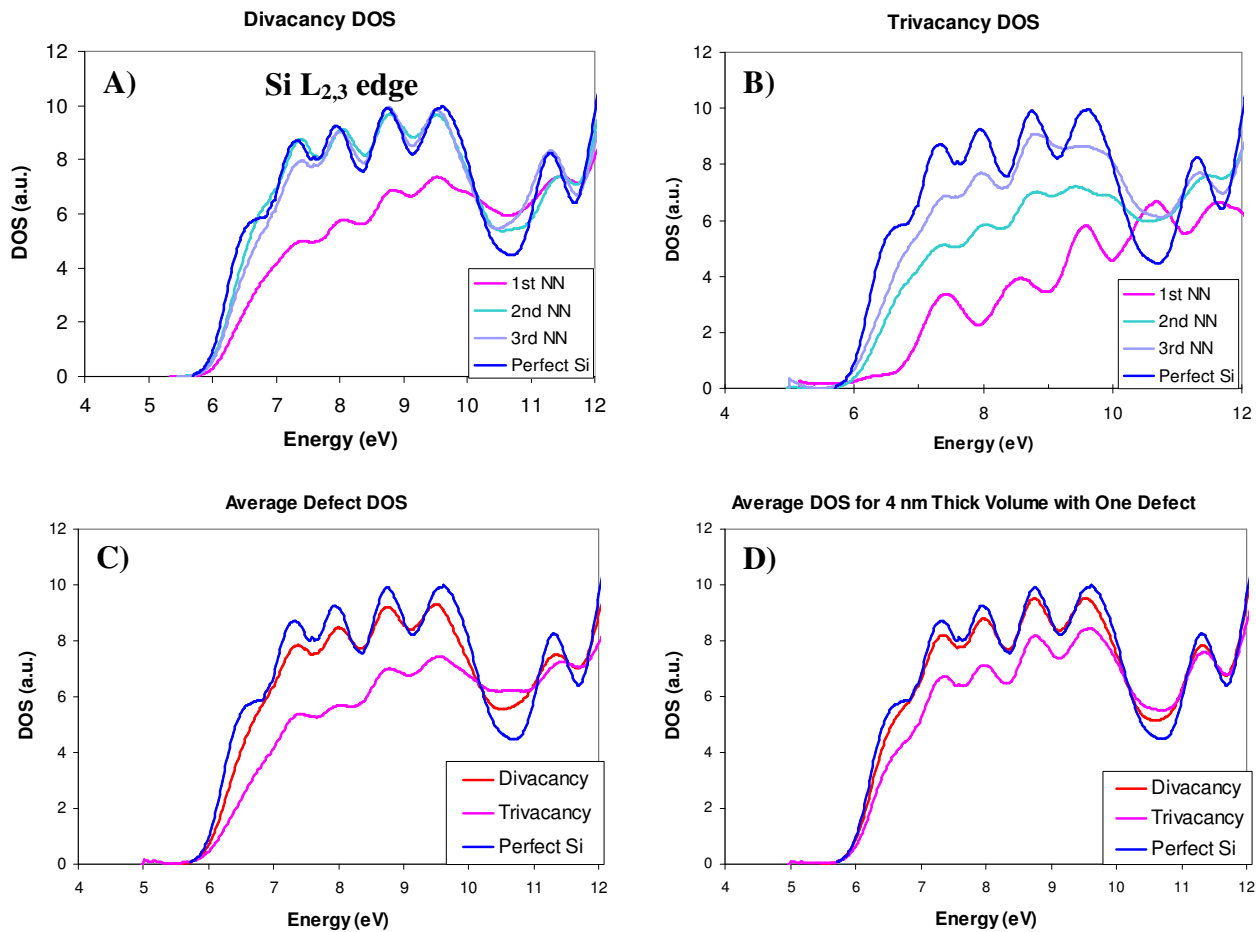


Figure 28: Simulated EELS signals from the conduction band density of states (DOS) calculated for excited atoms near two and three vacancy complexes. The raw data have been convolved to resemble electron energy loss spectra of 0.3 eV resolution. When averaged with signal from bulk silicon, the divacancy is undetectable at this energy resolution, but the trivacancy has a unique and observable change relative to the bulk.

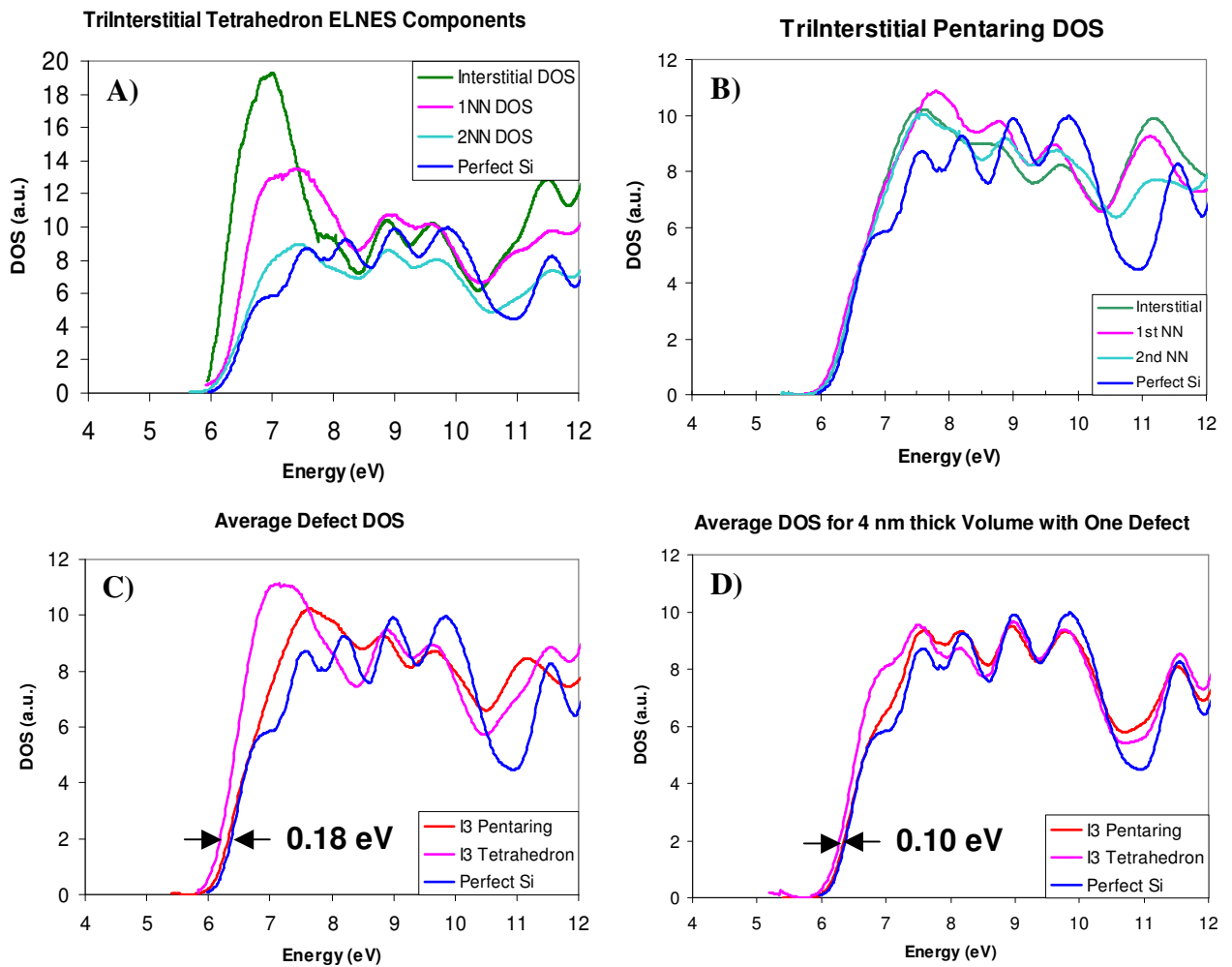


Figure 29: Simulated EELS signals from the Z+1 density of states (DOS) calculated for excited atoms near tri-interstitial complexes. The raw data have been convolved to resemble electron energy loss spectra of 0.3 eV resolution. When averaged with signal from bulk silicon, the penta-ring is distinguished by the smoothing of the first shoulder and the filling of the dip at 11eV. The tetrahedron has a unique and observable change relative to the bulk in the form of a 0.1 eV energy shift, an enhanced initial shoulder and a similar filling of the 11 eV trough.

Table 3: Atomic mass (in amu) and maximum kinetic energy transferable from a 200 keV electron for elements important to silicon processing.

Atom	Atomic Mass	$T_{max}$ (eV)
<b>Si</b>	<b>28.086</b>	<b>18.678</b>
B	10.811	48.522
C	12.011	43.676
N	14.007	37.452
O	15.999	32.787
Al	26.982	19.442
P	30.974	16.936
Ga	69.723	7.524
Ge	72.610	7.225
As	74.922	7.002
Sb	121.760	4.308
Bi	208.980	2.510

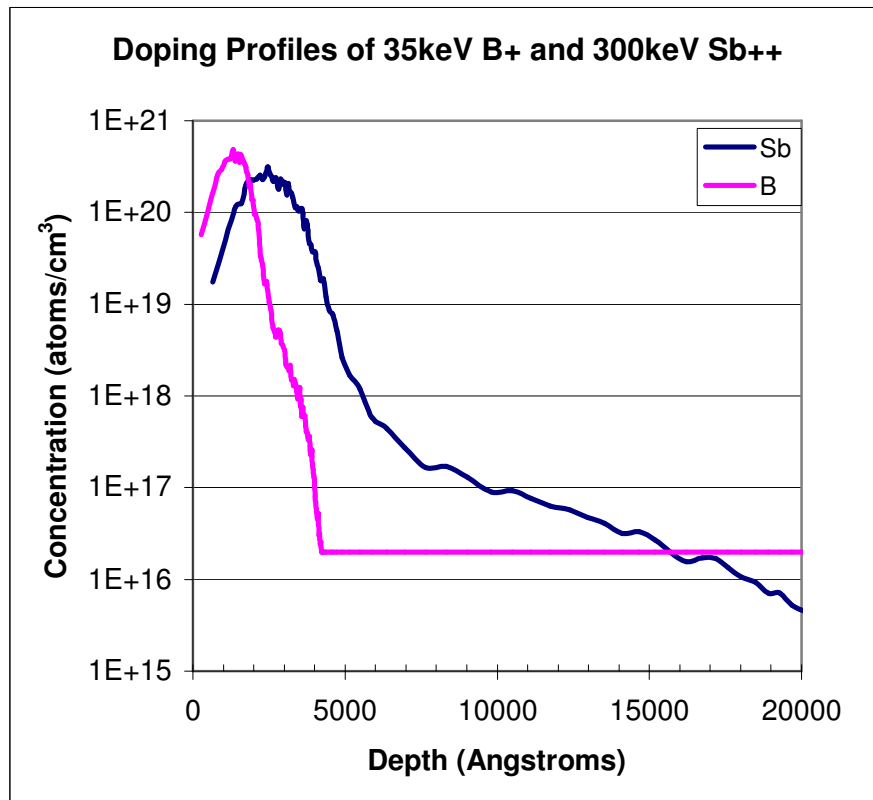


Figure 30: As implanted doping profile for a silicon sample with  $2 \times 10^{16} \text{cm}^{-3}$  bulk boron doping,  $5 \times 10^{15} \text{cm}^{-3}$  of 35 keV implanted boron, and  $5 \times 10^{15} \text{cm}^{-3}$  300 keV of implanted antimony. The curves are the result of a Monte Carlo simulation.

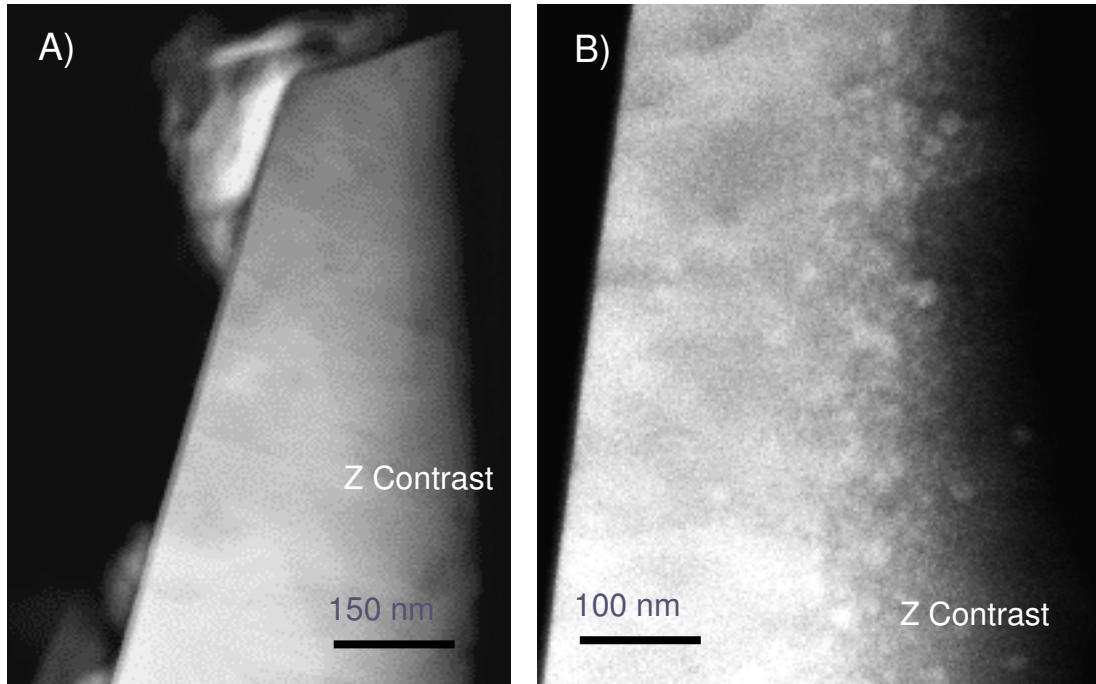


Figure: 31 Z contrast STEM images of implanted silicon samples that were recrystallized by A) Laser annealing and B) Solid Phase Epitaxy at 720°C for 30 minutes. The prior resulted in even activation but stacking fault formation while the latter resulted in dopant clustering.

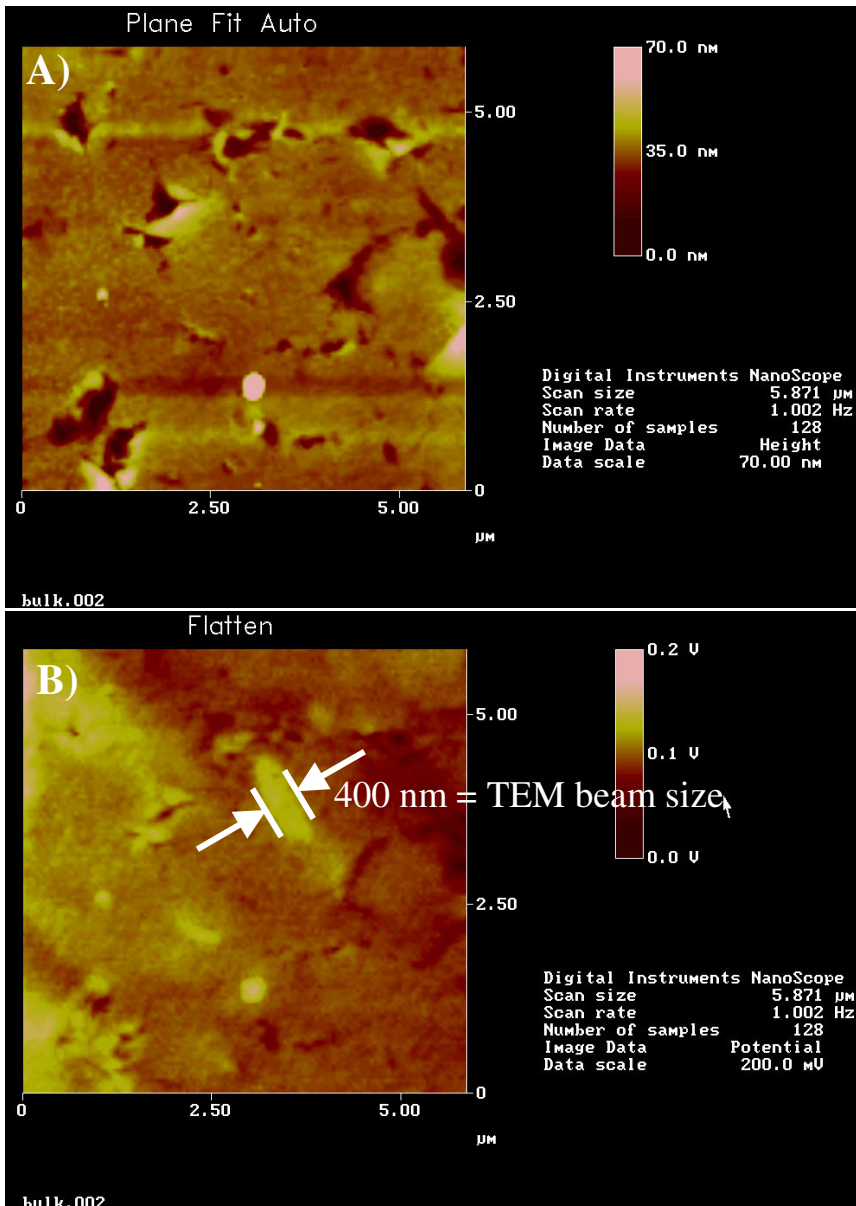


Figure 32 A) Topography and B) Surface potential images from an atomic force microscope. The surface potential feature that appears only in B) is attributed to be the result of electron irradiation of the bulk sample, due to the transition from the p-type background to the n-type irradiated spot.

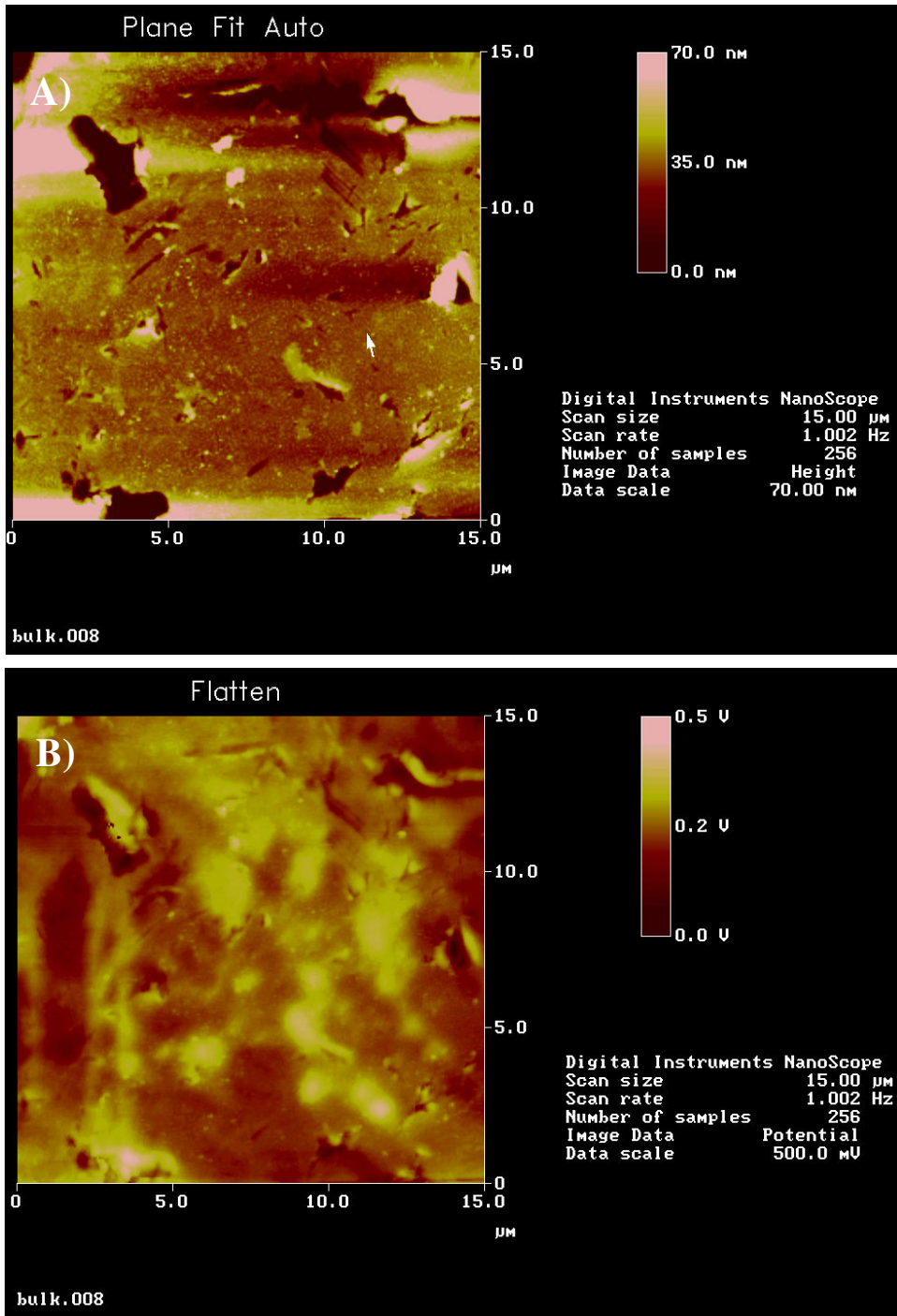


Figure 33 A) Topography and B) Surface Potential images from an AFM. The same effect is seen as in Fig. 32, but more spots are shown. On the left, a region where the beam was slowly dragged over the sample can be seen.

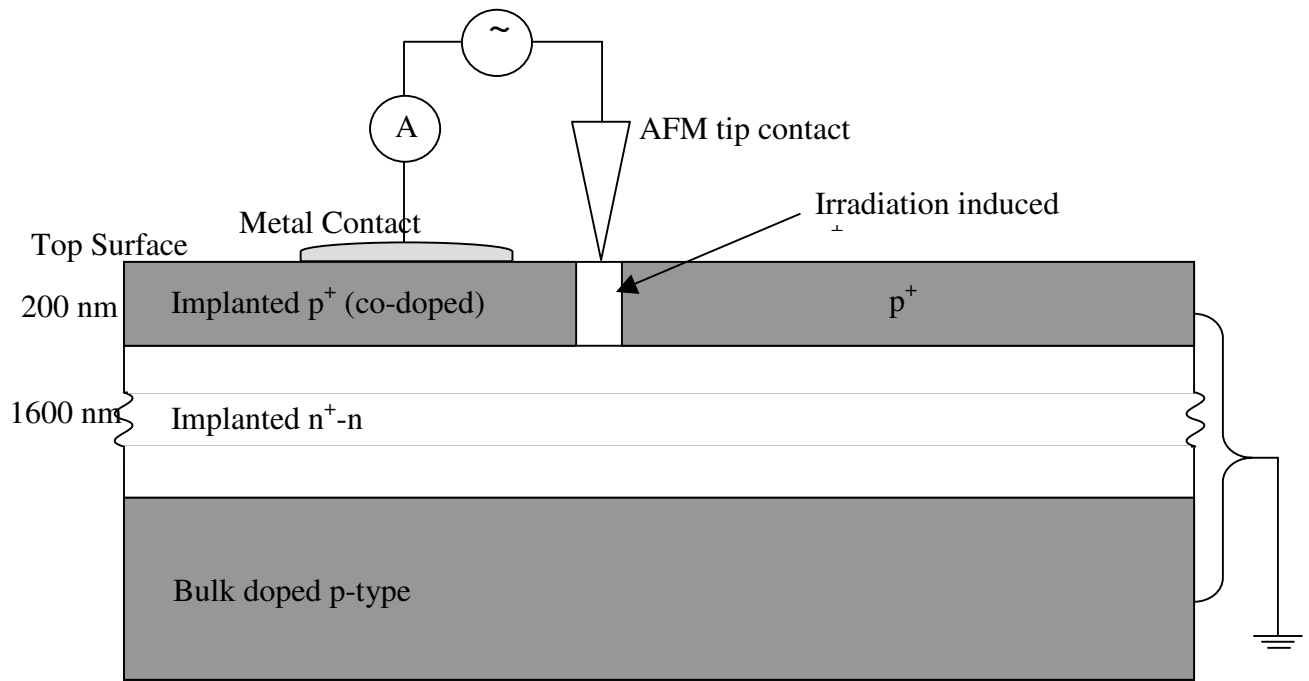


Figure 34 Device circuit for measurement of the electronic properties of the e-beam induced doped regions using a conducting AFM probe in stationary mode.

## REFERENCES

---

- <sup>1</sup> E. R. Weber, *Physica B Condensed Matter*, **340**: 1-14 (2003).
- <sup>2</sup> S. Dannefaer, P. Mascher, D. Kerr, *Phys. Rev. Lett.* **56** (20): 2195-2198 (1986).
- <sup>3</sup> O. K. Al-Mushadani, R. J. Needs, *Phys. Rev. B* **68** (23): Art. No. 235205 (2003)
- <sup>4</sup> P. M. Fahey, P. B. Griffin, J. D. Plummer, *Rev. Modern Phys.* **61** (2): 289-384 (1989)
- <sup>5</sup> G. D. Watkins, *Mat. Sci. Semicond. Proc.*, **3**, 227 (2000).
- <sup>6</sup> G.A. Rozgonyi, *Electrochem. Soc. Proc.*, 2002-1, 149 (2002).
- <sup>7</sup> M. Tamatsuka, N. Kobayashi, S. Tobe and T. Masui, *Electrochem. Soc. Proc.*, 99-1, 456 (1999).
- <sup>8</sup> K. Nakai, Y. Inoue, H. Yokota, A. Ikari, J. Takahashi, A. Tachikawa, K. Kitahara, Y. Ohta and W. Ohashi, *J. Appl. Phys.*, 89-8, 4301 (2001).
- <sup>9</sup> A. Karoui, F.S. Karoui, D. Yang, G.A. Rozgonyi, *Sol. State Phenom.*, 82-84, 69 (2002).
- <sup>10</sup> A. Karoui, F.S. Karoui, G.A. Rozgonyi, Y. Inoue, *Electrochem. Soc. Proc.*, 2002-2, 670 (2002).
- <sup>11</sup> R. Jones, S. Oberg, F. B. Rasmussen and B. B. Nielsen, *Phys. Rev. Lett.* **72** (12), 1882 (1994).
- <sup>12</sup> H. Sawada and K. Kawakami, *Phys. Rev. B* **62**, 1851 (2000).
- <sup>13</sup> T. Itoh, T. Abe. *Applied Physics Letters*, **53**, 39 (1988)
- <sup>14</sup> G. J. Willems, H. E. Maes. *Journal of Applied Physics*, **73** (7), 3256 (1993)
- <sup>15</sup> H. Kageshima, A. Taguchi, K. Wada. *Applied Physics Letters* **76** (25), 3718-3720 (2000)
- <sup>16</sup> A. Karoui, F. S. Karoui, G. Rozgonyi, M. Hourai, and K. Sueoka, *J. Electrochem. Soc.* **150**(12) G771 (2003).
- <sup>17</sup> P. A. Schultz and J. S. Nelson, *Appl. Phys. Lett.* **78**(6), 736 (2001).
- <sup>18</sup> H. Sawada, K. Kawakami, A. Ikari and W. Ohashi, *Phys. Rev. B* **65** 075201 (2002).
- <sup>19</sup> M. Kiritani, *Ultramicroscopy*, **39**(1-4): 135 (1991).

- 
- <sup>20</sup> A. Rohatgi, J. P. Schaffer, G. Augustine and M.S. Ramanachalam, *Sol. Cells*, **31**(4): 379 (1991).
- <sup>21</sup> J. C. Bourgoin, N. de Angelis, *Sol. Energ. Mat. Sol. C*, **66**(1-4): 467 (2001).
- <sup>22</sup> M. Kiritani, *J. Nucl. Mater.*, **251**, 237 (1997).
- <sup>23</sup> R. Oshima and G. C. Hua, *Ultramicroscopy*, **139**, 160 (1991).
- <sup>24</sup> L. Fedina, A. Gutakovski, A. Aseev, J. Van Landuyt, J. Vanhellefont, *Phys. Stat. Sol. A*, **171**(1): 147-157 (1999).
- <sup>25</sup> S. Arai, Y. Satoh, K. Arakawa, C. Morita and M. Kiritani, *J. Electron Microsc.*, **53**(1): 21 (2004).
- <sup>26</sup> W. Windl, T. J. Lenosky, J. D. Kress, A. F. Voter, *Nucl. Inst. Meth. Phys. B*, **141** (1-4): 61-65 (1998)
- <sup>27</sup> T. Diaz de la Rubia and V. V. Bulatov, *MRS Bulletin*, **26**(3): 169 (2001).
- <sup>28</sup> M. J. Caturla, T. Diaz de la Rubia and M. Fluss, *J. Nucl. Mater.* **323** (2-3): 163-168 (2003).
- <sup>29</sup> K. Morishita, R. Sugano, B. D. Wirth, *Fusion Sci. Tech.*, **44** (2): 441-445 (2003).
- <sup>30</sup> R. S. Averback and T Diaz de la Rubia, *Sol. State Phys.* **51**, 281 (1997).
- <sup>31</sup> J. Yamasaki, S. Takeda, and K. Tsuda, *Physical Review B*, **65**, 115213 (2002).
- <sup>32</sup> D. N. Seidman, R. S. Averback, P. R. Okamoto, and A. C. Baily, *Phys. Rev. Lett.* **58**, 900 (1987).
- <sup>33</sup> L. Reimer, *Transmission Electron Microscopy: The Physics of Image Formation and Microanalysis*, Springer-Verlag, Berlin (1993).
- <sup>34</sup> R. F. Egerton, *Electron Energy-Loss Spectroscopy in the Electron Microscope*, 2<sup>nd</sup> ed. (Plenum Press, New York, 1996), pp. 137, 186.
- <sup>35</sup> R. Falster, *Electrochem. Soc. Proc.*, 98-13, 135 (1998).
- <sup>36</sup> S. J. Pennycook and L. A. Boatner, *Nature*, **366**, 565 (1988).
- <sup>37</sup> A. Karoui, F.S. Karoui, A. Kvit, G. A. Rozgonyi and D. Yang, *Appl. Phys. Lett.*, **80**-12, 2114 (2002).

- 
- <sup>38</sup> W. Windl, in *Si Front-End Processing-Physics and Technology of Dopant-Defect Interactions III*, edited by K. S. Jones et al., MRS Symposia Proceedings **669** (Materials Research Society, Pittsburgh, 1998), p. J4.11
- <sup>39</sup> H. P. Hjalmarson, P. Vogl, D. J. Wolford, and J. D. Dow, *Phys. Rev. Lett.* **44** (12): 810-813 (1980)
- <sup>40</sup> D. Bollinger, R. Fink, *Solid State Technology*, **23** (11), 79 (1980).
- <sup>41</sup> S. E. Jacobson, N. A. Cade, R. A. Lee, *Instrumentation in Physics Conference Series*. (99): 5-8 (1989).
- <sup>42</sup> D. J. Barber, *Ultramicroscopy*. **52**(1) 101 (1993).
- <sup>43</sup> Michael Nastasi, James Mayer and James Hirvonen, *Ion-Solid Interactions: Fundamentals and Applications*. Cambridge; New York: Cambridge University Press, 1996.
- <sup>44</sup> A. Pivovarov, F. A. Stevie, D. P. Griffis, G. M. Guryanov, *Journal of Vacuum Science Technology A*, **21** (5): 1649-1654 (2003)
- <sup>45</sup> A. Karoui et al., *J. of Appl. Phys.* **96**(4) 15 (Part-I and Part-II, 2004).
- <sup>46</sup> V. S. Vavilov, A. E. Kiv and O. R. Niyazova. *Phys. Status Solidi (a)***32** (1975), p. 11.
- <sup>47</sup> H. J. Himpfel, F. R. McFeel, A. Taleb-Ibrahimi, J. A. Yarmoff, G. Hollinger, *Phys. Rev. B*, **38**, 6084 (1988).
- <sup>48</sup> G. Duscher, R. Buczko, S. J. Pennycook and S. T. Pantelides, *Ultramicroscopy* **86**, 355 (2001).
- <sup>49</sup> T. Hojo, M. Sato, H. Komano, *J. Photopolymer Sci. and Tech.*, **16** (3): 455-458 (2003).
- <sup>50</sup> A. M. Haghiri-Gosnet, C. Vieu, G. Simon, M. Mejias, F. Carcenac, H. Launois, *J. De Physique IV*, **9** (P2): 133-141 (1999).
- <sup>51</sup> W. Windl, M. M. Bunea, R. Stumpf, S. T. Dunham, M. P. Masquelier, *Phys. Rev. Lett.*, **83**(21), 4345 (1999).
- <sup>52</sup> D. K. An, *Defect Diffus. Forum*, **194**(1): 653-658 (2001).
- <sup>53</sup> E. Napolitani, D. DeSalvador, A. Carnera, S. Mirabella, F. Priolo, To be published in the Proceedings of MRS 2004 Spring meeting, symposium C.
- <sup>54</sup> S. H. Yoo, J. S. Ro, *J. Korean Phys. Soc*, **43**(2), 290 (2003).